INFLUENCE OF WATER AND MEMBRANE MICROSTRUCTURE ON THE TRANSPORT PROPERTIES OF PROTON EXCHANGE MEMBRANE FUEL CELLS

by

Ana Rosa Siu
B. Sc. (Hons), Simon Fraser University, 2000

THESIS SUBMITTED IN PARTIAL FULFILLMENT OF
THE REQUIREMENTS FOR THE DEGREE OF

DOCTOR OF PHILOSOPHY

In the
Department
of Chemistry

SIMON FRASER UNIVERSITY

Spring 2007

APPROVAL

Name: Ana Siu

Degree: Doctor of Philosophy

Title of Thesis: Influence of Water and Membrane Microstructure on the Transport Properties of Proton Exchange Membrane Fuel Cells

Examining Committee:

Dr. Ross H. Hill
Chair
Professor

Dr. Steven Holdcroft
Senior Supervisor
Professor, Department of Chemistry

Dr. George R. Agnes
Supervisor
Professor, Department of Chemistry

Dr. Vance E. Williams
Supervisor
Assistant Professor, Department of Chemistry

Dr. Michael H. Eikerling
Internal Examiner
Assistant Professor, Department of Chemistry

Dr. Peter N. Pintauro
External Examiner
Professor, Chemical Engineering Department
Case Western Reserve University

Date Approved: December 18, 2006

ABSTRACT

Proton transport in proton exchange membranes (PEMs) depends on interaction between water and acid groups covalently bound to the polymer. Although the presence of water is important in maintaining the PEM's functions, a thorough understanding of this topic is still lacking. The objective of this work is to provide a better understanding of how the nature water, confined to ionic domains of the polymer, influences the membrane's ability to transport protons, methanol and water. Understanding this topic will facilitate development of new materials with favorable transport properties for fuel cells use.

Five classes of polymer membranes were used in this work: polyacrylonitrile-graft-poly(styrenesulfonic) acid (PAN-g-macPSSA); poly(vinylidene difluoride) irradiation-graft-poly(styrenesulfonic) acid (PVDF-g-PSSA); poly(ethylenetetrafluoroethylene) irradiation-graft- poly(styrenesulfonic) acid (ETFE-g-PSSA); PVDF-g-PSSA with hydroxyethylmethacrylate (HEMA); and perfluorosulfonic acid membrane (Nafion).

The nature of water within the polymers (freezable versus non-freezable states) was measured by systematically freezing samples, and observing the temperature at which water freezes and the amount of heat released in the process. Freezing water-swollen membranes resulted in a 4-fold decrease in the proton conductivity of the PEM. Activation energies of proton transport before and after freezing were ~ 0.15 eV and 0.5 eV, consistent with proton transport through liquid water and bound water, respectively. Reducing the content of water in membrane samples decreased the amount of freezable

and non-freezable water. Calorimetric measurements of membranes in various degrees of hydration showed that water molecules became non-freezable when λ (water molecules per sulfonic acid group) was less than ~14. Proton conduction through membranes containing only non-freezable water was demonstrated to be feasible.

Diffusion experiments showed that the permeability of methanol decreased when the content of free water in the membranes decreased. Variation in permeability trends observed for the different polymer classes of the same content of free water was explained on the basis of tortuosity and interaction of methanol within the ionic network. Finally, a novel set of polymers containing non-ionic hydrophilic segments were examined for enhanced water transport in order to see if such domains might offset the flux of water due to electro-osmosis.

To my parents and family,

who encouraged and supported me throughout my studies

ACKNOWLEDGEMENTS

I would like to thank:

My senior supervisor Prof. Steven Holdcroft, who gave me his supervision, endless patience, scientific freedom, many research assistantships, and opportunities to work in his laboratory and to travel abroad during my studies.

My supervisory committee Prof. George Agnes and Prof. Vance Williams for their great ideas to improve my thesis.

My examining committee, Prof. Peter N. Pintauro, and Prof. Michael Eikerling for taking the time to read my thesis.

Dr. Bryan Pivovar, who gave the opportunity to work on my thesis at Los Alamos National Laboratory, for his mentorship, as well as time to proof-read this thesis

Dr. George Vamvounis for his inspiration and encouragement, and for proof-reading this thesis.

Dr. Jianfu Ding and Mr. Keith V. Lovell for providing the samples for my thesis.

National Research Council Canada, Institute for Fuel Cell Innovation (NRC-IFCI) for allowing the use of DSC equipment, and Dr. Z. Shi for coordinating the use of the DSC equipment and for providing the TEM image of Nafion®.

Dr. H. Every of LANL for assistance in PFG-NMR experiments on PAN-*g*-*mac*PSSA membranes, and Dr. A. Herring and Mr. S. Dec. for performing PFG-NMR experiments of PVDF-*g*-PSSA membranes at Colorado School of Mines.

Drs. R. Michalczyk, B. MacDonald, A. Tracey, A. Lewis, Z. Xie, M. Eikerling and B. Andreaus for their helpful and valuable comments.

Ms. Jennifer Schmeisser and Ms. Amy Yang for assistance in acquiring some of the proton conductivity data presented in Chapter 2. Dr. Titichai Navessin for providing the fuel cell data presented in Chapter 4. Dr. Laurent Rubatat and Mr. Makoto Adachi for providing the hydraulic permeability data presented in Chapter 4. Prof. Barbara Frisken for allowing us to use her hydraulic permeability set-up.

Staff in the machine shop and the electronic shop for their valuable technical support.

My proof readers: Dr. Tim Peckham, Ms. Emily Larkman, Mr. Nestor Siu, Mr. Julian Ehlers, and Dr. Ricky Lee for their timely and constructive criticisms.

Past and current group membranes for their friendship and useful discussions.

Simon Fraser University, Methanex Corp., Los Alamos National Laboratory, and the Natural Sciences and Engineering Research Council of Canada for financial support.

TABLE OF CONTENTS

LIST OF FIGURES

LIST OF TABLES

LIST OF ABBREVIATIONS

AFC	alkaline fuel cell
ATR-FTIR	attenuated total reflectance – fourier transform infrared
"BRICS"	Brazil, Russia, India and China
DMFC	direct methanol fuel cell
DMSO	dimethylsulfoxide
DSC	differential scanning calorimetry
ETFE	poly(ethylenetetrafluoroethylene)
ETFE-*g*-PSSA	poly(ethylenetetrafluoroethylene) irradiation-*graft*-poly(styrenesulfonic) acid
EU	European Union
GDE	gas diffusion electrode
GDP	gross domestic products
HEMA	hydroxyethylmethacrylate
IEA	International Energy Annual
IEC	ion exchange capacity
FTIR	fourier transform infrared
MCFC	molten carbonate fuel cell
MEA	membrane electrode assembly
N117	Nafion®
NMR	nuclear magnetic resonance
PAFC	phosphoric acid fuel cell
PAN	polyacrylonitrile
PAN-*g*-*mac*PSSA	polyacrylonitrile-*graft*-poly(styrenesulfonic) acid
PEM	proton exchange membrane
PEMFC	proton exchange membrane fuel cell
PFG-NMR	pulsed field gradient nuclear magnetic resonance
PSSANa	poly(styrenesulfonic), sodium
PTFE	poly(tetrafluoroethylene)
PVDF	poly(vinylidene difluoride)

PVDF-*g*-(HEMA-*co*-SSA)	simultaneous co-polymerization of HEMA and styrene as grafts to PVDF
PVDF-*g*-PSSA	poly(vinylidene difluoride) irradiation-*graft*-poly(styrenesulfonic) acid
PVDF-*g*-PSSA-*g*-HEMA	PVDF-*g*-PSSA *graft* HEMA
RH	relative humidity
S	saturation vapour pressure
SOFC	solid oxid fuel cell
SSNa	styrenesulfonic, sodium
TGA	thermal gravimetric analysis
TEM	transmission electron microscope
TEMPO	2,2,6,6-tetramethyl-1-piperidinyloxy
US	United States
VWT	water vapour transmission

LIST OF SYMBOLS

α	transfer coefficient
A	area of membrane
A(0)	PFG-NMR signal when no gradient is applied
A(g)	PFG-NMR signal when gradient is applied
c_s^o	concentration of methanol in the source compartment
c_r^o	concentration of methanol in the receiving compartment
D_{H2O}	self-diffusion coefficient of water
Δ	time between gradient pulses
δ	length of gradient pulse
D_{app}	apparent diffusion coefficient
D_σ	diffusion coefficient of protons (Einstein Relation)
D_{MeOH}	diffusion coefficient of methanol
D_{O2}	diffusion of oxygen
E	potential when current is flowing
E^{eq}	equilibrium potential
η	overpotential
g	gradient strength
γ	gyromagnetic ratio
G	weight change
H	partition coefficient
$[H^+]_{est}$	estimated acid concentration in the membrane
j	kinetic-controlled current density
j^o	exchange current density
K_H	permeance of water measured by applying a pressure difference across the sample
Kv	permeance of water measured by applying a vapour gradient across the sample
l	thickness of membrane
λ	H_2O/SO_3^-

$\lambda_{freezable}$	freezable water expressed as H_2O/SO_3^-
$\lambda_{non\text{-}freezable}$	non-freezable water expressed as H_2O/SO_3^-
λ_{total}	total water expressed as H_2O/SO_3^-
μ_{est}	estimated proton mobility in the membrane
n_{drag}	electro-osmotic drag coefficient
Δp	pressure difference
P	pressure
P_{MeOH}	methanol permeability
$P_{H2O,hydraulic}$	hydraulic permeability
$P_{H2O,WVT}$	water vapour transmission permeability
Q	volume flow rate
R_m	membrane resistance
Ru	uncompensated resistance
R_1	relative humidity in vial
R_2	relative humidity outside of vial
σ	proton conductivity
σ / P_{MeOH}	ratio of proton conductivity to methanol permeability
t	time
T	temperature
V_s	volume of methanol in the source compartment
V_r	volume of methanol in the receiving compartment
W_f	fraction of freezable water
W_t	total water
W_{nf}	fraction of non-freezable water
$\langle x^2 \rangle$	root mean square displacement
X_v	fraction of water in the membrane
$X_v F_{freezable}$	fraction of freezable in the membrane
$\lvert z \rvert$	valence of ion

CHAPTER 1:

INTRODUCTION TO FUEL CELLS

1.1 Motivation for the development of fuel cells

The economy in most countries is reliant on a constant supply of low cost energy primarily from non-renewable fossil fuel sources. Statistics from the International Energy Annual (IEA) in 2004 indicate that a significant portion of this energy (~ 38 %) is derived from petroleum,[1] that, according to projections is only expected to remain sustainable for another 40 years.[2] With the rapid increase in gross domestic product (GDP) predicted for the European Union (EU), the United States (US) and the four major developing "BRICS" countries (Brazil, Russia, India and China), energy demands are expected to deplete the oil reserves much sooner than the 40 year timeline.[2,3]

Recent statistics indicate that the discovery of oil reserves appears to have slowed down considerably in the last decade, with discoveries between 1990 and 2000 at ~ 25 % of those between 1950 and 1960.[2] According to an analysis published in The Economist in 8/12/2001, oil production probably reached its maximum capacity in 2003.[2,4] The gap between supply and demand is projected to widen to 65 million barrels/day in 2020 with continued consumption and population growth. Increasing oil recovery from existing wells is not expected to improve the situation significantly. The IEA estimates that developing new fields (e.g., deep sea drilling down to 2000 m in 2010) will require an enormous investment of ~ $ 1 trillion US. Even then, concerns remain whether investments made to develop new and more expensive oil wells will come in time to curb shortages of oil supply and unfriendly competition.[2]

In order to promote energy self-reliance, supply security, sustainability and clean air, many analysts agree that the long-term solution is to use renewable energy harvested from diverse sources. One energy carrier that can satisfy this goal is hydrogen. Hydrogen can come from diverse sources (e.g., fossil fuels, and water), and is abundant in many organic compounds. Once separated from other elements, hydrogen can be directly burned, or converted into electricity through fuel cells. Fuel cells are thus, expected to play a significant role in achieving a hydrogen economy.[5]

1.2 Types of Fuel Cells

A fuel cell is a galvanic electrochemical energy conversion device similar to a battery, but designed so that reactants are continuously supplied to the electrodes. The choice of electrolyte materials governs many things: (1) the chemical reactions that take place at the electrode/electrolyte interface, (2) the type of catalysts that should be used, (3) the temperature range in which the fuel cell can operate, (4) and the fuel that can be supplied. These characteristics in turn influence the suitability of the fuel cell application. Table 1.1 lists examples of common fuel cells.[6-8]

Table 1.1: Overview of common fuel cells.

Fuel Cell	Electrolyte	Operating Temperature (°C)	Efficiency (%)	Electrochemical Reactions
Molten Carbonate Fuel Cell (MCFC)	Solutions of lithium, sodium, and/or potassium carbonates soaked in a matrix	600 – 1000	45-60	**Anode:** $H_2 + CO_3^{2-} \rightarrow H_2O + CO_2 + 2e^-$ **Cathode:** $\frac{1}{2} O_2 + CO_2 + 2e^- \rightarrow CO_3^{2-}$ **Cell:** $H_2 + \frac{1}{2} O_2 + CO_2 \rightarrow H_2O + CO_2$ CO_2 is consumed at the anode and produced at the cathode so it is included on both sides of the equation)
Phosphoric Acid Fuel Cell (PAFC)	Phosphoric acid soaked in a matrix	175 – 200	35 – 50	**Anode:** $H_2 \rightarrow 2H^+ + 2e^-$ **Cathode:** $\frac{1}{2} O_2 + 2H^+ + 2e^- \rightarrow H_2O$ **Cell:** $H_2 + \frac{1}{2} O_2 \rightarrow H_2O$
Proton Exchange Membrane Fuel Cell (PEMFC)	Ion exchange membrane	30 - 80	35 – 50	**Anode:** $H_2 \rightarrow 2H^+ + 2e^-$ **Cathode:** $\frac{1}{2} O_2 + 2H^+ + 2e^- \rightarrow H_2O$ **Cell:** $H_2 + \frac{1}{2} O_2 \rightarrow H_2O$
Solid Oxide Fuel Cell (SOFC)	Solid zirconium oxide with a small amount of yttria	600 - 1000	45 – 60	**Anode:** $H_2 + O^{2-} \rightarrow H_2O + 2e^-$ **Cathode:** $\frac{1}{2} O_2 + 2e^- \rightarrow O^{2-}$ **Cell:** $H_2 + \frac{1}{2} O_2 \rightarrow H_2O$
Alkaline Fuel Cell	Aqueous solution of potassium hydroxide soaked in a matrix	90 - 100	< 60	**Anode:** $H_2 + 2\ OH^- \rightarrow 2H_2O + 2e^-$ **Cathode:** $\frac{1}{2} O_2 + H_2O\ 2e^- \rightarrow 2(OH^-)$ **Cell:** $H_2 + \frac{1}{2} O_2 \rightarrow H_2O$

The focus of this thesis is on proton exchange membrane fuel cells (PEMFC). Their promise as a low polluting and highly efficient energy conversion system with high power densities, quiet operation, moderate temperature range (30 – 200 °C), and adaptability to many hydrogen-containing fuels make them attractive for a variety of applications, such as large-scale power generation, automobiles and small portable electronic devices (e.g., laptops).

1.3 The Proton Exchange Membrane Fuel Cell

1.3.1 Evolution of PEMFC Technology

The fuel cell was first demonstrated in 1839 by Sir William Grove. The technology, however, gained little popularity due to a lack of specialized applications for them. Although some excitement was created in 1959 with the 29 kW fuel cell-powered tractor, the first significant breakthrough, however, came after 1965 when fuel cells found their first major application in the NASA's Gemini space mission. The unit, developed by General Electric Research Laboratory, was a PEMFC that employed sulfonated polystyrene membranes and platinum black electrodes.[6] Individual cells were stacked together to form 1 kW units in order to provide electricity for the spacecraft. Although PEMFCs were efficient at delivering high power densities, their high cost and the short lifetimes of the polystyrene-based membranes prevented their commercialization. Development of PEMFC technology has generated renewed interest within the last three decades following the discovery of more stable and ionically conductive perfluorosulfonic acid solid polymer electrolytes, such as Nafion® (Figure 1.1), as well as the efforts undertaken by the government (e.g., The California Clean Air Act), private investors (e.g., Ballard Power Systems), and major automobile

manufacturers that expanded fuel cells for terrestrial use.[6,9] The need to develop more environmental friendly solutions to meet and supplement growing world energy demands and energy costs are the main driving forces for the development of this technology. Consequently, this has also led to the development of fuel cells for electronic devices.[2]

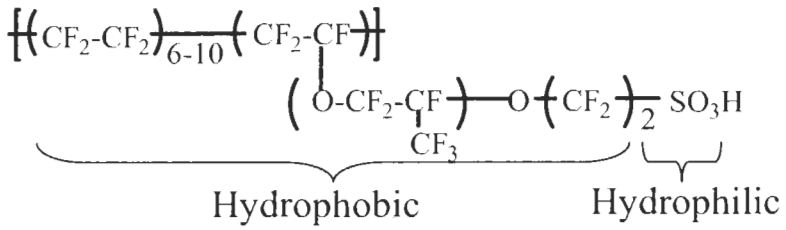

Figure 1.1: Chemical structure of Nafion®.

1.3.2 Essential Features of PEMFCs

The main components of a single PEMFC are illustrated in Figure 1.2. It consists of an anode, a cathode and an electrolyte. Porous carbon fibre paper/cloths dispersed with platinum particles form the anode and cathode. A polymer-based proton exchange membrane (PEM) is sandwiched between the electrodes to form the membrane electrode assembly (MEA). The MEA is compressed between two light and electronically conductive plates (e.g., graphite) that serve as current collectors. Flow fields are machined into the plates over the active region of the electrode in order to deliver reactants to the electrodes. The compressed MEAs-plate units are stacked in series so that individual cell voltages can be added together.

The electrochemical reactions that take place for a hydrogen/oxygen fuel cell are illustrated below. Hydrogen gas is oxidized at the anode (equation 1.1) under the application of a load to form protons and electrons. Protons migrate through the membrane to the cathode, whereas electrons are transported *via* an external circuit to the

cathode. At the cathode, oxygen reacts with electrons and protons to form water (equation 1.2). The external current flow is the source of electricity from the fuel cell.

$$\text{Anode:} \quad H_2(g) \rightarrow 2H^+(aq) + 2e^- \qquad E^o = 0.00\ V \qquad (1.1)$$

$$\text{Cathode:} \quad \tfrac{1}{2}\, O_2(g) + 2H^+ + 2e^- \rightarrow H_2O(l) \qquad E^o = 1.23\ V \qquad (1.2)$$

$$\text{Net Reaction:} \quad H_2(g) + \tfrac{1}{2}\, O_2(g) \rightarrow H_2O(l) \qquad E^o = 1.23\ V \qquad (1.3)$$

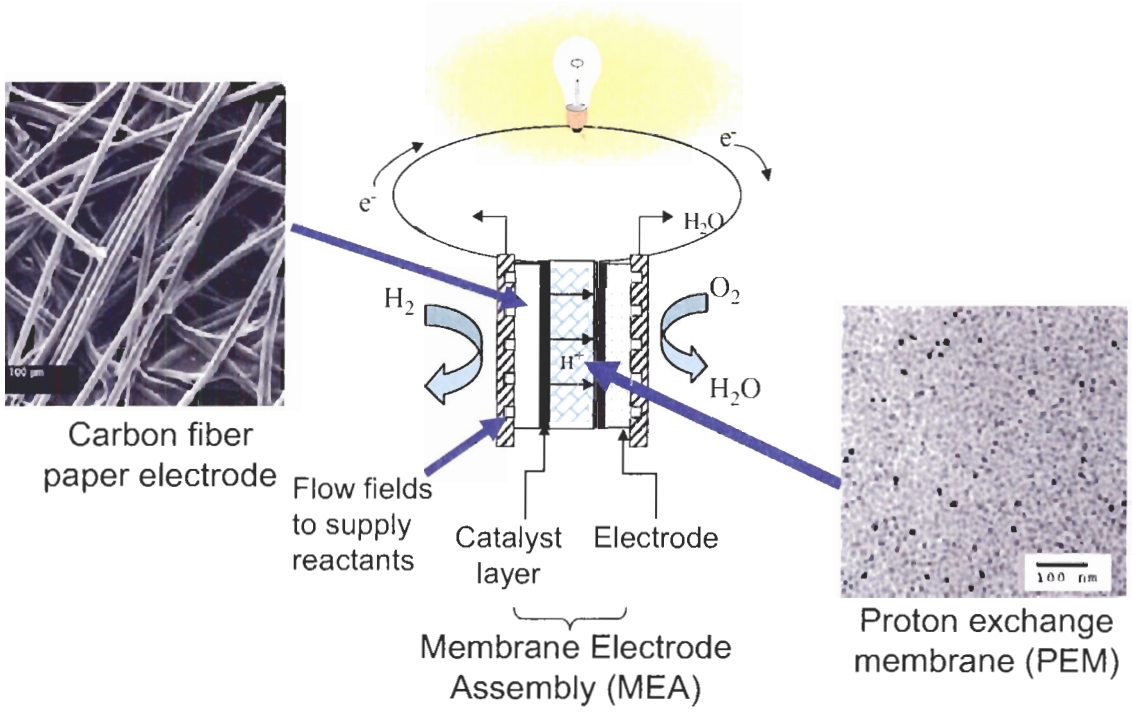

Figure 1.2: Schematic drawing of a proton exchange membrane fuel cell. Scanning electron micrograph of carbon fiber paper electrode is reproduced with permission from Electrochimica Acta, Lim, C.; Wang, C. Y., *49*, 4149-4156, Copyright (2004), Elsevier. Transmission electron microscope of PEM is reproduced with permission from Journal of Polymer Science Part B-Polymer Physics, Siu, A.; Pivovar, B.; Horsfall, J.; Lovell, K. V.; Holdcroft, S., *44*, 2240-2252, Copyright (2006), John Wiley & Sons.

1.3.3 The Membrane Electrode Assembly – Heart of the Fuel Cell

The MEA, illustrated in Figure 1.3, is likened to the heart of the fuel cell because it is here that chemical energy is converted into useful electrical energy.[10] Consequently,

a significant amount of effort has been invested to understand how the structure and interaction of each MEA component (e.g., catalyst, gas diffusion layer and PEM) interplay in the overall fuel cell performance.

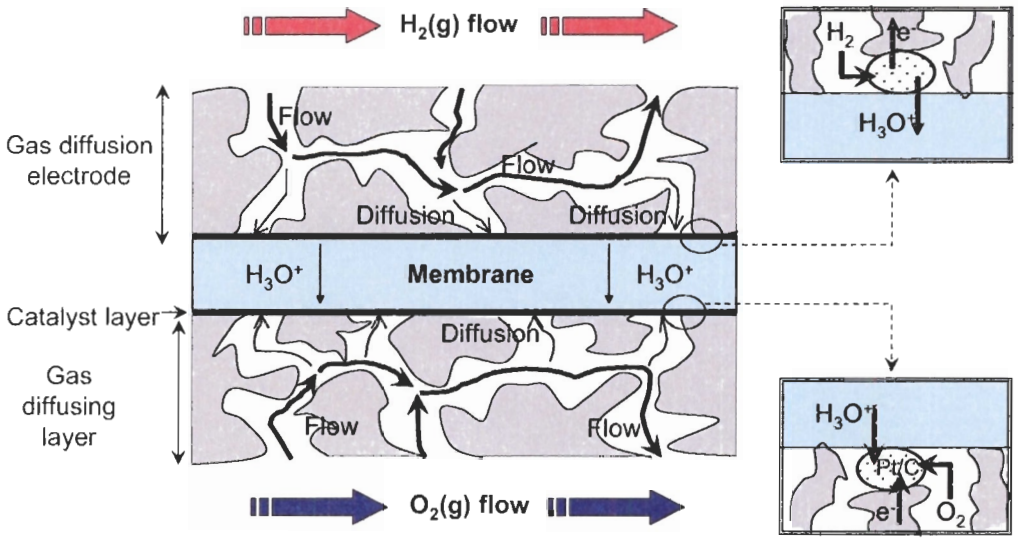

Figure 1.3: Schematic drawing of a membrane electrode assembly for a PEMFC.

1.3.3.1 Gas Diffusion Electrode

The electrodes consist of a catalyst layer and a diffusing substrate as illustrated in Figure 1.3. The gas diffusion layer serves several purposes: (1) it distributes reactant gases from the flow field channel to the catalyst layer, (2) it moderates liquid water transport from the catalyst layers so that the flow of gases to the catalyst layers does not get impeded, and (3) it conducts electrons and provides mechanical support to the catalyst layer. The most promising diffusion materials are those that are relatively stiff and highly porous ($\geq$ 70 %), and have high electrical conductivity. Gas diffusing materials are normally treated with 5 – 30 % poly(tetrafluoroethylene) (PTFE) to facilitate removal of product liquid water.[6]

The catalyst layer, at the membrane/electrode interface, is important to a fuel cell because poor construction often leads to a significant performance loss. It is made by depositing an ink slurry composed of a catalyst (e.g., Pt, Pt/C, Pt/Cr) and a proton conducting polymer binder (e.g., suspended Nafion® solution) and/or PTFE to a PEM or to a gas diffusion material (e.g., carbon fiber cloth) before the gas diffusing material is bonded to the membrane. The polymer binder serves many functions at the interface: It holds the catalyst, "glues" the electrode to the membrane, and transports protons from the membrane to the catalyst in the cathode or from the catalyst to the membrane in the anode. Molecular oxygen and hydrogen must often diffuse through this thin ionomer binder in order to reach the electro-active catalyst.[11,12] Delamination at the membrane/electrode interface is a concern because it results in fuel cell failure. This occurrence is most likely observed in fuel cells that operate under conditions that induce repetitive inhomogeneous interfacial stresses (e.g., when improper start-up and shutdown protocols are followed, or when the fuel cell freezes when liquid water is present at the interface), when incompatible binder and membrane materials are used, or when poor MEA bonding conditions are followed.[13-15]

Due to the large volume of water produced by the reaction and from water co-transported with protons by electro-osmosis, the cathode is prone to flooding if this water is not promptly removed, particularly at high current densities. Flooding can block delivery of reactant gases to the reaction site. Sometimes hydrophobic polymers, such as PTFE, are incorporated into the catalyst layer in order to open up existing pores and therefore decrease the propensity for water to accumulate.[16] Maintaining this balance is

vital to the operation of the MEA. This topic will be discussed in section 1.4 and in Chapter 4.

1.3.3.2 Proton Exchange Membrane

The principle functions of the PEM in a fuel cell are to conduct protons, prevent mixing of reactants, electronically isolate the electrodes, and act as a scaffold for the catalyst. The membrane should possess a combination of the following properties in order to be used: high proton conductivity; good mechanical and chemical integrity; low permeability to reactants; limited swelling in the presence of water; good capacity to fabricate into MEA's; and high electrical resistance.[17,18]

One well studied PEM is Nafion®, a perfluorinated polymer developed by DuPont in the late 1960's for the chlor-alkali industry. The chemical structure of Nafion® consists of a perfluorinated backbone with pendent vinyl ether side chains terminated with SO_3H (Figure 1.1). The high C-F content of the backbone of perfluorinated membranes ensures high chemical resistivity, a property that earlier versions of PEMs (e.g., poly(styrenesulfonic) acid membranes) lacked. The limited durability of earlier membranes was primarily due to the poor stability of C-H bonds towards oxidation caused by high cathode potentials and by small quantities of hydrogen peroxide formed at the electrodes (section 1.3.5).[9]

Although perfluorinated analogues with chemical structures similar to Nafion® but differing only in the length of the perfluorosulfonic acid side chain and the ion exchange capacity also exist (e.g., Aciplex, Flemion, and Dow),[17] Nafion® is the most

used PEM in the fuel cell industry because it is commercially available. For this reason, Nafion® is also the "technological standard".

Nafion® possesses good chemical and mechanical stability. It also performs well when adequately hydrated in a fuel cell. The excellent selectivity and transport of ions in Nafion® is attributed to the structure of the polymer. Small angle X-ray and neutron scattering reveal that it primarily has a bi-continous morphology.[19] Early studies proposed the existence of a network of ionic clusters (spherically inverted micelles) interconnected by narrow channels and embedded in a fluorocarbon medium that reorganizes upon hydration to provide a continuous pathway for ionic conduction. Although a true morphological model of Nafion® is still under debate, studies support claims that the positive attributes of Nafion® as a fuel cell membrane with respect to its high proton conductivity and mechanical integrity are related to its extensive nano-scale phase separation.[18,19]

Despite these positive attributes, Nafion® membranes do have critical drawbacks that limit their use: They are limited to fuel cells that operate below 80 °C, prone to dehydration, difficult to synthesize and process, and expensive to produce. Recycling of fluorinated polymers is also another concern. For direct methanol fuel cell (DMFC) applications (see section 1.5.2), Nafion® is also a poor methanol barrier. In H_2/O_2 fuel cells, the high osmotic drag coefficient of Nafion® leads to dehydration of the anode and/or flooding of the cathode, unless appropriate precautions are followed.[18] These shortcomings have spawned development of new membrane materials. Many of these alternatives are aromatic-based or partially fluorinated polymers for improved oxidative stability. A few examples are shown in Figure 1.4.

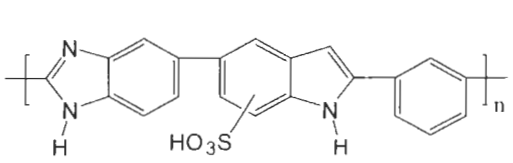

Sufonated
Polybenzimidazole

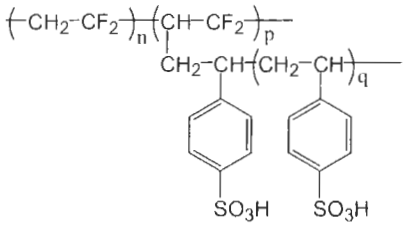

Irradiation grafted poly(styrenesulphonic)
acid on poly(vinyledene difluoride)

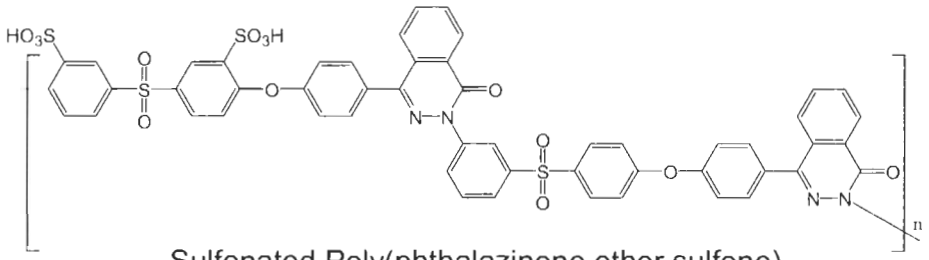

Sulfonated Poly(phthalazinone ether sulfone)

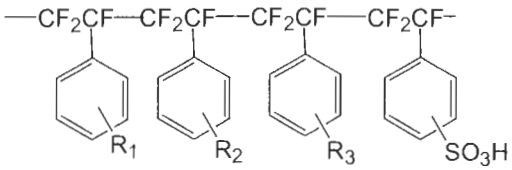

R_1, R_2, R_3 = alkyls, halogens, or, $CF{=}CF_2$, CN, NO_2, OH

Sulfonated poly(trifluorostyrene)

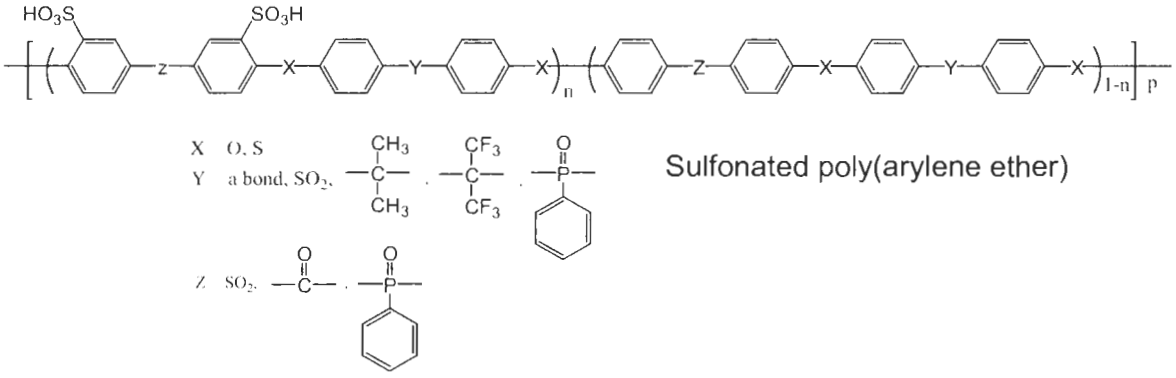

Sulfonated poly(arylene ether)

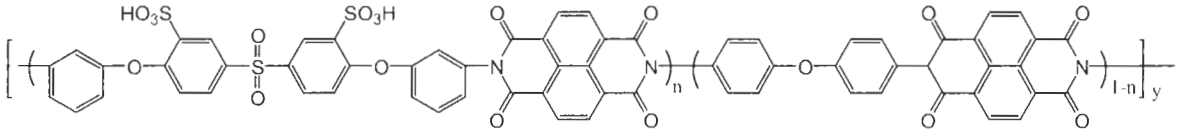

Sulfonated polyimide

Figure 1.4: Examples of alternate proton exchange membranes.[17]

The success of Nafion® and other PEMs as solid electrolytes rely on covalent bonding of hygroscopic -SO_3H acid groups to insoluble polymer segments. The amount of exchangeable -SO_3H in the membrane is normally expressed as a ratio of acid content determined by titration normalized to the mass of dry membrane in units of mmol of SO_3^- per gram. This ratio is defined as the ion exchange capacity (IEC) and controlling it tunes the amount of water a membrane can absorb as well as its proton conductivity.[17]

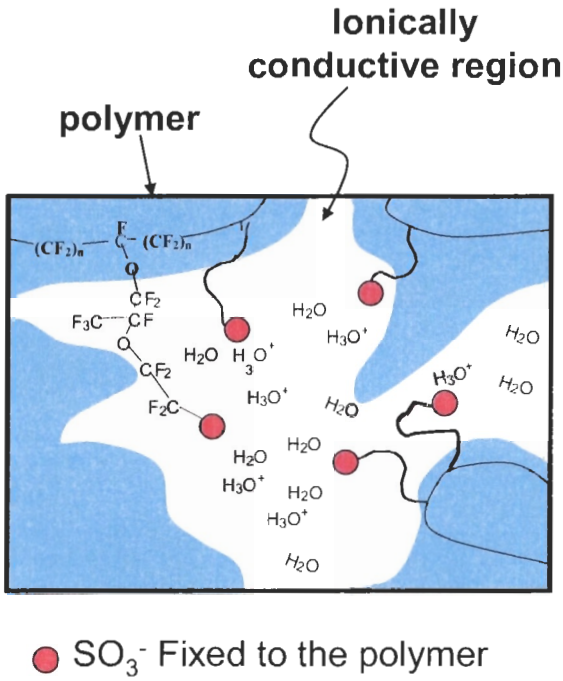

Figure 1.5: Schematic diagram of coalesced ionic clusters when the polymer absorbs water. The connected hydrophilic domains provide the pathway for proton conduction. Reproduced with permission from Journal of the Electrochemical Society, Yeager, H. L., Steck, A., *128*, 1880-1884, Copyright (1981), The Electrochemical Society.

The polymer structure re-organizes to provide a continuous hydrophilic network upon absorbing water (Figure 1.5). Nearly all existing PEM's rely on this water and its interaction with the acid groups to yield proton conduction. The strength of the acid groups is an integral part of the membrane design because transport of ionic current

depends on the mobility of protons as anions are fixed to the polymer. This is not an issue for strong acids, such as those employed in Nafion®. Electronic structure calculations for triflic acid and *para*-toluene sulfonic acid (in which the pKa's are approximately -6 and -2, respectively)[20] show that the respective proton dissociates from the anion upon the addition of the 3rd water molecules per sulfonic acid group (i.e., 3 H_2O/SO_3^-) to form a hydronium ion[21] (Figure 1.6). Calculations indicate that this requirement can be as low as 1 H_2O/SO_3^-, depending on the proximity between the sulfonic acids.[22]

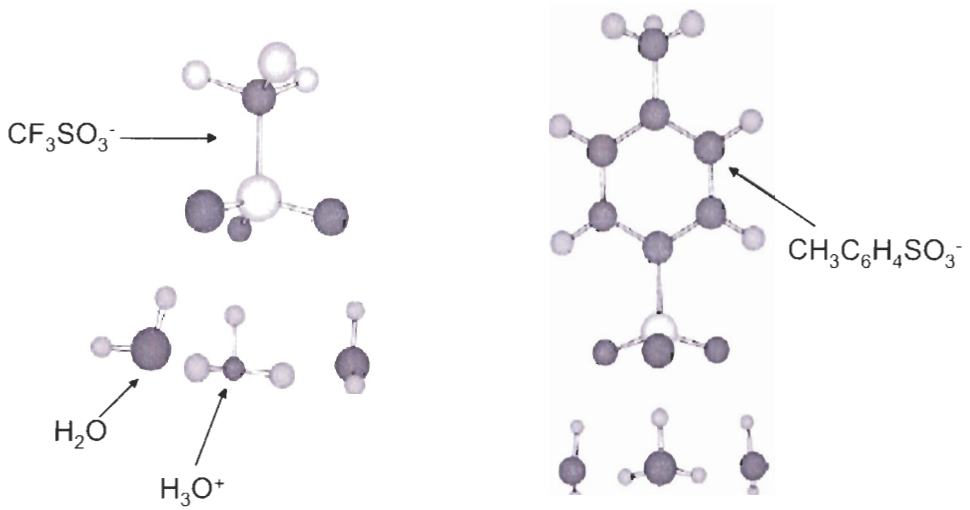

Figure 1.6: Fully optimized (a) triflic acid and (b)*para*-toluene sulfonic acid with 3 water molecules showing dissociation of acidic protons. In both cases, the dissociated protons form a hydronium ion, but its equilibrium position is closer to the sulfonate ion for the aromatic system. The close O-O distances between the anion and the hydronium ion are 2.56 Å and 2.49 Å for triflic acid and *para*-toluene sulphonic acid, respectively. Reproduced with permission from Journal of New Materials for Electrochemical Systems, Paddison, S., *4*, 197-207, Copyright (2001), Journal of New Materials for Electrochemical Systems.

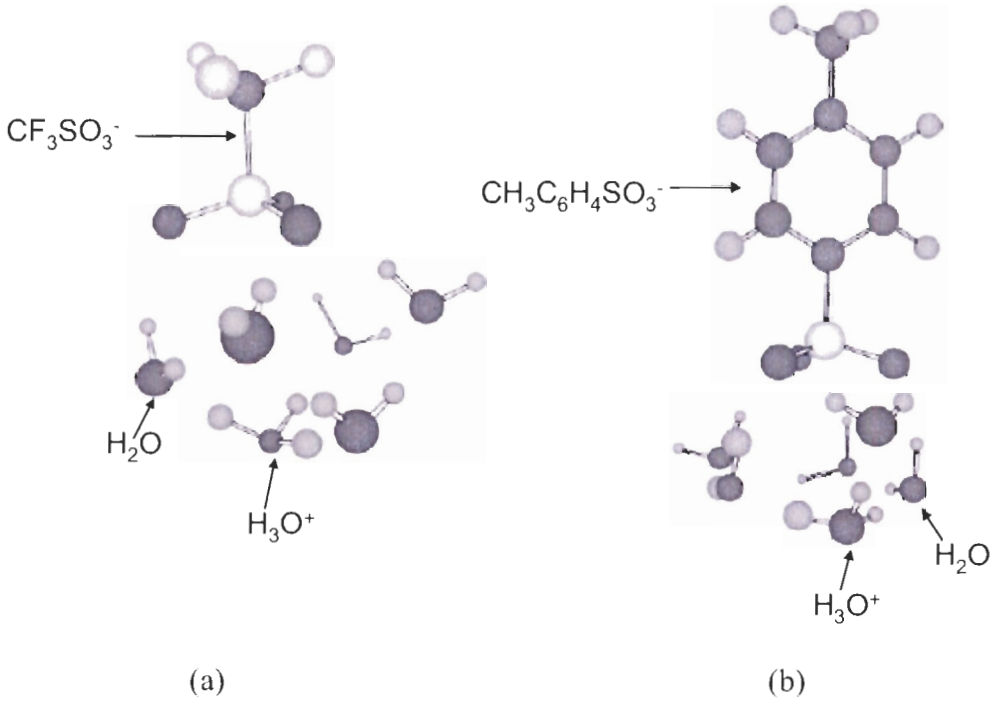

Figure 1.7: Optimized conformations for (a) triflic acid and (b) *para*-toluene sulphonic acid with 6 water molecules. The O-O distances of 4.24 and 3.64 Å between the anion and the hydronium ion for triflic acid and *para*-toluene sulphonic acid, respectively, indicate a well separated hydrated proton (or Eigen ion). Reproduced with permission from Journal of New Materials for Electrochemical Systems, Paddison, S., *4*, 197-207, Copyright (2001), Journal of New Materials for Electrochemical Systems.

Although dissociated, the SO_3^-/water/H^+ entity is still a contact ion-pair that cannot easily conduct protons. Theoretical calculations suggest that complete separation of the hydronium ion is observed only after the addition of the 6th water molecule.[23] Optimized conformations between the hydrated proton and SO_3^- are illustrated in Figure 1.7. Water molecules that form an intermediate hydration shell around the SO_3^- and the Eigen ion ($H_9O_4^+$, a hydronium ion surrounded by 3 water molecules) shield the proton from direct electrostatic interaction. This hydration shell (~ 5 H_2O molecules) appears to be necessary in order to give mobility to the protons. These calculations appear to be

consistent with IR spectra, quasineutron scattering experiments interpretations, and isopiestic sorption curve of Nafion® illustrated in Figure 1.8.[23-25]

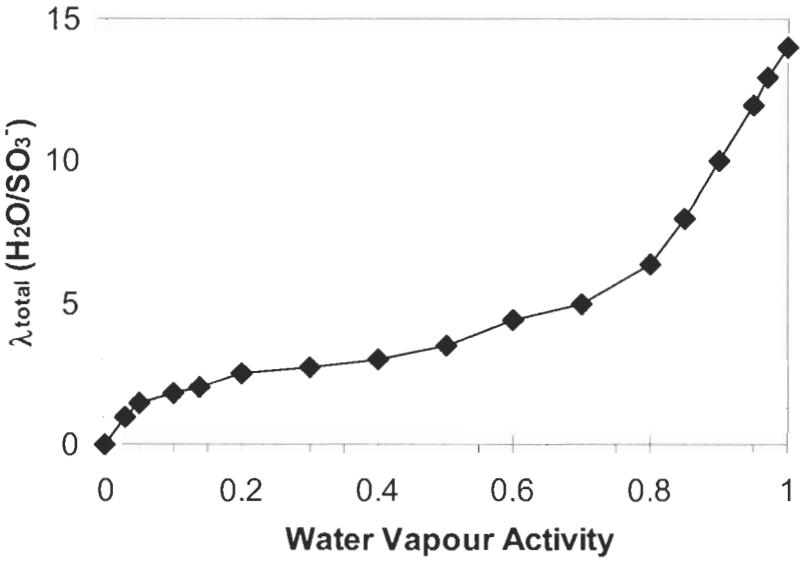

Figure 1.8: Equilibriumm sorption of water vapour as a function of water vapour activity. Data from Zawodzinski, T. A. Jr., Derouin C., Radzinski, S., Sherman, R. J., Smith, V. T., Springr, T. E.,Gottesfeld, S., *Journal of the Electrochemical Society* (1993) *140* (4), 1041 – 1047.

Designing a membrane that can transport protons in the presence of little or no water is desired for many applications - particularly in the automotive industry. For example, the U.S. Department of Energy has set a guideline of 120 °C and 50 % relative humidity as target operating conditions, and a proton conductivity of 0.1 S cm^{-1} for membranes used in automobiles.[17] However, this goal presents a significant challenge; understanding how the interaction between water molecules and acid groups in the ionic network affects proton conductivity is critical to the development of new PEM materials.

1.3.4 Cell Overpotential

When a cell is connected and current flows from the interface of an electrode, the potential of the electrode changes from E^{eq} (equilibrium potential when no current flows), to E (real potential). The difference between E and E^{eq} is known as the overpotential, η (equation 1.4). The overpotential of an electrode depends on the current, temperature and the composition of the electrode. It follows that $\eta > 0$ is an electrode at which oxidation prevails (i.e., anode), whereas $\eta < 0$ is an electrode at which reduction dominates (e.g., cathode).[26]

$$\eta = E - E^{eq} \tag{1.4}$$

For the same reason, when current flows from a fuel cell, the potential of the cell is reduced by an amount which corresponds to the sum of catalytic, Ohmic and mass-transfer overpotential losses, illustrated in Figure 1.9.[27]

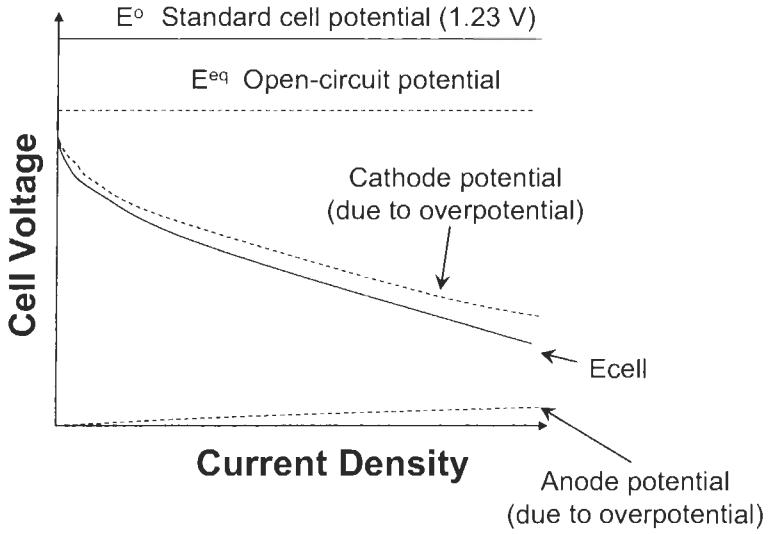

Figure 1.9: Change in the electrode potentials due to overpotential. Ecell = cathode potential – anode potential.

For a process in which the rate of the reaction is solely controlled by the rate of the electrochemical charge transfer process or the activity of the catalyst, η relates to the current density of kinetically controlled process through the Butler-Volmer equation (equation 1.5).[26] The left and right terms in the bracket of equation 1.5 correspond to the anode and cathode kinetically controlled current densities, respectively; wherein j^o is the exchange current density, α is the transfer coefficient, n is the number of electrons transferred in the reaction, and R, T and F are the ideal gas constant, temperature and Faraday's constant, respectively.

$$j = j^o \left[e^{\frac{(1-\alpha)F\eta}{RT}} - e^{\frac{-\alpha F\eta}{RT}} \right] \qquad (1.5)$$

An important parameter to note in the Butler-Volmer equation is the exchange current density. It represents the electrochemical reaction rate of forward and backward reactions when the system is at equilibrium. The exchange current density for hydrogen oxidation is quite high (~10^{-3} A cm^{-2}) in comparison to the exchange current density for oxygen reduction (~ 10^{-9} A cm^{-2}).[6]

The 10^6 – 10^7 orders of magnitude difference between the anode and the cathode reaction rates shows that oxygen reduction is the rate determining process in the fuel cell.[6] The sluggishness of oxygen reduction reaction (in comparison to hydrogen oxidation) is attributed to its small j^o value, and this is also the predominant source of potential loss in a PEMFC.[28] Although kinetic losses in the polarization profile can come from both half electrochemical reactions, the overpotential due to hydrogen oxidation is small in comparison to the overpotential due to oxygen reduction. For example, the

overpotential for hydrogen oxidation at 1 A cm^{-2} is estimated to be ~ 20 mV[9] whereas that for oxygen reduction is between 300 - 450 mV at moderate current densities.[29] This magnitude of voltage loss corresponds to approximately 30% of the cell's efficiency. The high overpotential for oxygen reduction is believed to be related to the stability of adsorbed oxygen on platinum at high potentials (particularly on Pt(111) surfaces).[28] It is believed that lowering the potential of the electrode decreases the stability of metal-oxygen bonds, which then allows the reaction to proceed.[28]

1.3.5 Cell Polarizations and Performance

Plotting cell potential as a function of applied current load is a common technique to evaluate fuel cell performance (often termed a polarization curve). A typical example of a fuel cell polarization curve is illustrated in Figure 1.10. The true cell voltage is reduced from an open circuit value or equilibrium cell potential value of 0.92 – 1.05 V for a H_2/O_2 system by an overpotential. This equilibrium potential rarely exceeds 1.1 V (slightly lower than the thermodynamic value for H_2/O_2 of 1.23 V) even in carefully prepared systems at standard state. This discrepancy is attributed to the existence of trace organic contamination, oxide formation, and/or platinum corrosion on the catalyst, permeability of reactants through the membrane, and variation in fuel cell operating conditions such as temperature.[6,27]

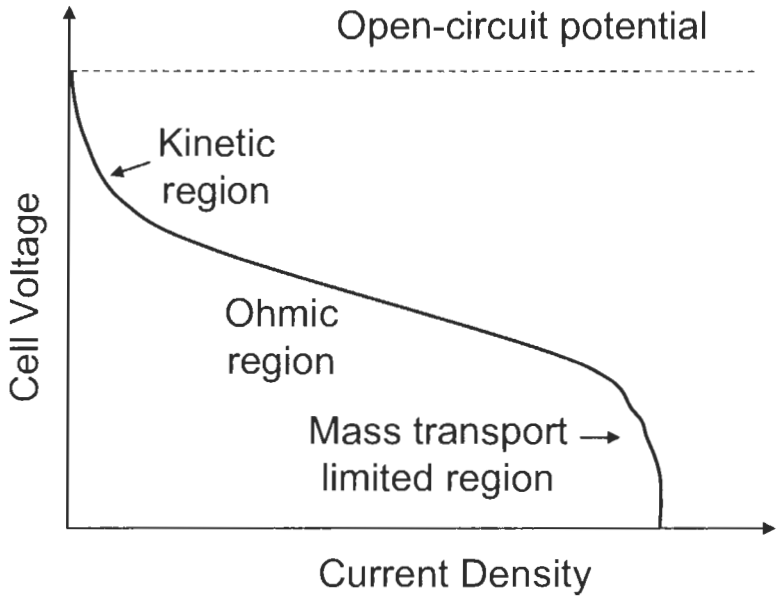

Figure 1.10: Example of a typical fuel cell polarization curve.

The different regions of the polarization profile indicate sources of potential loss in the fuel cell. The initial sharp potential drop at low current densities is primarily due to the sluggish kinetics of the oxygen reduction reaction at the electrode/electrolyte interface. The linear Ohmic region is related to internal fuel cell resistances such as membrane resistance, electronic resistance within the electrodes and interfacial resistance between components. The sharp decline of cell potential at high current densities (in the mass transport limited region) takes place when the rate of reactant reaching the catalytic site decreases below the rate of consumption. Impediment of oxygen transport to the reaction site by excess water (i.e., flooding) is common at the cathode in a PEMFC operating below 80 °C.[30-34]

With current state-of-the art technology, a single cell H_2/O_2 PEMFC delivers approximately 700 mA cm^{-2} at 0.7 V (~0.49 W cm^{-2}); however, a power density (power per surface area) as high as ~ 1.7 W cm^{-2} has been reported.[6] The exact power a fuel cell

can generate depends on many factors, including hardware design, type and thickness of membrane, catalyst loading, membrane/electrode interface, back-pressure of the reactants and the fuel used.

1.4 Water management

Water management is a term that describes the problems associated with maintaining appropriate water balance in the fuel cell during operation. One of these is to prevent the anode from drying due to electro-osmosis. Electro-osmotic drag is a phenomenon in which a solvent (or water in this instance) is co-transported with an ion as a hydration sphere, or along with the moving ion and solvent cluster due to hydrodynamic pumping. The number of solvent molecules co-transported with a proton is known as the electro-osmotic drag coefficient, and quantifies the extent to which electro-osmosis occurs in a given ion/membrane/solvent system.[35,36] Electro-osmosis depletes moisture from the anode, and saturates the cathode with water. In many cases, water is transported back (by back diffusion) to the anode.

Numerous studies exist in the literature that discusses on how to manage water in an operating fuel cell.[30-34,37-39] These studies primarily focus on: (1) new gas flow fields designs that reduce pressure loss along the serpentine gas flow channels, (2) new gas diffusion layers that help wick away excess water from the cathode to prevent flooding, (3) use of humidifier to hydrate the gas streams, (4) use of pressure difference across the membrane (normally between 5 – 15 psig) to help push excess water back to the anode, and (5) maintaining the membrane in a well hydrated state by controlling water transport and fluxes (Figure 1.11). Maintaining this balance is not only important for better cell

performance by reducing Ohmic and mass transport losses, but it also allows the cell to yield a reliable and steady electrical power output.

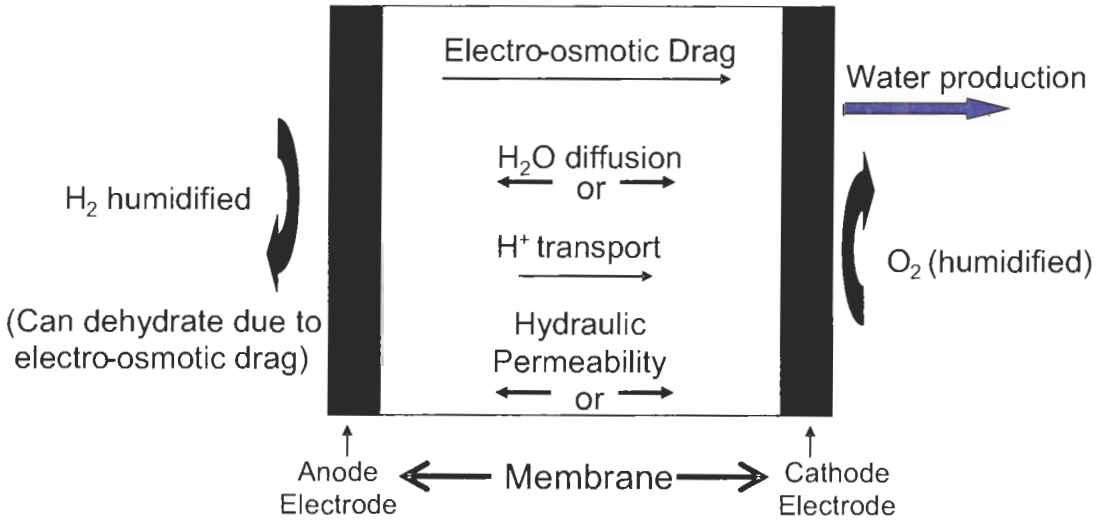

Figure 1.11: Schematic diagram illustrating the different modes of water transport within a fuel cell.

1.5 Fuels

Thermodynamic data and theoretical efficiencies of common oxidizable hydrogen-containing fuels are illustrated in Table 1.2.[6,40,41] Even though many of them yield high efficiencies in theory, H_2 (g) is still by far the most advanced and successful. Oxidation kinetics of low molecular weight hydrocarbons is often poor, and unreacted fuels often leak through the PEM. Permeated fuels reduce the fuel cell's fuel efficiency as well as its power density due to a combination of cathode de-polarization (which reduces the cathode potential), and a decrease in oxygen reduction rate (from direct combustion of fuel, and poisoning of the catalyst by molecular CO at the cathode for fuels containing carbon). For these reasons, hydrogen gas is still the most common fuel. Methanol, however, has also received significant attention due to its high energy density, as well as its ease of handling.

Table 1.2: Thermodynamic data for anodic fuel cell oxidation reactions at 25 °C, under standard conditions and ideal energy efficiency, with oxygen reduction as the cathodic reaction.

Fuel	(ΔH^{o}_{RXN} kJ mol^{-1})	ΔG^{o}_{RXN} (kJ mol^{-1})	Lower heating Value (MJ kg^{-1})[1]	Higher heating Value (MJ kg^{-1})[2]	E^{o}_{RXN} (V)	Ideal fuel efficiency (%)
H_2	-286	-237	120	142	1.23	83
Methane	-891	-818	50	56	1.06	91
Methanol	-727	-703	20	23	1.21	97
Ethanol	-1367	-1325	27	30	1.15	97
Propane	2221	-2106	46	50	1.09	95
Formic Acid	-270	-286	-	-	1.48	106
Diesel[3]	-	-	42 – 44	45 – 47	-	-
Gasoline[3]	-	-	42 – 44	44 – 47	-	-

[1] Defines the amount of heat released by combusting a specified quantity (initially from 25 °C), and then returning the combustion products to 150 °C. It assumes that the latent heat of vapourization for water is not recovered which typically represents ~ 10% of the total heat content. This value is commonly used in the petroleum industry to compare fuels where condensation of the combustion products is impractical, or heat at a temperature below 150°C cannot be put to use. [2] Defines the amount of heat released by a specified quantity of fuel (initially at 25 °C) and then returning the combustion products to 25 °C. Unlike the lower heating value, the higher heating value takes into account the latent heat of vapourization for water in the combustion products, and is useful in calculating heating values for fuels where condensation of the reaction product is practical. [3] Diesel and gasoline are not directly used as a fuel but are converted into hydrogen before supplying it to the fuel cell. RXN = combustion reaction e.g., $H_2(g) + ½\ O_2(g) \rightarrow H_2O(l)$ for when $H_2(g)$ is the fuel.

1.5.1 Hydrogen

Hydrogen gas is an excellent fuel because it has a high theoretical power density, reacts easily and produces water as the only product. Although many analysts agree that hydrogen derived from renewable resources, such as by electrolysis of water, is ideal, the realization of this technology for mass-market implementation will likely take many years due to the high costs of implementing appropriate fuelling infrastrusture.[2] Currently, much of the world hydrogen gas production comes from fossil fuels: 48 % by steam reforming of natural gas (equations 1.6 and 1.7), 30 % by processing crude oil products, 18 % by processing coal and 3% as a byproduct of the chlor-alkali process.[6]

Steam reforming is one of the common and mature processes for converting fossil fuel to hydrogen in high efficiencies (70 % - 89 %) for industrial use, such as to produce ammonia.[6,44] The first step involves desulfurization of the fossil fuel as sulphur is a poison to catalysts used in subsequent reactions. Steam is applied to the desulfurized fossil fuel at a high temperature (700 – 1000 ^{o}C) to produce a synthetic gas (syngas) mixture of CO and H_2 gases (equation 1.6) in a process that is referred to as reforming. Exposing the syngas to more steam further converts CO to CO_2 and generates more H_2 (water gas shift reaction, equation 1.7). The product is purified and further reacted to remove traces of CO (equation 1.8). As important as it is in the synthesis of ammonia to remove traces of CO from the reactants, hydrogen gas supplied to the anode of the fuel cell should also be free of CO because CO forms strong bonds on Pt surfaces, which lowers the number of available hydrogen oxidation sites. In this respect, hydrogen gas from reformate is not a zero emission fuel because the production of hydrogen releases greenhouse gases to the environment. Sequestration of CO_2 (g) (storing of CO_2 in unmineable coal seams, and oil and gas reservoirs) is currently being considered as a means to store and reduce CO_2 emissions into the atmosphere.[42]

$$CH_4\,(g) \text{ or any fossil fuel} + H_2O\,(g) \rightarrow CO\,(g) + 3H_2\,(g) \qquad (1.6)$$

$$CO\,(g) + H_2O\,(g) \rightarrow CO_2\,(g) + H_2\,(g) \qquad (1.7)$$

$$CO\,(g) + 3H_2\,(g) \rightarrow H_2O\,(g) + CH_4\,(g) \qquad (1.8)$$

Being small and light, a hydrogen molecule will penetrate through small cracks and holes of containment vessels very easily, and thus, will require special storage units. However, as hydrogen rises and disperses quickly, an explosive concentration of the gas is normally difficult to reach (unless it is trapped). The low density of hydrogen gas also means that less energy will be liberated in a given volume; therefore, hydrogen is also

much safer than either natural gas or gasoline.[43] The lack of appropriate infrastructures for the storage and distribution of hydrogen, however, is a huge roadblock for the commercialization of the hydrogen fuel cell. The use of on-board hydrogen generation by reforming hydrocarbons continues to be considered, but the complexity of implementing extra fuel processors and the associated costs in order to reform hydrocarbons have inhibited mass-market implementation of "on-board" hydrogen generation in the automobile industry.[44]

1.5.2 Methanol

The use of methanol as a "hydrogen carrier" has recently generated interest in specialized niche portable markets, such as in field-use laptops, cellphones and electric scooters, where fuel cells allow them to be used longer on a single charge. Methanol, being a liquid, is easy to re-fuel. It is also very economical to produce in large quantities from standard industrial processes (e.g., by reformed natural gas derived from either fossil fuels, or biomass sources in the presence of a catalyst) compared to hydrogen.[44]

As indicated in the preceding subsection, being able to omit the need for a separate fuel processor is a motivation for the development of direct methanol fuel cells (DMFCs). While the indirect methanol fuel cell (in which methanol is reformed to produce hydrogen) still remains under development, the DMFC is viewed to be more appropriate for portable systems because the design is less complex. The electrochemical oxidation of methanol in DMFCs produces protons, carbon dioxide and electrons, according to the following reaction:

$$CH_3OH\ (l) + H_2O\ (g) \rightarrow CO_2\ (g) + 6H^+\ (aq) + 6e^- \quad (1.9)$$

The cathodic reaction remains the same as in hydrogen PEMFCs

$$3/2\ O_2\ (g) + 6H^+(aq) + 6e^- \rightarrow 3H_2O\ (l) \quad (1.10)$$

Adding the half-reaction results in the following net equation:

$$CH_3OH\ (l) + 3/2\ O_2\ (g) \rightarrow CO_2\ (g) + 2H_2O\ (l) \quad (1.11)$$

As in a hydrogen PEMFC, protons are also transported through the PEM. In contrast to the hydrogen PEMFC, the anodic reaction in the DMFC is much slower because Pt cannot efficiently form $(OH)_{ads}$, which is needed to convert the intermediate species of methanol oxidation, (e.g., CO) adsorbed on the Pt surface to CO_2. The use of Ru alloyed to the Pt (i.e. Pt/Ru) has improved the rate of oxidation by enhancing formation of $(OH)_{ads}$ and, thus, the conversion of CO to CO_2.[6,45] However, this results in only a minor improvement in the rate of methanol oxidation.

The fact that Nafion® is a poor methanol barrier is also another challenge for DMFCs. The industry often uses a combination of a thick Nafion® membrane (e.g., 175 μm) and a low methanol concentration feed (~ 0.3 – 2 M) to minimize the amount of unoxidized methanol from permeating the membrane.[46] Methanol that transverses to the cathode occupies potential oxygen reduction sites and creates a mixed potential that lowers the open circuit potential and decreases the overall efficiency of the system.[7] Performance gains associated with lower methanol crossover are in most cases offset by a concurrent increase in membrane resistance of a thicker membrane. Because of these setbacks, the power density of a DMFC (~ 0.14 W cm^{-2} for a single cell) is often 5 to 10 times lower *versus* hydrogen PEMFCs.[7] While impractical for transportation

applications, these power densities are, nonetheless, sufficient to power small portable devices.[7]

1.6 Future prospects

The automobile industry is currently investing billions of dollars in research and development (R&D) of fuel cell cars, with the aim of replacing existing gasoline-powered engines with energy conversion devices powered by natural gas and/or other renewable energies. At the same time, they are also aiming at increasing the car's engine efficiency and at decreasing greenhouse gas and other tail pipe pollutants to very low or zero levels. Oil companies (e.g., Shell and BP) have increased investment in renewable energy and hydrogen generation.[2,10]

The EU and the US are also promoting activities that increase hydrogen production from natural gas, coal and renewable energy by providing political support and financial incentives.[2] Environment legislation in California, and USA Partnership for a New Generation of Vehicles program (PNGV) sponsored by the government of US and big US automobile manufactures, have stimulated a worldwide surge in fuel cell R&D for portable power, automotive and power generation applications.[9] The EU created the "EU Hydrogen and Fuel Cell Technology Platform" to bring about a secure and sustainable energy supply in which hydrogen and fuel cells play major roles. The platform has two main activities: to develop a "Strategic Research Agenda" and to develop a "Deployment Strategy". The former was launched in 2004 to address technical and non-technical issues related to hydrogen production, hydrogen distribution and storage (e.g., safety and standards), fuel cells for transport, fuel cells for stationary applications, portable fuel cells

and socio-economics. The latter action will focus on transition lines for hydrogen and fuel cell technologies, safety, codes, standards and possible commercialization routes.[2]

Successful implementation of a hydrogen economy from hydrogen derived from renewable resources requires major changes in current energy supplies. These changes are expected to encounter many barriers, and consequently, are expected to take many years to bring about.[2] A major barrier to a hydrogen economy is the slow progress of fuel cell commercialization. To help offset some of the initial capital cost, the US government passed an Energy Policy Act in 2005, which included a US $ 3.7 billion initiative fund to support hydrogen and fuel cell R&D. The bill includes a fuel cell tax credit of up to US $ 1 000 per kilowatt on the purchase of fuel cells used in residential or commercial applications.[5] The EU, through the Commission of the European Communities, will further support fuel cell and hydrogen R&D through a € 2.8 billion initiative between 2004 and 2015.[10]

At present, two of the most significant barriers to fuel cell commercialization are their high cost and insufficient reliability. Cost projections indicate that in order to compete with current technologies, fuel cells must not exceed € 50 kW^{-1} for private cars; € 200 – 300 kW^{-1} for buses; € 400 – 600 kW^{-1} for portable applications; and 400 – 600 kW^{-1} for cogeneration in buildings and power production.[2] The cost of a hand-made fuel cell at the moment is ~ € 3000 – 5000 kW^{-1}, of which 30 % is due to the actual cost of MEA materials, 37 % is due to bipolar plate materials and handling (e.g., machining of flow fields), 13 % is due to fuel cell assembling, and 14 % is due to endplates, testing, seals and gas diffusion layers.[10]

Mass production is expected to decrease the cost of fuel cells, but costs of key components, such as platinum and Nafion®, are not likely to decrease cost significantly unless a cheaper alternative is found. Major improvements have been made in membrane technology, and PEM alternatives to Nafion® will likely be available in the not too distant future for H_2/air systems. The use of as little as 0.25 mg Pt cm^{-2} total platinum in the fuel cell have also demonstrated reasonable power densities in H_2/air fuel cells[47], which will substantially lower the cost of the catalyst to ~ € 8 kW^{-1}. Achieving higher fuel cell power densities is also beneficial to lowering production cost. The use of fewer cells and less surface area to generate the desired power output, would require less material (i.e., MEA, bipolar plates, end plates and seals), and thus achieve a significant reduction in the overall stack cost.[2]

Even though cost reduction is promising for H_2/air PEMFCs, the use of hydrocarbon fuels, such as methanol or impure H_2 mixture (which contains remnant CO) will still require more R&D efforts to reach competitive cost targets. For example, the poor catalytic activity of catalyst for methanol in a direct methanol fuel cell system, requires a high platinum loading (e.g., ~ 2 mg Pt cm^{-2}). This amount would cost ~ € 400 – 800 kW^{-1} for a power density of 0.05 – 0.01 W cm^{-2}, too high to reach the € 50 kW^{-1} target for private automobiles.[2]

Insufficient fuel cell durability is still a major barrier to commercializing fuel cells, and industrial R&D groups, in particular, have devoted a great deal of resources to improve this. Lifetime requirements for fuel cell applications are 5000 h for private automobiles, 50 000 – 100 000 h for buses, and 40 000 – 100 000 h for cogeneration in buildings and power production. Analysis shows that the 5000 h for PEMFC driven

private automobiles with pure hydrogen seems achievable.[2] Other major applications, such as buses and stationary power production, which require extremely long lifetime operations, must overcome enormous hurdles. In the case of stationary power, the fuel cell industry faces strong competition from more mature technologies like wind-power, hydropower, biomass, and geothermal. Although the initial capital investment for these technologies is also high (~ $1 000 – $5 000 Cdn per kW, or € 700 - € 3 600 per kW)[48], their lifetimes are, however, much longer. Current cogeneration of heat and electricity using PEMFC with natural gas reformers have a guaranteed lifetime of 1 year.[2] In the case of buses and trucks, competition comes from hybrid, compressed natural gas, electrical and improved traditional gasoline and diesel engine designs. Some of these technologies are currently available commercially.[10]

Lifetime and reliability of PEMFC are strongly influenced by many factors. These include inappropriate water management within the cell, catalyst layer stability, purity of fuel and reactant crossover (which is a big problem for direct methanol fuel cells). Platinum catalysts are extremely vulnerable to low quantities (i.e., 2 – 10 ppm) of sulphur and carbon monoxide. Replacing the more economical, reformed hydrogen with ultra high purity hydrogen circumvents this problem. Membrane and catalyst layers are extremely sensitive to the amount of water in them. Flooding impedes delivery of reactants, whereas inadequate water reduces power density due to Ohmic losses and also causes irreparable damage to the membrane/electrode interface by creating hot spots that encourage material degradation.[2] The use of humidified gases usually solves the latter problem but adds parasitic losses and cost to the PEMFC. Fuel cell manufacturers have invested in studies that improved the PEMFC durability, but the basic research aimed to

understand the degradation mechanisms (particularly for the membrane and the catalyst layer) is lacking.

Some analysts predict that it is critical that fuel cells become commercially available, at least in selected niche markets within the next 5 years; otherwise, activities aimed at establishing a hydrogen society could peter out.[2] The following are considered as priorities by many analysts: (1) identify niche markets for kW size fuel cell applications that have high allowable costs and require short lifetimes (e.g., summer houses, yachts, electric wheel chairs, etc), (2) gain support from government to subsidize fuel cell systems (e.g., through tax incentives) to compensate for their higher price, (3) reduce cost and improve reliability and durability of the systems, and (4) reduce competitive pressures within the industry.[2,10]

1.7 Thesis Objectives

The focus of this thesis is on the solid polymer electrolytes for PEMFCs. An in-depth understanding of structure-property relationships is critical for the development of new PEM materials. The desired properties of a PEM vary depending on the operating conditions and the choice of fuel used. For instance, the aspect of low methanol crossover is important for membranes used in direct methanol fuel cells, but not for membranes in hydrogen fuel cells.

The diverse roles of a PEM rely on the existence of bi-continuous hydrophilic and hydrophobic phases in the polymer. The hydrophilic phase transports protons and water whereas the hydrophobic phase provides mechanical support. The interplay of both phases influences the properties of the material. Most of the synthetic methods currently

reported in the literature utilize a random or statistical placement of sulfonic acid units along the copolymer backbone to form the ion containing materials. Distribution of sulfonic acid groups along the chain, as well as the acid strength and the nature of the spacer group, between the polymer backbone and the ionic site, are deemed important to the morphology and the intrinsic properties of the membrane.[49,50] While it is desirable to maximize proton conductivity by increasing the content of $-SO_3H$ in the membrane, the inclusion of too many acid groups could induce excessive swelling, which compromise both the mechanical integrity and durability of the polymer, as well as encourage fuel crossover.[17]

Numerous literature work illustrates the importance of water on membrane transport;[19,51-54] however, it is still not very clear, from a quantitative perspective, how the interaction of water with the polymer affects transport of protons and other small molecules (e.g., methanol in the case of methanol permeability) through the membrane. The objectives for this work are to provide a better understanding of how the nature of sorbed water, which is a function of the material that constitutes the PEM, affects transport of protons, methanol and water. Graft copolymers (Figure 1.12) with well-defined structures were used in this work. Dr. Jianfu Ding synthesized the first set of polymers in our laboratory and Mr. Keith V. Lovell from Cranfield University in the UK provided the second set of polymers. These polymers allowed compositions and properties to be correlated.

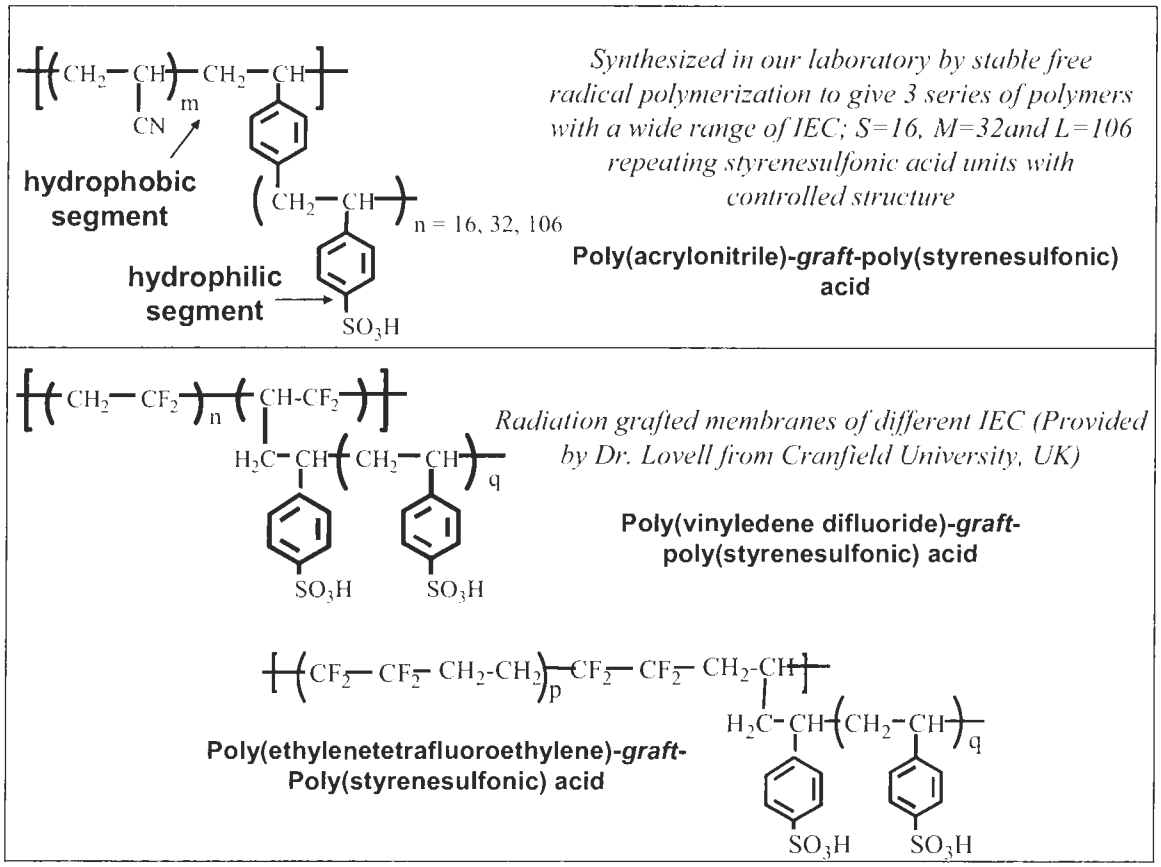

Figure 1.12: Polymer systems investigated in this work. Phase separation of incompatible hydrophobic and hydrophilic polymer segments were observed by transmission electron microscopy.

The distinction between the different states of water within the proton transporting conduit is difficult to discern in a real system because the rate of proton exchange in acidic water is high (10^{-12} s).[55] This is also evident by the single broad ^{1}H NMR observed in hydrated PEMs.[56,57] Nonetheless, the local environment of water in the ionic pores can still be probed by measuring the temperature at which water in the membrane freezes and the heat flow required for the phase change.[58,59] This method of analysis classifies water as either *freezable* or *nonfreezable*. Chapter 2 describes the use of low temperature differential scanning calorimetry to discern the environment of water molecules (freezable *versus* non-freezable), and how temperature and humidity influence

the relative disproportionation of water types. In addition, the chapter will also address how these parameters jointly affect proton conductivity, particularly at subzero temperatures and reduced humidity. Proton conductivity data of ETFE-*g*-PSSA and N117 membranes equilibrated at 25 °C and relative humidities between 85 % RH and the wet state were obtained by Ms. Jennifer Schmeisser. Ms. Amy Yang provided some of the sub-zero temperature proton conductivity data of the same membranes equilibrated at relative humidities between 45 and 85 %, and some of the proton conductivity data for the same membranes equilibrated at 25 °C and relative humidities between 45 – 85 % RH.

Currently, designing membranes that reject methanol while maintaining appropriate proton conductivity is a challenge because ionic domains that transport protons and water will also serve as conduits for the permeation of methanol. For the same reason, common approaches that increase proton conductivity by increasing the IEC or water content of the membrane also results in higher methanol permeability. Chapter 3 will discuss how the control of this water, in particular free water, influences methanol transport, as well as address how morphology and the nature of the polymer can have an affect on the permeability of methanol through the membrane.

Although *ex-situ* characterization could reveal the presence of adequate free water in some PEMs to sustain high proton mobility, assembling it in the fuel cell could still result in poor fuel cell performance if water in the fuel cell is poorly managed. Chapter 4 discusses the viability of implementing secondary non-ionic domains in order to alleviate the problem of anode dehydration due to electro-osmosis, and cathode flooding, which can lead to Ohmic and mass transport overpotentials. Dr. Titichai Navessin provided the

fuel cell data of HEMA-containing PVDF-*g*-PSSA. Mr. Keith Lovel of Cranfield University provided the modified PVDF-*g*-PSSA. Dr. Laurent Rubatat and Mr. Makoto Adachi provided the hydraulic permeability data for PVDF-*g*-PSSA and HEMA-containing PVDF-*g*-PSSA.

Chapter 5 is a summary and discussion of future work that may emerge after understanding how the nature and transport of water within the membrane affects its function. This knowledge might also lead to the development of new membranes that require little or no free water to function. Success in this area may allow fuel cells to operate with lower inlet gas humidication and less fuel cross-over.

CHAPTER 2:

STATE OF WATER IN POLY(STYRENESULFONIC) ACID-CONTAINING COPOLYMERS AND ITS EFFECT ON PROTON CONDUCTION

Sections of this chapter have been reproduced in part with permission from:

Journal of Physical Chemistry B, **2006**, *110* (12), 6072-6080

2.1 Introduction

A membrane with high proton conductivity is desired in order to decrease Ohmic losses in a proton exchange membrane fuel cell (PEMFC).[60] Succesful solid proton exchange membranes (PEM) generally rely on the presence of covalently bonded hygroscopic -SO_3H acid groups on insoluble polymer segments, as shown in Figure 1.2, to induce phase separation. The amount of exchangeable -SO_3H in the membrane is normally expressed as a ratio of acid content as determined by titration normalized to the mass of dry membrane in units of mmol per gram. This ratio is defined as the ion exchange capacity (IEC).[17] Small angle X-ray, neutron and atomic electron microscope studies indicate that on absorbing water the phase-separated morphology of Nafion® reorganizes to yield a continuous ionic/aqueous pathway upon coalescence of ionic domains.[18]

Protons are quite reactive as a free species because they lack an outer electron shell. They readily form multinuclear species with water molecules (e.g., H_3O^+, $H_5O_2^+$, $H_9O_4^+$) within the ionic phase of the membrane and are transported predominately by proton hopping (the Grotthuss Mechanism) and vehicular diffusion.[55,61] Although it is still under debate, it has been suggested that the contribution of the Grotthuss mechanism largely occurs through the center of the water-swollen phase, and consequently the proton mobility is higher in this region.[62,63] Counterviews suggest that the distinction between Grotthuss and vehicular conduction is not so clear-cut. In fact, the charge-carrying protons are undistinguishable from the "sea" of background protons and water;[61] and

"fixed", "free" or "excess" protons are not considered to exist *per se*; i.e., a proton, mobile in one moment of time becomes part of the next water molecule in the next. Furthermore, protonated clusters H_3O^+, $H_5O_2^+$ or $H_9O_4^+$ are considered mobile but short lived. Kreuer[55] estimates that hydrogen bond breaking and forming occurs at a rate of 10^{11} s^{-1}. Still, the Grotthuss mechanism is known to enhance proton transport because transport of alkali metal cations through perfluorinated membranes, where the mechanism is absent, occurs at a much lower rate.[64,65] Understanding the correlation between protons and water, and how they affect proton conductivity in the PEM is important in designing new membranes.

The nature of water molecules will depend largely on their immediate environment. Water molecules in the vicinity of polar groups will associate more strongly with the polar-head groups through hydrogen-bonding whereas those in the vicinity of nonpolar groups will associate less strongly.[66] In a much similar manner, water confined to the hydrophilic domains of the PEM will behave differently from bulk water because of these interactions. Numerous literature is available that attempts to understand how water influences the properties of a PEM (particularly Nafion®) using nuclear magnetic resonance spectroscopy, low angle X-Ray and neutron scattering, and calorimetry.[19,66] Despite many qualitative analyses, only a few articles are available that directly quantify the content of distinct types of water in the PEM.[19,66] This chapter will attempt to correlate this to proton conduction.

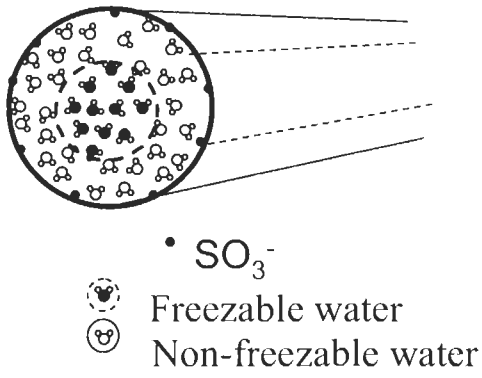

Figure 2.1: Cartoon representation of a hydrophilic cylindrical pore in Nafion®.

To correlate the equilibrium sorption and transport behariours, Pintauro *et al.*,[67,68] developed a simple model which describes Nafion® as an array of cylindrical pores with uniformly distributed fixed-charge sites on the pore walls shown in Figure 2.1. The hydrophilic cylindrical pores take up water when the membrane absorbs water. The electric field from the anion re-orients the dipole moments of nearby water molecules. The change in dipole moment of the water molecules from bulk-like water behaviour can be estimated by calculating the change in dielectric constant. The dielectric constant profile for water in Nafion® in Figure 2.2 points out that water between the normalized radial distance of 0 – 0.7 is still very bulk-like (< 10% change). This radial distance accounts for approximately 50 % of the total volume in the ionic pore. The dielectric constant for water at radial distance > 0.7 is much lower, indicating a shift from bulk-like behaviour.

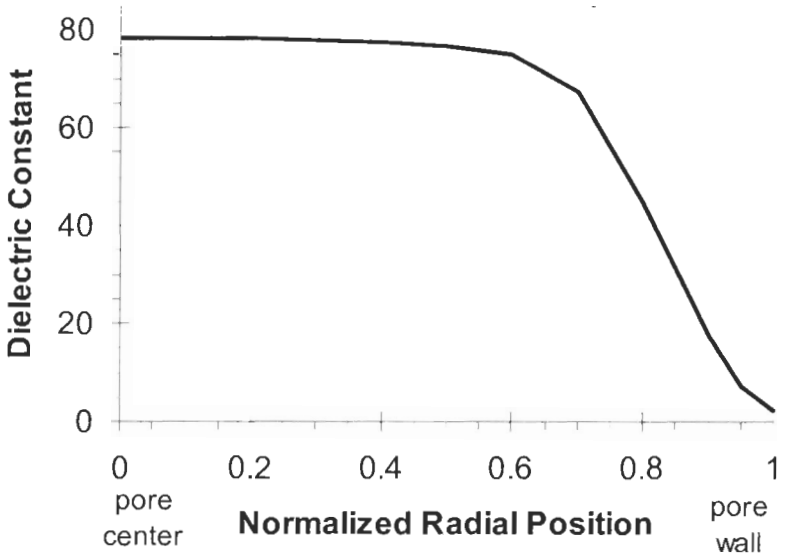

Figure 2.2: Calculated dielectric constant profile in a Nafion® 117 membrane pore after equilibration in a solution of 0.0625 M $Pb(NO_3)_2$ + 0.0625 M $CsNO_3$ + 0.125 M HNO_3. The dielectric constant is in the radial direction from pore center. The radius used in this model was 1.95 nm. Data from Yang, Y.; Pintauro, P. N., *Industrial & Engineering Chemistry Research* 2004, *43*, 2957 – 2965.

In a real system, the distinction between the different states of water within a membrane can be difficult to discern because all the water molecules are interchangeable and represent a continuum of states,[69] as indicated by the single broad ^{1}H NMR peak of hydrated membranes.[56,57] However, the local environment of water in ionic pores can still be probed by measuring the temperature at which water in the membrane freezes and the heat flow required for the phase change.[58,59] This method of analysis classifies water as *non-freezable* or *freezable*. Non-freezable water is water that is strongly bound to either the polymer backbone or the ionic groups that are associated with the polymer; non-freezable water yields no characteristic thermal transition in DSC analysis. Water molecules that are highly polarized by virtue of being in close proximity to an ion exist in

hydration shells and are unable to crystallize.[58,59] Freezable-water, whether only weakly polarized or liquid-like exhibits similar thermal transitions to bulk water.

A simplified schematic drawing illustrating the different types of water within an ionic pore is shown in Figure 2.3. Non-freezable water is situated along the wall of the ionic pore, whereas freezable water is located near the pore center. This depiction of the hydrophilic domain is supported by modeling, as well as by X-ray and neutron scattering work.[23,63,67,71] Water molecules that are not influenced by the electrostatic interaction of SO_3^- and which bear a close resemblance to bulk water are expected to crystallize first. The ice crystal will continue to grow with further decrease in temperature until the residual water molecules cannot re-orient themselves and pack into a crystal lattice, giving rise to non-freezable water.

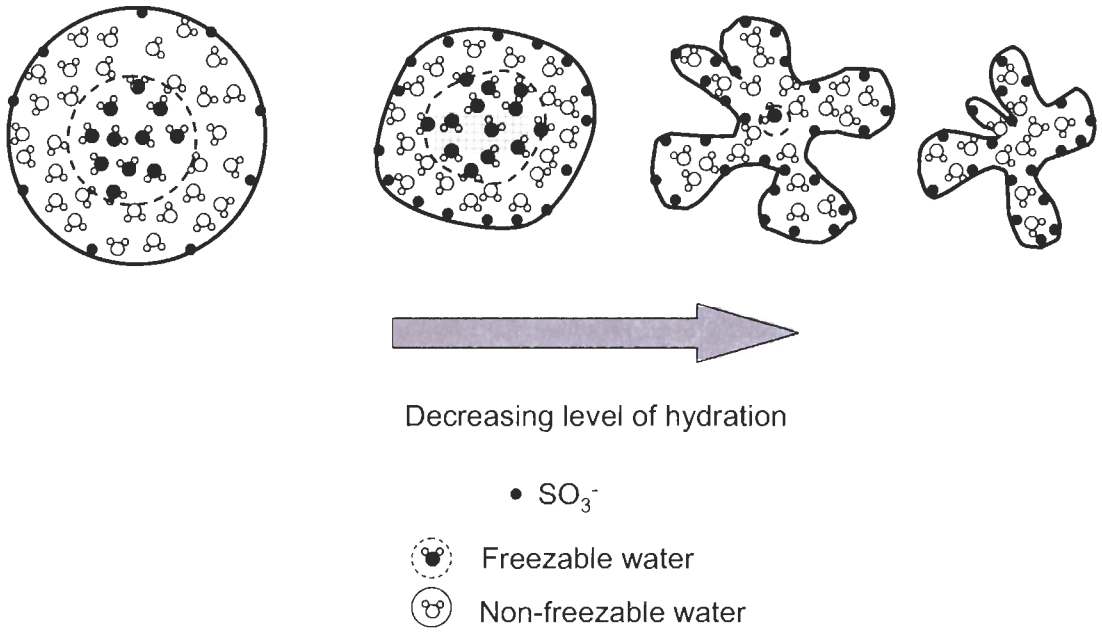

Figure 2.3: Schematic diagram illustrating the different types of water

Many studies show that water absorbed in hydrophilic polymer systems does not exhibit the same calorimetric,[72,73] diffusive[62] or spectroscopic[74,75] behaviour as bulk water.

In this work, the focus will be on using calorimetric techniques to probe the nature of water in PEMs containing various amount of water. Low temperature DSC measurements have been extensively used to study water in polymers, but it has mainly been applied to hydrogels.[76] A few reports are available for fuel cell membranes. Earlier work by Hietela[73] and Gupta[72] quantified the amount of freezable water by integrating the areas under the DSC curves and comparing the enthalpies calculated to that found for pure water. Kim and co-workers[52] showed that the different states of water can be measured indirectly by correlating the glass transition temperature of hydrated polymers, obtained by DSC measurements, with spin-spin relaxation times, T_2, obtained by ^1H NMR.

Two issues will be addressed: (1) the nature of water inside the polymer membrane and how it can be influenced by temperature and humidity, and (2) how these parameters jointly influence proton conductivity at the sub-zero temperatures and under reduced humidity. Sub-zero, low temperature conductivity of PEMs[77,78] has not been as extensively studied as high temperature conductivity (>100 ^oC)[79,80] even though it has relevance to low temperature fuel cell operation. Two types of membrane were examined: a series of experimental radiation-grafted ETFE-*g*-PSSA membranes that contain varying ionic contents, and commercially available Nafion® 117 (N117) (Figure 2.4) for benchmark comparison. The former, while being chemically susceptible to degradation under standard fuel cell conditions, are available with a range of IEC so that data can be compared, and the relationship between nature of water and proton transport be further understood.

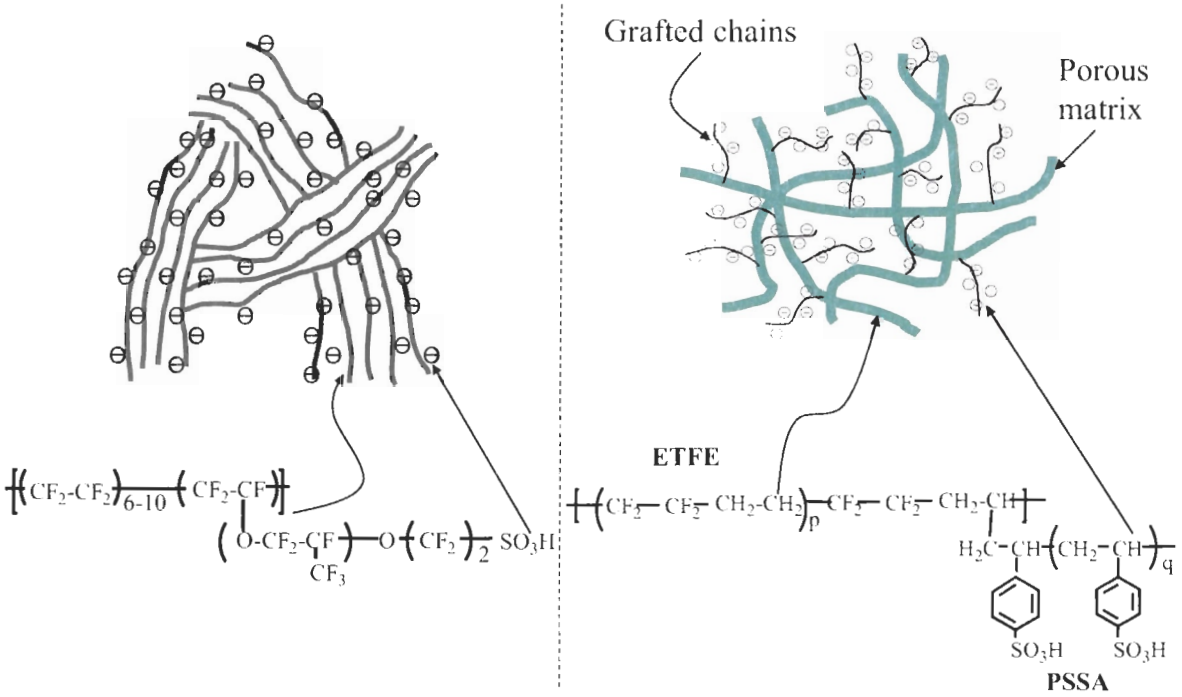

Figure 2.4: Cartoon representation of hydrated (a) N117, and (b) radiation-grafted ETFE-*g*-PSSA.

2.2 Experimental

2.2.1 Membrane Preparation

Radiation-grafted ETFE-*g*-PSSA membranes were provided by K. Lovell and co-workers (Cranfield University, UK). A detailed description of the synthesis of ETFE-*g*-PSSA membranes is described in detail elsewhere.[81] Briefly, a porous, preformed poly(ethylenetetrafluoroethylene) (ETFE) film (Du Pont) is exposed to gamma radiation and then immersed in styrene solution to initiate the graft polymerization of styrene. The length and density of the graft polymers is controlled by the conditions of polymerization. The styrene units are sulfonated to different degrees in order to provide a systematic variance in the ionic content of the membrane. The IEC of each membrane (mmol SO_3^- / g dry polymer) is provided in parentheses.

Nafion® membranes (from Ion Power) were boiled in 3% hydrogen peroxide solution for 30 min, and then in water for another 30 min. They were then boiled in 0.5 M H_2SO_4 for another 30 min. ETFE-*g*-PSSA membranes were soaked in 2 M H_2SO_4, and then soaked in MilliQ (Millipore) water to remove the excess acid.

Membranes were equilibrated from 99% to 45% RH in an ESPEC SH-241 humidity chamber at 25°C. Water-swollen membranes (wet) were equilibrated by immersion into Millipore water at room temperature.

2.2.2 Determination of Water Uptake and Water Content

Water-saturated membranes and membranes with 85 – 99 % RH were pat-dried with tissue paper and placed on a tared DSC aluminum pan. No significant loss of water was observed from the sample during the 1 min. assembly time (< 3%). Water uptakes were determined by heating the samples in a Hi-Res 2050 Thermogravimetric Analyzer (TA Instruments) from 25 °C to 350 °C at 5 K min^{-1}, and with a constant purge of nitrogen. The thermograms were analyzed using the Universal Analysis 2000 software (Version 3.9A). Water uptake and content values were determined from equation 2.1 and equation 2.2, respectively. The weight of dry membranes was determined from the point at which degradation of sulfonic acid begins (~ 288 °C). The content of water in membranes was also expressed as λ, a ratio of mmol H_2O to mmol SO_3^- (or), in order to account for differences in acid content between membranes.

$$\text{water uptake} = \frac{\text{weight of hydrated membrane - weight of dry membrane}}{\text{weight of dry membrane}} \text{ x } 100\% \quad (2.1)$$

$$\text{water content} = \frac{\text{weight of hydrated membrane - weight of dry membrane}}{\text{weight of hydrated membrane}} \times 100\% \quad (2.2)$$

2.2.3 Water Uptake in Membranes containing only Non-Freezable Water

The aforementioned procedure was modified in order to expediate the measurement process. Membranes between 85 % and 45 % RH were pat-dried with tissue paper and then weighed. The dried weight of the polymer was determined after drying it in a vacuum oven at 80 ^{o}C (28 mm Hg below atmosphere) for at least 10 h. As vacuum drying could not remove all the water bound from the polymer, the content of water uptake taken up by the membrane was estimated by adding together water uptake of membranes determined by vacuum oven to water uptake of already vacuum dried membranes. The latter was determined by following the same thermal gravimetric analysis as described earlier, and it accounted for residual water not removed by vacuum drying.

2.2.4 Ion Exchange Capacity and Acid Concentration

Ion exchange capacities (IEC) were determined by titration of acid released from the protonic form of the membranes in 2 M NaCl with sodium hydroxide. The estimated acid concentration, $[H^{+}]_{est}$, within the membrane was calculated using equation 2.3.

$$[H^{+}]_{est} = \frac{IEC}{\text{water uptake (\%)}} \times 100 \quad (2.3)$$

The volume fraction of water absorbed by the membrane at different humidities, X_v, was calculated by converting water content (ratio of water absorbed to hydrated membrane mass) into volume ratio using the density of bulk water (1 g mL^{-1}), and the density of the membrane at the humidity of interest, respectively, as described below:

$$X_v = \frac{\text{volume of water in membrane}}{\text{volume of hydrated membrane}} = \frac{\text{water content}}{\text{density of hydrated membrane}} \quad (2.4)$$

2.2.5 The State of Water in PEM: Freezable and Non-Freezable

The fraction of freezable-water in membranes was determined from differential scanning calorimetry (DSC) using a DSC Q10 (TA Instruments) calibrated against indium. The data was analyzed using the Universal Analysis 2000 software, version 3.7A. Samples were pat-dried with tissue paper, and quickly sealed in aluminum DSC pans. In a typical run, 2-7 mg of sample was cooled from 2 °C to −100 °C and then heated to 10 °C at 2 K min^{-1} under a nitrogen atmosphere. The content of freezable water in membranes was determined by integrating the area under the cooling curve and comparing it to the measured enthalpy of fusion for water (314 J g^{-1}). An example of this calculation is illustrated: The abscissa of the cooling thermogram, typically expressed in units of temperature, was converted to time using the 2 K min^{-1} scan rate. The area under thermal transion in the cooling curve (Figure 2.5) was integrated to provide an estimate of the heat released in unit Joules per mass of hydrated sample (J g^{-1}) for the crystallization of water in the membranes. The content of freezable water in units of mol g^{-1} was estimated by dividing the energy term by enthalpy of fusion for bulk water (314 J g^{-1}). Freezable water normalized to the membrane's acid content or $\lambda_{freezable}$ was calculated from equation 2.5.

$$\lambda_{freezable} = \frac{\text{freezable water in mol g}^{-1} \text{ x } 1000}{(1 - \frac{\text{water content in \%}}{100}) \text{ x IEC}} \quad (2.5)$$

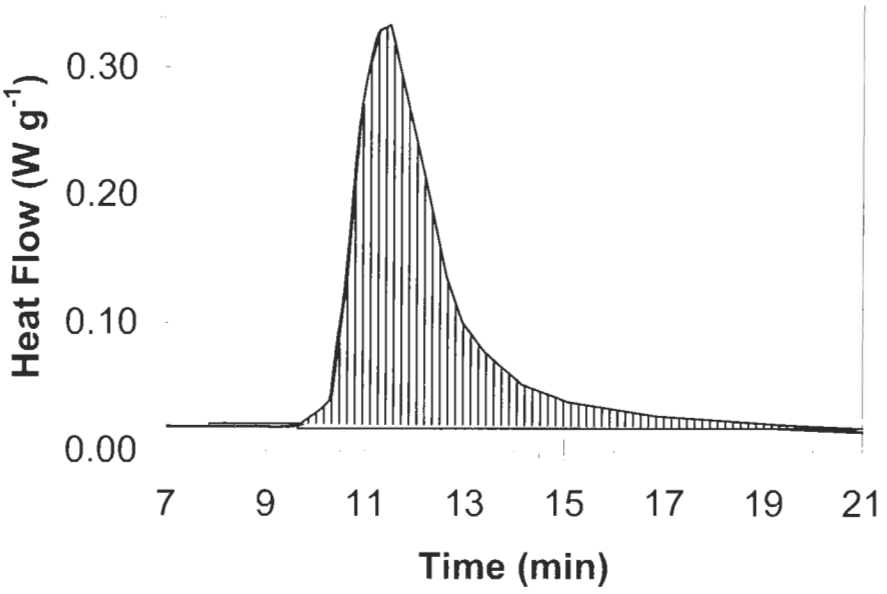

Figure 2.5: Integration of area under the cooling curve to estimate the heat required for crystallization of water in the membranes.

From equation 2.6, (in which W_f is the fraction of freezable water, W_{nf} is the fraction of non-freezable water and W_t is the total water in the membrane) the total water in membranes should simply be the sum of freezable and non-freezable fractions.

$$W_f = W_t - W_{nf} \tag{2.6}$$

2.2.6 Proton Conductivity

The in-plane proton conductivities of the samples were measured using a Hewlett Packard 8753A Network Analyzer. A strip of membrane was set between 2 Pt electrodes, as shown in Figure 2.6, and an alternating current was passed through the plane of the sample. Nyquist plots between 300 kHz and 1 MHz were obtained from the samples. Membrane resistances were extrapolated by fitting the data to the standard Randles equivalent circuit. A Solartron 1260 frequency analyzer was also used to extend

the frequency limit of the measurements. In this case, an alternating current between 10 MHz and 100 Hz and amplitude of 100 mV was applied.

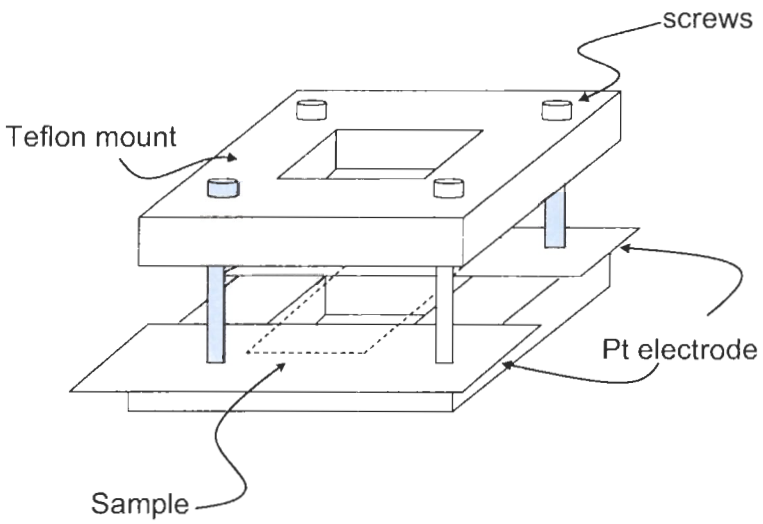

Figure 2.6: Schematic drawing of the proton conductivity probe.

Proton conductivities were calculated using equation 2.7, where L is the distance between electrodes, A is the cross-sectional area of the membrane, and R_m is the resistance of the membrane.

$$\sigma = \frac{L}{R_m A} \tag{2.7}$$

2.2.7 Controlling the Humidity of Samples for Low Temperature Proton Conductivity Measurements

Water-saturated samples were mounted in the conductivity probe and sealed in a plastic bag which contained a piece of wet kimwipe in order to keep the membrane water-saturated during the experiment. The temperature of the sample was lowered in a systematic manner, and held until a steady proton conductivity value was obtained.

Stability studies showed that the proton conductivity values were relatively stable over the time scale of the experiment.

Humidity of membranes equilibrated between 99 % - 45 % RH at 25 °C was maintained by sealing them in a jar. Pre-equilibrated samples were mounted into a conductivity probe and inserted into a jar half-filled with epoxy. Strips of wet kimwipe or membranes were placed in the jar to prevent the membrane from excessive dehydration. The sample was then allowed to re-equilibrate at 25 °C for 1 week. The exact humidity of the sample later was determined by comparing the conductivity of the re-equilibrated sample to a calibration chart. The temperature of the sample was then systematically decreased and allowed to equilibrate until a steady value was obtained (~ 5 – 6 hours). Similar proton conductivity values were obtained before and after temperature ramping. In addition, system stability investigations, which compare proton conductivity measured at the end of 1 week (i.e., for -37.5 °C) to proton conductivity measured when the sample is cooled directly from 25 °C at the beginning of the experiment, indicate that the system is very stable.

Multiple measurements were performed for all the experiments in order to estimate the standard deviation and the reproducibility of the data.

2.3 Results

2.3.1 Proton Conductivity of Water Saturated Membranes at Low Temperature

The IEC of ETFE-*g*-PSSA membranes depends on the degree of grafting of sulphonated styrene on the ETFE matrix (Table 2.1). Increasing the degree of grafting increases the IEC, the water uptake and the corresponding λ values (H_2O/SO_3^-). A higher

IEC leads to a disproportionate increase in water uptake and results in a decrease in $[H^+]_{est}$.

Table 2.1: Properties of fully hydrated N117 and ETFE-*g*-PSSA membranes at 25 °C.

Sample (IEC /mmol g^{-1})	Degree Grafting (%)	Water uptake (%)	λ (H_2O /SO_3^-)	$[H^+]_{est}$ (M)	σ (S cm^{-1})	$\lambda_{freezable}$ [a] (H_2O /SO_3^-)	μ_{est} [b] x 10^3 (cm^2 s^{-1} V^{-1})
ETFE –g-PSSA							
(2.13)	32	69	22	1.8	0.15	9	0.85
(2.50)	34	111	24	1.5	0.17	12	1.19
(3.27)	46	186	28	1.3	0.20	16	1.59
N117 (0.97)	-	36	20	1.1	0.09	9	0.87

[a] Obtained by DSC, presented in detail in subsequent sections. [b] Calculated from equation 2.8.

In the context of a previous classification of proton conductivity in membranes[82] these series are classified as *water-poor* because the presence of additional water enhances proton conductivity *via* enhancement of proton mobility - as opposed to additional water which lowers conductivity through a dilution effect. Even though Nafion® possesses the more acidic entity, triflic acid, the higher conductivity seen for ETFE-*g*-PSSA can be attributed to its higher $[H^+]_{est}$ and $\lambda_{freezable}$. The larger fraction of freezable λ ($\lambda_{freezable}$) due to the larger water uptake of the membrane presumably reduces the extent of ionic interaction in the hydrophilic channels and increases the mobility of the protonic species.

The points noted here suggest that *free* or *freezable* water is important to proton conduction. To further evaluate the impact of freezable water on membrane conductivity,

proton conductivities of fully hydrated membranes were measured at sub-zero temperatures to systematically control the content of freezable/free water in the polymers.

Examples of Nyquist plots for ETFE-*g*-PSSA (3.27) and (2.13) at -10 °C are illustrated in Figure 2.7. Nyquist plots for other membranes and for N117 at other temperatures were similar in nature, varying only in the diameter of the arc, from which proton conductivity is determined.

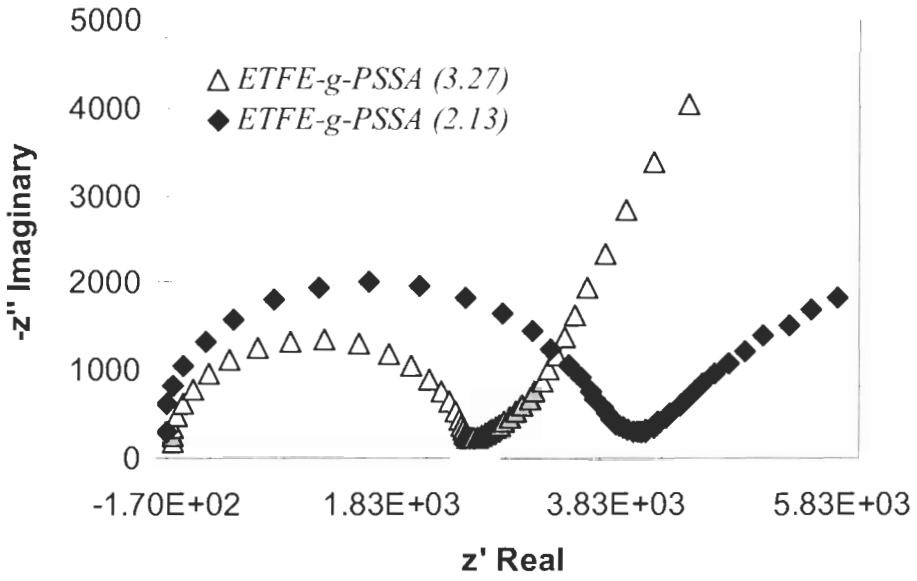

Figure 2.7: Nyquist plots of hydrated ETFE-*g*-PSSA (3.27) and (2.13) at -10 °C.

Plots of proton conductivity between 25 °C and -37.5 °C for fully hydrated N117 and ETFE-*g*-PSSA (2.13 and 3.27 mmol g^{-1}) membranes are shown in Figure 2.8. Two sharp breaks are visible in the plots. The proton conductivity for N117 falls from 0.093 to 0.049 S cm^{-1} upon reducing the temperature from 25 °C to –3 °C. The latter is associated with the onset of freezing. Crystallization of water in N117 continues until -20 °C (see DSC in Figure 2.12 (a)) with proton conductivity concomitantly falling from 0.049 to 0.012 S cm^{-1} (~1/4 of its original value). A further decrease in temperature to

-37.5 °C causes the conductivity to drop to 0.002 S cm^{-1}. The proton conductivity of ETFE-g-PSSA (3.27 and 2.13 mmol g^{-1}) decreases from 0.195 to 0.105 S cm^{-1}, and from 0.145 to 0.080 S cm^{-1}, respectively, between 25 °C and -3 / -5 °C. Similarly to Nafion®, the latter temperature corresponds to the onset for freezing of water in the polymer. Reducing the temperature to -10 °C (corresponding to the freezing of water) causes the conductivity to decrease to 0.030 S cm^{-1} for both membranes (~ 5- 6 times smaller than its original value). Decreasing the temperature to -37.5 °C further decreases the conductivity to 0.004 and 0.003 S cm^{-1}, respectively. The sharp drop in conductivity due to the freezing of water is shifted to -3 °C and -5 °C for ETFE-*g*-PSSA (2.13) and (3.27), respectively. Although the conductivities for both ETFE-*g*-PSSA membranes and N117 are significantly different from one another between 25 °C and the onset of freezing, their proton conductivities converge to a similar value after the "free" water has crystallized.

Arrhenius plots of proton conduction between 25 °C to -37.5 °C are presented in Figure 2.9. The activation energies for proton conduction above the freezing of water is calculated to be 0.15 eV for wet N117, which is very similar to published data,[77,78,83] and 0.14 eV and 0.15 eV for wet ETFE-*g*-PSSA (2.13) and (3.27), respectively. The magnitude of the activation energies are similar to that found for proton conduction in bulk water.[84]

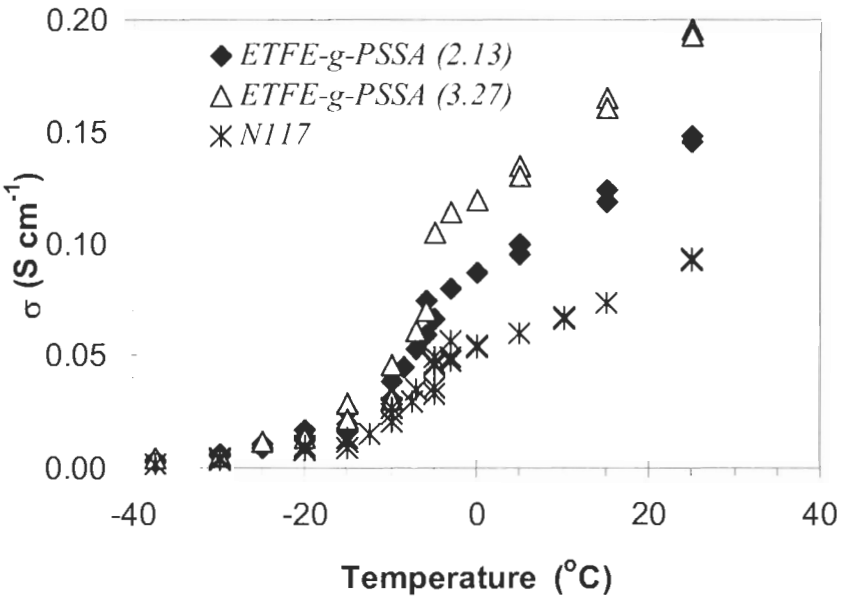

Figure 2.8: **Proton conductivity, σ, of fully hydrated ETFE-*g*-PSSA (2.13), ETFE-*g*-PSSA (3.27), and N117 membranes between 25 and -37.5 °C.**

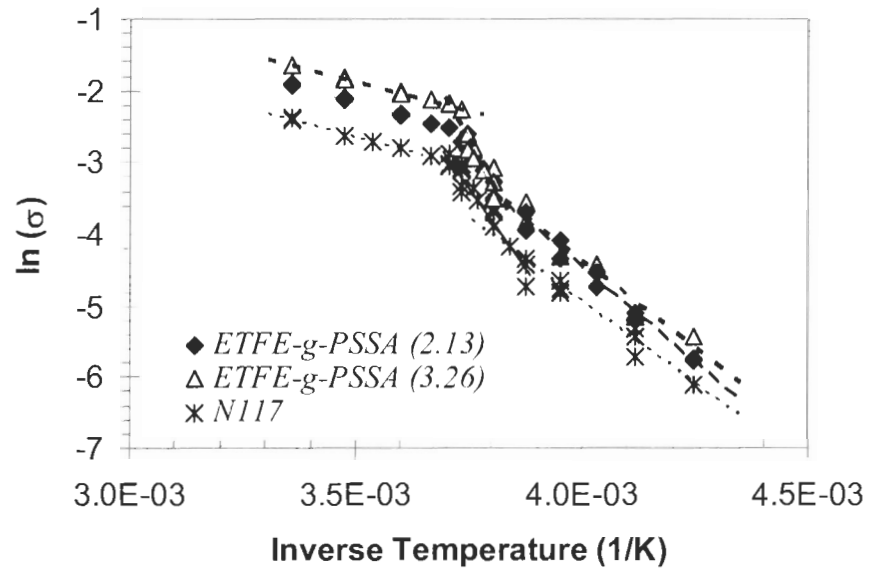

Figure 2.9: **Arrhenius plots of water-swollen N117, ETFE-*g*-PSSA (3.27), and ETFE-*g*-PSSA (2.13) membranes between 25 and -37.5 °C.**

The activation energy for proton conduction in the temperature region corresponding to frozen membranes is 0.4 eV for N117; and 0.4 eV and 0.5 eV for ETFE-*g*-PSSA (3.27), and (2.13), respectively. Data for N117 agree with reports published by Uosaki[78] and Cappadonia.[77,83] Although the value of ~0.5 eV is close to the activation energy found for proton conduction through polycrystalline ice,[77,85] proton conductivity through ice is much lower (~ 10^{-7} S cm^{-1} at ~ -13 °C) [86] because the mobility of protons through ice is also quite low (~ 7 x 10^{-10} cm^2 V^{-1} s^{-1}).[87] The high activation energy may be attributed to the strong molecular resistance induced by water molecules being in close proximity to an electric field (e.g. sulfonic acid groups), and infers that non-freezable water may be relatively immobile, but still able to transport protons.

A remarkable feature of this data is that proton conductivity decreases only by a factor of 4 for Nafion®, and ~ 5 - 6 for ETFE-*g*-PSSA (3.27) and (2.13), respectively, upon freezing the water inside the membranes. By inference, residual (unfrozen) water still exists in the membrane and this water facilitates proton transport under these temperature regimes. The rest of this paper is devoted to further understand how the different states of water affect proton conductivity. This investigation is achieved by controlling the ambient humidity in order to reduce λ, and by using aforementioned DSC measurements to determine the nature of water in membranes with different levels of hydration.

2.3.2 Relationship Between λ, Relative Humidity and Proton Conductivity

TGA and DSC measurements were performed on samples equilibrated at different RH. Their λ values, calculated from TGA data after equilibrating the membranes in liquid water, and at 99%, 95%, 90% and 85% RH at 25 °C, are shown in Figure 2.10 (a).

λ is highest in wet membranes and decreases with RH. Water content is greater in ETFE-*g*-PSSA than in N117 membranes for a given RH, indicating that the elastic forces of the former are weaker and/or the osmotic driving force is greater. Nevertheless, λ converges to a common value for all samples at lower RH, which can be attributed to the loss of liquid-like water and the persistent presence of residual ion-bound water.

The proton conductivities of N117 and ETFE-*g*-PSSA membranes at different humidities are shown in Figure 2.10 (b). The increase in proton conductivity with increasing sulfonic acid content is a trend that agrees with other reports.[79,88,89] At 99% RH, the conductivity of ETFE-*g*-PSSA membranes is ~ 2 times greater than N117. At 85% RH, the conductivity of N117 is still lower than ETFE-*g*-PSSA even though λ values for both polymers are similar (~8 H_2O/SO_3^-). In spite of the loss of free water at 85% RH (see below), proton conductivity is still reasonably high for both polymer series, suggesting that non-freezable water transports protons reasonably well.

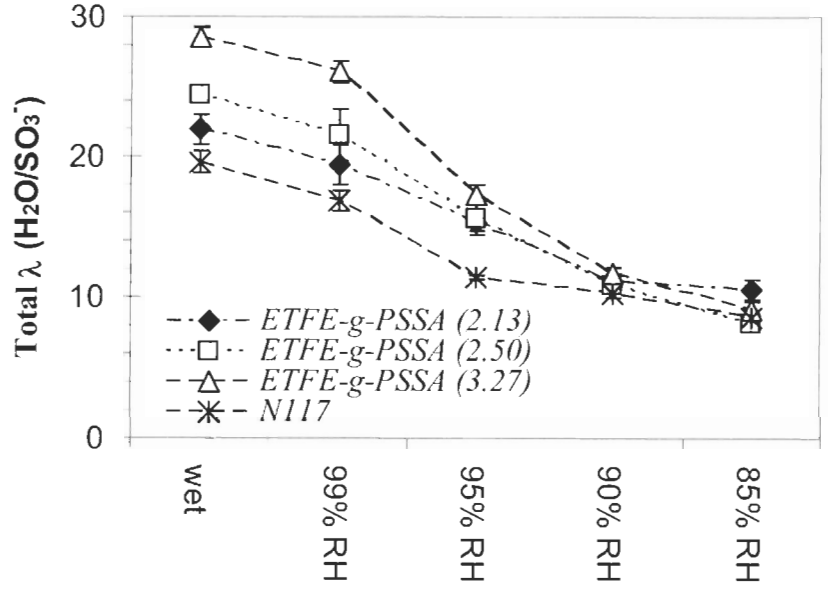

(a)

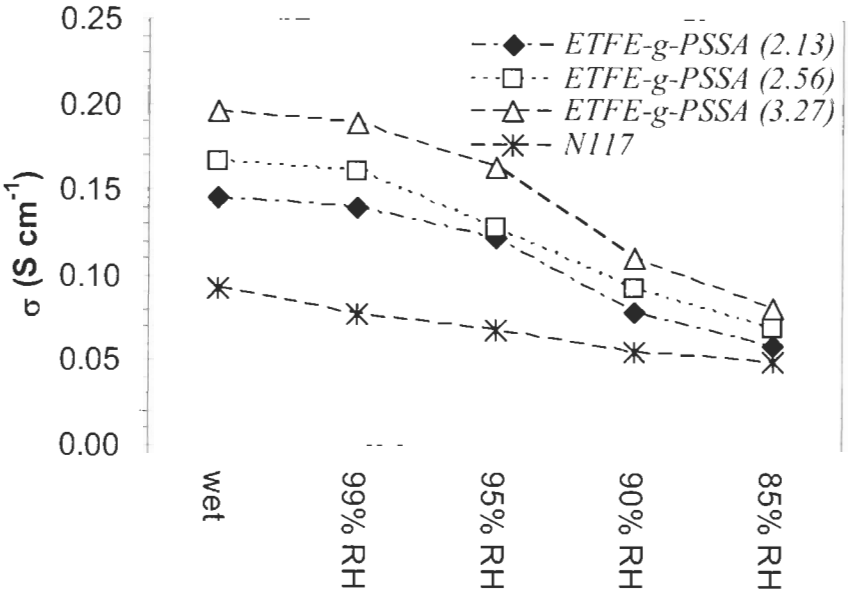

(b)

Figure 2.10: (a) Change of total λ (determined by TGA). (b) Proton conductivity, σ, for N117 and ETFE-*g*-PSSA membranes as a function of membrane humidity.

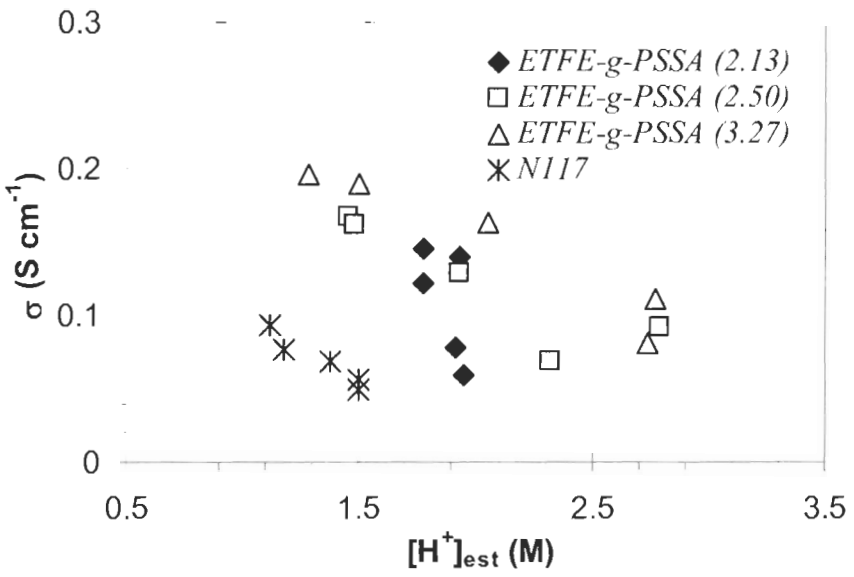

Figure 2.11: Change of proton conductivity, σ, as a function of acid concentration, $[H^+]_{est}$, for N117 and ETFE-*g*-PSSA membranes. The $[H^+]_{est}$ was varied by controlling RH.

2.3.3 Effect of Acid Concentration on Proton Conduction.

The acid concentration for each membrane was estimated based on the density of bulk water. The correlation between conductivity and the estimated acid concentration for the two types of polymers at different humidities is shown in Figure 2.11. The data shows that conductivity decreases with a decrease in membrane humidity - the result of the materials being *water-poor* in the context of proton conductivity.[82] Reducing λ further (by lowering RH) has an adverse effect on proton mobility because the increased ionic interaction associated with higher $[H^+]_{est}$ can retard the mobility of protons and offset the benefit of the higher number of charge carriers in the pore. This phenomenon is illustrated in two of the three cases of the ETFE-*g*-PSSA series. In a direct comparison, ETFE-*g*-PSSA (2.50) and (3.27) for which $[H^+]_{est}$ is clearly lower, the λ values are higher and hence it is inferred that conductivity is enhanced by the increase in proton mobility.

2.3.4 On the Nature of Water.

Low temperature DSC was used to quantify and elucidate the different types of water (freezable *versus* non-freezable) in the polymer electrolytes. DSC traces of water-saturated samples, and of membranes with 99 % to 85 % RH, were acquired. A thermogram of fully-hydrated N117 is shown in Figure 2.12 (a). The exothermic peak is due to freezing of water within the hydrophilic regions of the membrane; the corresponding endothermic peak is due to the melting of frozen water. The onset of fusion at a lower, sub-zero, temperature compared to the melting transition illustrates the known super-cooling phenomenon of water. Membranes exposed to lower RH provided similar thermograms. Calorimetric thermograms of ETFE-*g*-PSSA membranes and of N117 at different humidity were similar in nature to N117, but the position of the transitions and the integrated areas of the peaks varied. The change in the thermograms for ETFE-*g*-PSSA (3.27) as a function of exposure to different humidities are illustrated in Figure 2.12 (b).

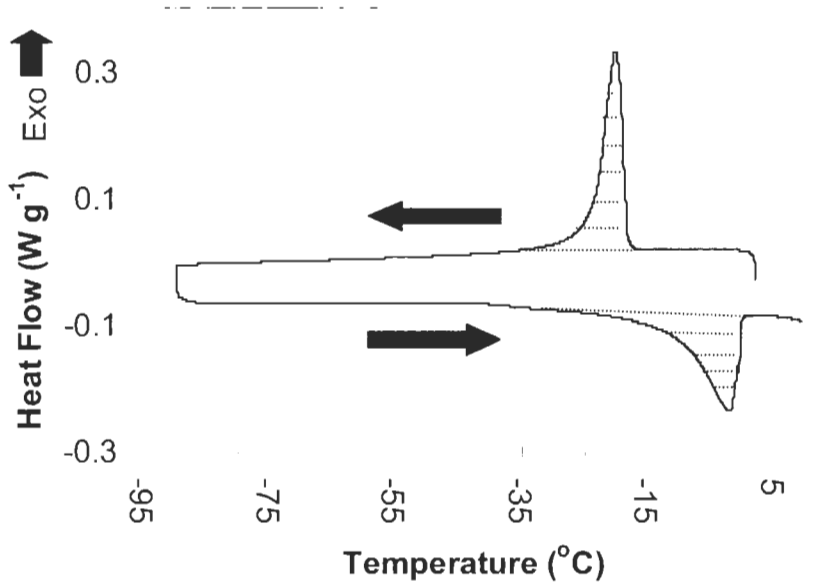

(a)

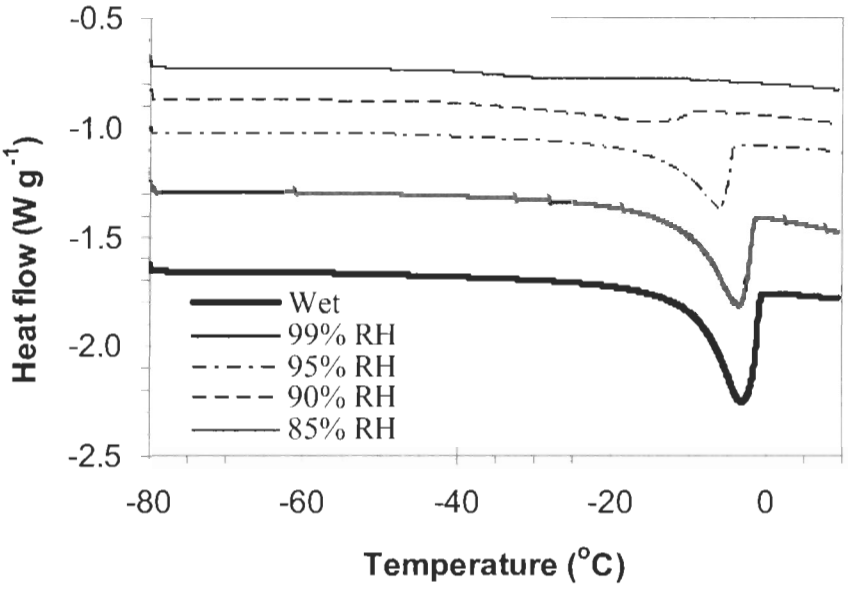

(b)

Figure 2.12: (a) DSC thermograms of water-swollen N117, (b) Endothermic DSC thermograms of ETFE-*g*-PSSA (3.27) at different humidities.

The melting temperature for fully hydrated N117 is -2.0 °C. The same transition occurs at -3.0 °C and -5.0 °C, for fully hydrated ETFE-*g*-PSSA (2.13) and (3.27) membranes, respectively. The melting transition in ETFE-*g*-PSSA shifts to lower temperatures as IEC decreases - a trend that agrees with published literature.[72,76,90] As described previously, for a given series, as the IEC is lowered the ability of the membrane to absorb water is reduced and the local acid concentration increases. Colligative properties dictate that the fusion/melting transitions of water shift to lower temperature as acid concentration increases. Exposing membranes to lower relative humidity causes them to lose water, and since IEC does not change for a given membrane this loss results in an increase in $[H^+]_{est}$, (illustrated in Figure 2.13). The estimated proton concentration varies from 1 M for fully-hydrated membranes to ~ 3 M for membranes at 85% RH, with a corresponding phase change shift from -2.2 °C to -32 °C. The freezing point depression of water in the membranes are not expected to decrease proportionally with $[H^+]_{est}$ since $[H^+]_{est}$ corresponds to the concentration of protons in the material with the volume of the polymer taken into account (and not simply to the acid concentration within the ionic pores).

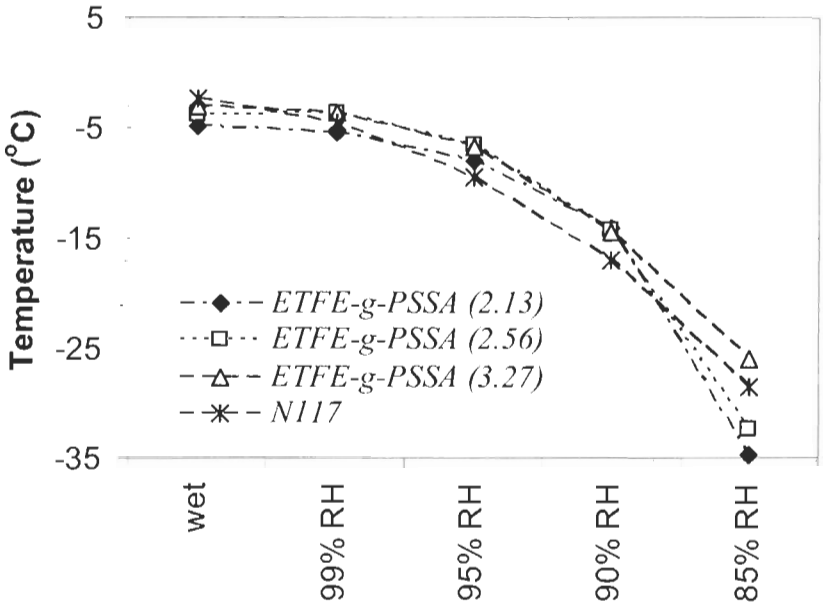

(a)

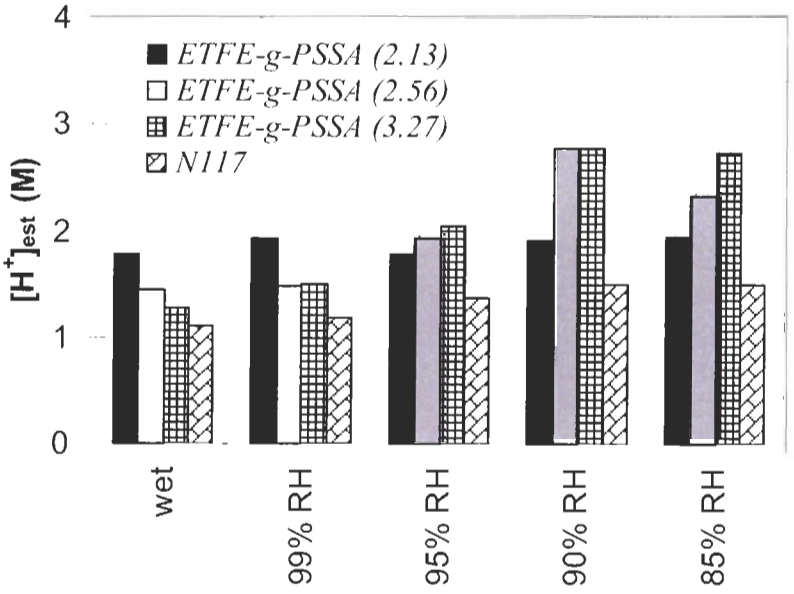

(b)

Figure 2.13: (a) Melting temperature of water in frozen N117 and ETFE-*g*-PSSA membranes as a function of membrane humidity. (b) Corresponding membrane acid concentration before freezing.

The number of water molecules per SO_3^- that freeze, $\lambda_{freezable}$, are estimated from the integrated areas under the transitions corresponding to fusion. Although a range of enthalpies is expected, in part supported by the shift of freezing to lower temperatures, there are also reasons to believe that the heat of fusion of freezable water within the hydrophilic pore may be similar to the enthalpy of fusion of bulk water. Freezable water exists in a region of the pore that is furthest away from the electrostatic charge (i.e. pore center). Studies by Pintauro *et al.*[67,68] and Paddison *et al.* [23,91] reveal that the dielectric constant of water at a small distance away from the pore wall is similar to that of bulk water (within 10%). In Nafion®, both authors estimate that 50% of the total volume of a fully hydrated pore corresponds to liquid water – a value that is similar to the fraction of freezable water in the membrane. From this work, it can be inferred that the heat of fusion of the water that freezes in the membrane is similar to bulk water.

Values of $\lambda_{freezable}$ are estimated to be ~16, 12, and 9 for fully hydrated ETFE-*g*-PSSA (3.27), (2.50), and (2.13), and 9 for fully hydrated Nafion®. Reducing the relative humidity (and therefore the membrane's water content) significantly reduces $\lambda_{freezable}$. For instance, the averaged $\lambda_{freezable}$ for ETFE-*g*-PSSA (3.27) falls from 12 at 99% RH to 0.4 at 85% RH; and for N117, from 6 at 99% RH to 0.6 at 85% RH.

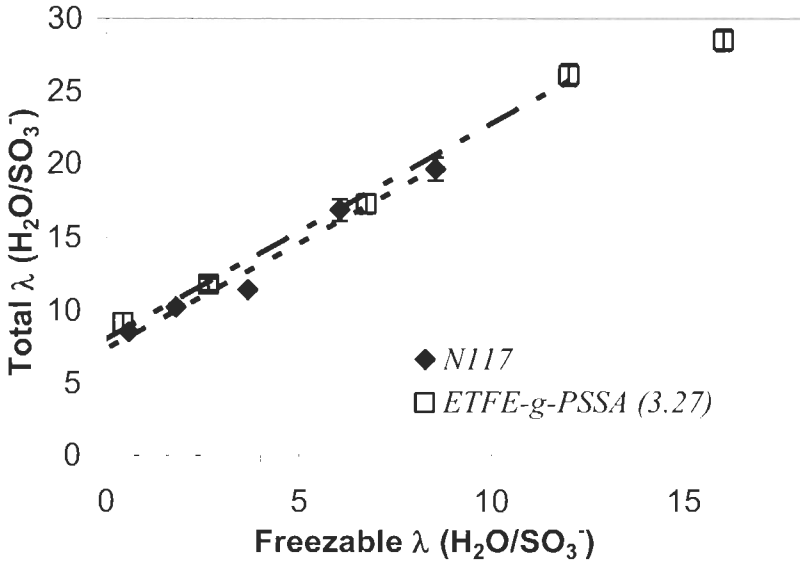

Figure 2.14: Plot of total λ (TGA) *versus* $\lambda_{freezable}$ (DSC) for N117 and ETFE-*g*-PSSA (3.27). The intercept provides $\lambda_{non\text{-}freezable}$.

The total amount of water in the membrane, λ, in Figure 2.10 (a), is the sum of $\lambda_{freezable}$ and $\lambda_{non\text{-}freezable}$. The values for $\lambda_{non\text{-}freezable}$ were estimated from the intercept of a plot of total water *versus* freezable water, the latter being varied by the humidity and measured by DSC analysis. An example is shown in Figure 2.14 for N117 and ETFE-*g*-PSSA (3.27). The averaged $\lambda_{non\text{-}freezable}$ calculated using this technique are estimated to be 7, 8, 8 and 8 for ETFE (2.12), (2.56), (3.27), and N117, respectively. Gupta[72] reported similar values for radiation-grafted poly(tetrafluoroethylene)-*g*-PSSA membranes; however, the values are slightly lower than those reported by Sundholm *et al.*, who calculated $\lambda_{non\text{-}freezable}$ to be ~ 10 H_2O/SO_3^- for ETFE-*g*-PSSA membranes by subtracting $\lambda_{freezable}$ from total λ.[73] The discrepancy may be due to subtle differences in the membranes and the techniques used.

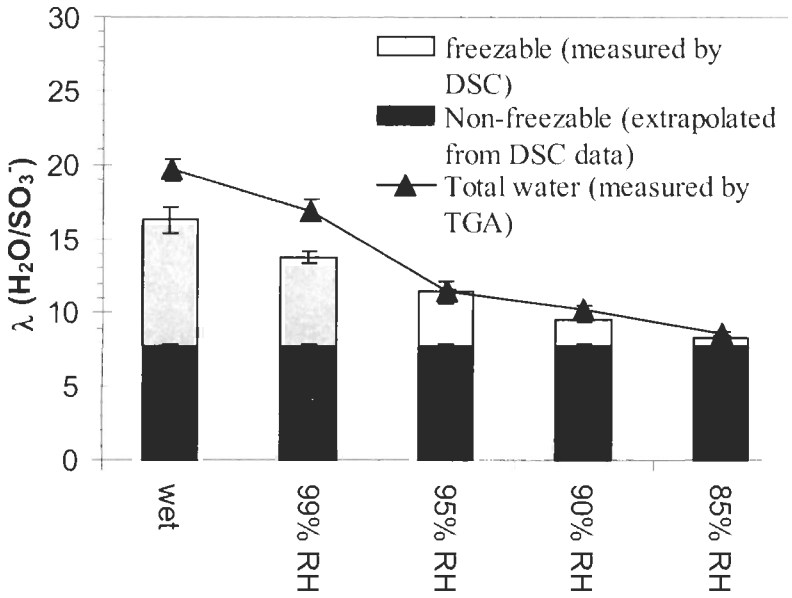

Figure 2.15: Histograms comparing total λ (TGA), $\lambda_{freezable}$ (DSC), and $\lambda_{non\text{-}freezable}$ for N117. Non-freezable λ was estimated by using a similar method described by Gupta.[72]

A more significant concern is the possibility of systematic variation in the structure of the membrane induced by controlling $\lambda_{freezable}$ through RH (Figure 2.3). The deviance of slopes in Figure 2.14 from unity for a membrane of a given IEC may infer changes in pore shapes with humidity (gradients of slope, s = 1.3 - 1.7), and explain the inconsistencies between the sum of $\lambda_{non\text{-}freezable}$ (estimated by extrapolation) plus $\lambda_{freezable}$ (measured by DSC), and the total λ (measured by TGA) as shown in Figure 2.15 for N117. The same discrepancy is also observed for ETFE-*g*-PSSA membranes for which the sum of freezable plus non-freezable λ. is ~15% of the total λ measured by TGA. Combined, these observations indicate that non-freezable λ as determined by the Gupta method may be underestimated.

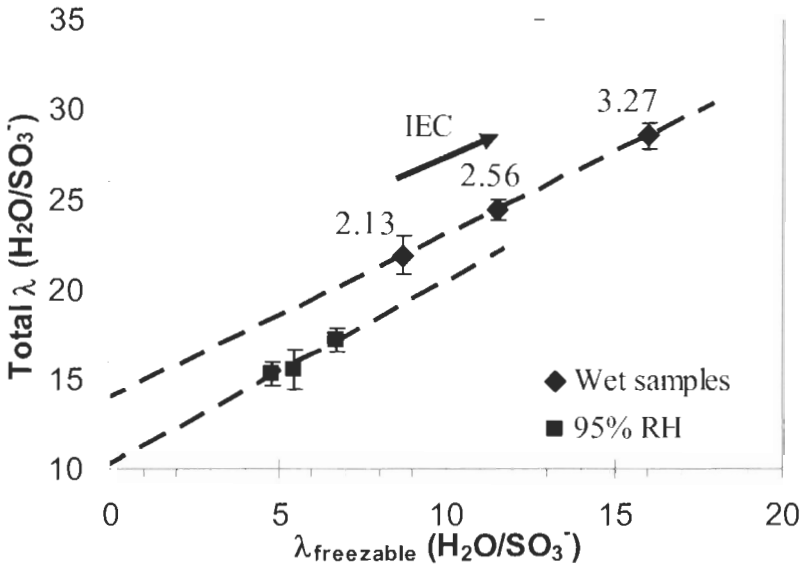

Figure 2.16: Plot of total λ (TGA) *versus* $\lambda_{freezable}$ (DSC) for ETFE-*g*-PSSA membranes equilibrated with liquid water and at 95% RH. The intercept provides $\lambda_{non\text{-}freezable}$. Total λ was controlled by changing the IEC of the sample. The IEC of the samples are provided in parathesis.

The conjecture that non-freezable λ depends on the relative humidity is verified from linear plots of total λ (TGA) *versus* freezable λ (DSC) for which the latter is controlled by the IEC of the membrane. Examples of such plots for ETFE-*g*-PSSA membranes in their fully hydrated state and at 95% RH are illustrated in Figure 2.16. Their slopes are 0.9 ± 0.2 and 1.0 ± 0.5, respectively. Experimental uncertainty increases when the humidity of the samples decreases, but this method is expected to yield a more reliable $\lambda_{non\text{-}freezable}$. Although some variation in morphology is expected from samples with different IECs, the variation to morphology by changing IEC should be smaller than changing humidity alone because the polymers are well percolated. Values of non-freezable λ extrapolated using this technique are 14, 10, 10 8.5, 8.5 H_2O/SO_3^- for ETFE-*g*-PSSA in wet, 99%, 95%, 90% and 85% RH, respectively. The value for non-freezable

water for hydrated samples measured in this fashion is closer to that measured by Sundholm. The same analysis could not be extrapolated for N117 because of a lack of available membranes with different IEC; however, non-freezable λ for N117 is expected to lie within 7.7 – 11 (estimated by subtracting freezable λ from the total λ measured) for 85% RH and wet samples, respectively.

Shown in Figure 2.17 in the form of a histogram are the $\lambda_{non\text{-}freezable}$ (determined by extrapolation using the modified Gupta's method), $\lambda_{freezable}$ (determined by DSC), and the total λ values (determined by TGA) for ETFE-*g*-PSSA (3.27) and ETFE-*g*-PSSA (2.13). Good agreement is found between the sum of $\lambda_{non\text{-}freezable}$ and $\lambda_{freezable}$, and total λ for all ETFE-*g*-PSSA samples. All λs (total, freezable and non-freezable) decrease with relative humidity. However, the majority of water lost is freezable water, and virtually no freezable water is detected in the freezing transition at 85% RH.

The data obtained from this study is consistent with work published by others[72,73] who used ΔH_{fusion} for bulk water in the integration of thermograms, but differs from that of Kim[52] *et al.* who used proton spin relaxation and T_g correlations. This dissimilarity may be due to the difference in temperatures between the experiments.

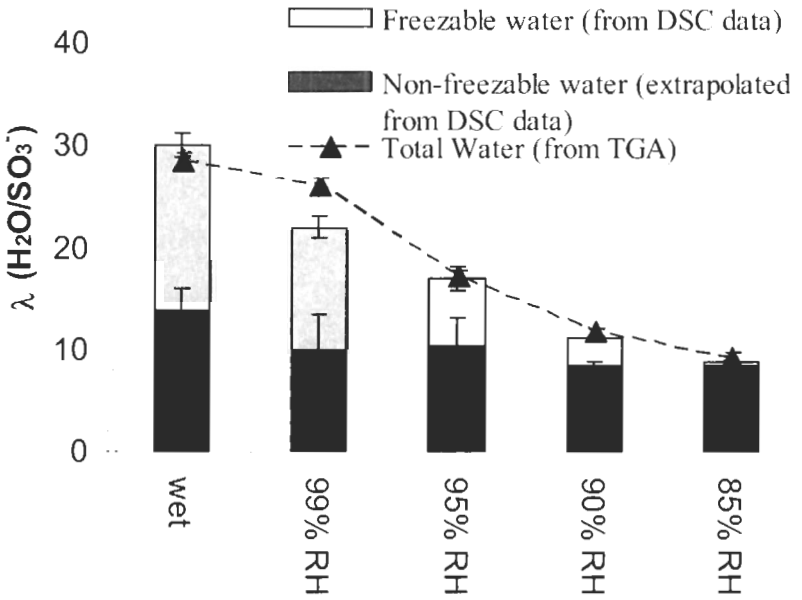

(a)

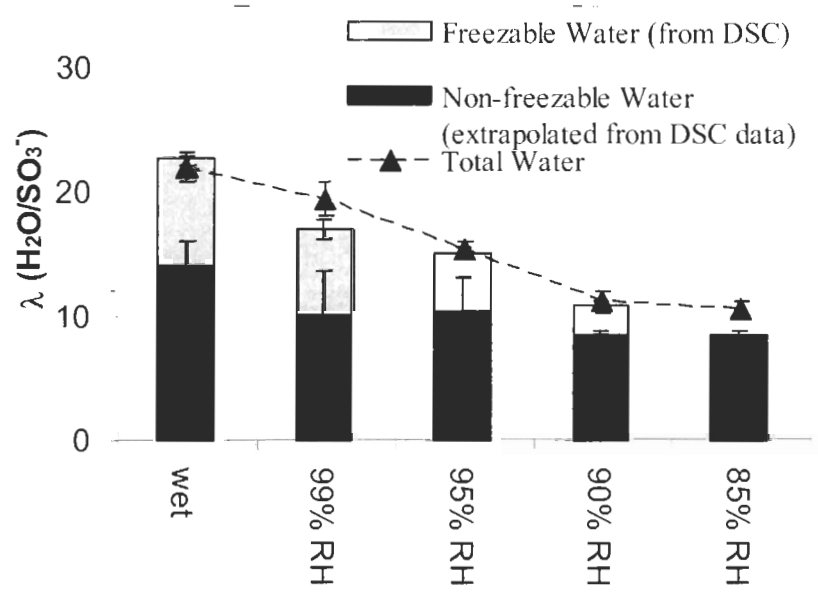

(b)

Figure 2.17: Histograms comparing total λ (TGA), $\lambda_{freezable}$ (DSC), and $\lambda_{non\text{-}freezable}$ for (a) ETFE-*g*-PSSA (3.27) and (b) ETFE-*g*-PSSA (2.13). Non-freezable λ was estimated using a modified Gupta method[72], wherein, the amount of $\lambda_{freezable}$ was controlled by IEC.

2.3.5 State of Water for Membranes Equilibrated below 85% RH

Gravimetric analysis shows that λ decreases from 14 to 9 and from 11 to 7 H_2O/SO_3^-, for N117 and ETFE-*g*-PSSA (2.13), respectively, at RH between 85% and 45%. No freezing thermal transition was detected in the exothermic direction for the samples; however, a very small melting phase was noticed in the endothermic direction of the samples at 85% RH, but the signal disappears with further reduction of humidity as illustrated in Figure 2.18. This discrepancy could be attributed to poor distinction between signal and baseline due to signal broadening in the exothermic direction. As the peak is expected to contribute negligibly to the overall content of freezable water, the state of water for N117 and ETFE-*g*-PSSA is virtually non-freezable below 85% RH.

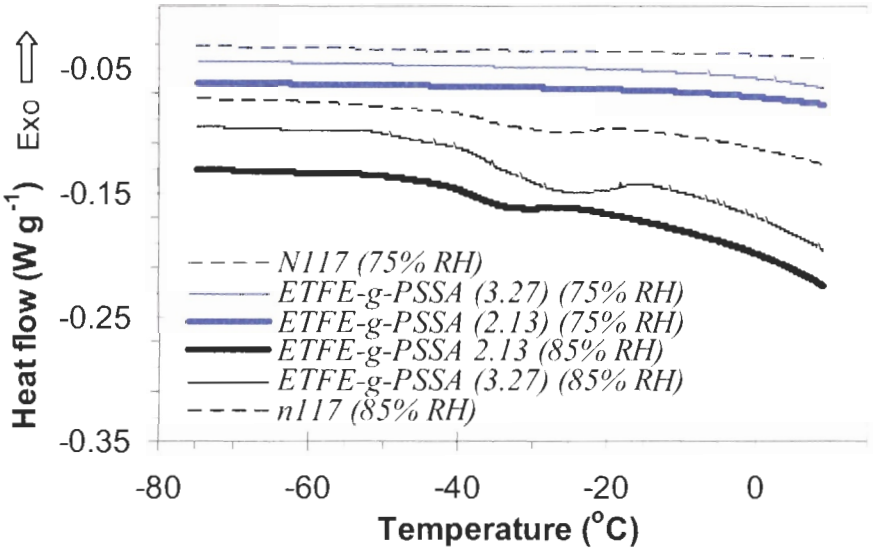

Figure 2.18: DSC traces of N117, ETFE-g-PSSA (2.13) and (3.27) at 75 % and 85 % RH.

2.3.6 Proton Conduction Through Non-Freezable Water

Proton conductivities of 0.045 – 0.009, 0.053 – 0.007, and 0.063 – 0.008 S cm^{-1} measured for N117, ETFE-*g*-PSSA (2.13) and (3.27), respectively, in the humidity range between 85% and 45% RH are still quite reasonable (Figure 2.19). Even though N117 possesses a slightly higher water content than ETFE-*g*-PSSA, proton conductivity of ETFE-g-PSSA is still slightly higher. This difference diminishes when RH drops to 55%.

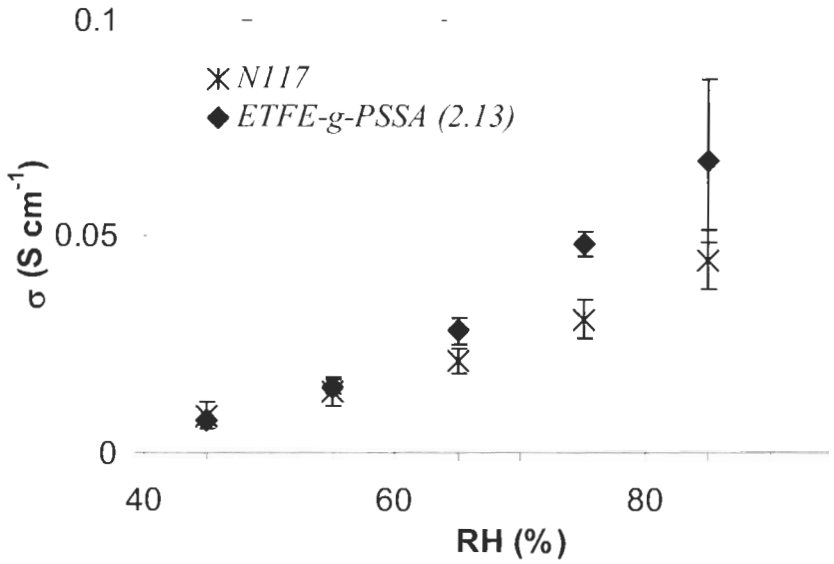

Figure 2.19: Proton Conductivity of N117 and ETFE-*g*-PSSA (2.13) membranes equilibrated between 45% and 85% RH and at 25 °C.

Decreasing the temperature of membranes humidified between 99% and 45% RH resulted in two conductivity trends. An example is illustrated in Figure 2.20 for N117; wherein, two sharp breaks were seen in the conductivity plots when the membrane were equilibrated between 99% and 85% RH, but none when the membranes were equilibrated in the humidity range when only non-freezable water was present (i.e., < 85% RH). As explained earlier, the first sharp break in the former scenario corresponded to the onset of water freezing. The process continued until water molecules in the ionic domains could

no longer organize into a crystalline structure i.e., ice (~ -20 °C for N117). Proton conductivity values continued to drop upon further decrease of temperature from 0.009 S cm^{-1} at -20 °C to ~ 0.002 S cm^{-1} at -37.5 °C. Preliminary results of ETFE-*g*-PSSA also exhibit similar behaviours.

The water content of the sample is believed to remain quite stable during the experiment because: (1) re-equilibrating the membrane at 25 °C after the experiment produced a value that was in agreement with the conductivity value measured at the beginning of the experiment, and (2) the proton conductivity of the sample measured at -37.5 °C at the end of the experimental compared well to proton conductivity of the sample measured at -37.5 °C after it has equilibrated at 25 °C.

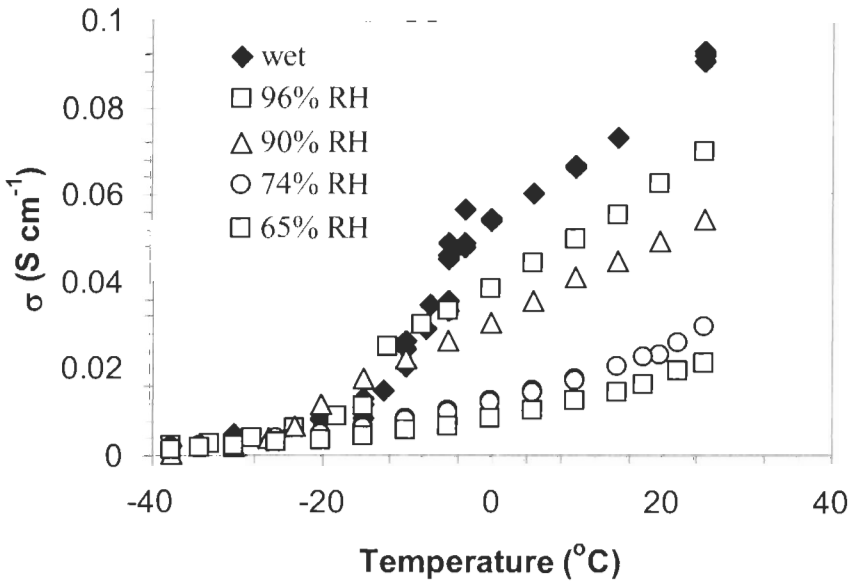

Figure 2.20: Proton conductivity at sub-zero temperature for N117 with reduced humidity. The samples were pre-equilibrated at 25 °C in a jar before the temperature of the sample was lowered. The humidity of the membrane was determined by comparing the conductivity measured at 25 °C with Figure 2.19.

The Arrhenius plots between 25 °C to -37.5 °C for N117 are illustrated in Figure 2.21. Two activation energies are seen for N117 with RH greater than 85% RH: one for proton transport before water in the membrane freezes, and one after free water in the membrane freezes. The activation energy for the former is between 0.15 – 0.17 eV; the latter is approximately ~ 0.4 eV. Both values are comparable to published data,[77,78,83] and are similar to those found for proton conduction in bulk water, and polycrystalline ice, respectively.[84] It is unlikely that the activation energy of 0.4 eV is attributed to ice because proton conductivity in ice is much lower (see section 2.3.1).

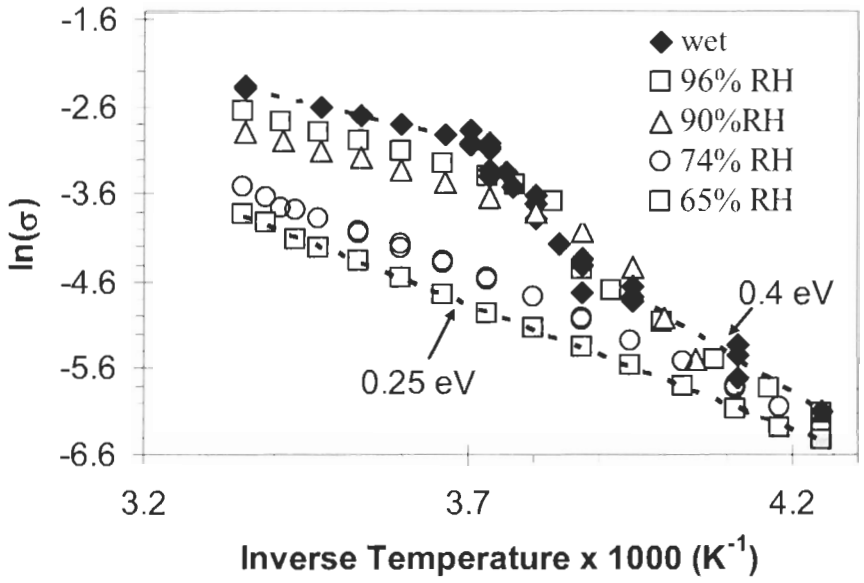

Figure 2.21: Arrhenius plots of N117 between 25 and -37.5 °C at varying degree of hydration.

Despite that two energy barriers were observed for membranes with humidity > 85%, only one energy barrier of 0.25 – 0.26 eV was detected for proton transport in N117 with RH between 45% - 85%. The inconsistency in activation energies (0.4 *versus* 0.25 eV) between the two conductivity trends at the low temperature regime could stem from

various reasons. One of them is the reduced spatial separation between SO_3^- groups, as schematically illustrated in Figure 2.3, at lower RH, which can potentially lower the energy barrier of proton conduction. A more probably cause is the increased restrictive nature of the hydrophilic domains possibly due to the presence of ice as shown in Figure 2.22 . The broad features of the exothermic phase change of hydrated N117 in Figure 2.12 (a) strongly support the latter theory.

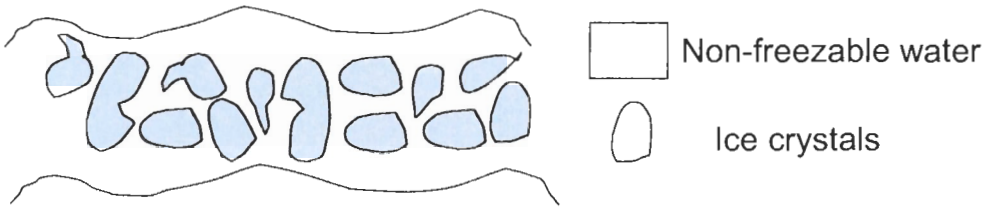

Figure 2.22: Schematic diagram of ice in frozen N117 with free water.

2.4 Discussion

Factors that determine ionic conductivity are concentration and mobility of the charge carriers in the membrane. As illustrated in Figure 2.10 (b), proton conductivity increases with a systematic increase in IEC for water-swollen membranes. This increase is due to an increase in the mobility of the protons as a result of increased hydration and an increase in *free* water in the pores.

Proton mobility, μ_{est}, was estimated using equation 2.8[92]

$$\mu_{est} = \frac{\sigma}{F\ [H^+]_{est}\,(\text{in M})} \times 1000 \qquad (2.8)$$

F is Faraday's constant and σ is the proton conductivity of the membrane. The calculated proton mobilities range from 0.85×10^{-3} to 1.59×10^{-3} $cm^2\ s^{-1}\ V^{-1}$ for N117 and ETFE-*g*-PSSA membranes in their fully hydrated states (Table 2.1). Saito *et al.* estimated the

proton mobility of N117 to be ~ 2 times higher than the one measured in this work.[93] The proton mobility of the graft polymers correlates well with the change in acid concentration: it is highest for samples with the largest IEC and water uptake (or λ value). Increasing λ in the membranes from 8 to 20 (by varying RH) increases proton mobility in ETFE-*g*-PSSA by a factor of 5; whereas proton mobility for N117 increases only by a factor of 2.

The large proton mobility in bulk water (~9 times larger than Li^+ and ~5 times the mobility of K^+ in solution) is due to additional contributions of the Grotthuss mechanism to vehicular mechanism. Proton mobility for the membranes were extrapolated to infinite dilution (i.e,. $X_v = 1$) in order to compare directly with that of bulk aqueous solution (3.6×10^{-3} cm^2 s^{-1} V^{-1}). The highest value attained for ETFE-*g*-PSSA was ~ 46% of mobility in bulk water. The difference between proton mobility in membranes and bulk water illustrates the effect of a restricted and tortuous ionic network within the polymer system.

Proton mobilities in ETFE-*g*-PSSA membranes are similar to that in N117 membranes of similar λ values (Figure 2.23 (a)). Proton mobility is further correlated to water volume fraction, X_v, as shown in Figure 2.23 (b) in order to understand how membrane structure relates to proton transport. The data indicates that ETFE-*g*-PSSA contains a higher volume fraction of water compared to Nafion®, which suggests that the higher proton mobility in ETFE-*g*-PSSA is ascribed to a more fully developed percolated network of ions and free water. However, when comparing proton mobilities where the two polymer series overlap in the volume fraction of water (e.g., X_v= 0.35-0.40), N117 possesses a higher mobility – by up to a factor of 2 – from which it can be inferred that, in this regime, the connectivity of hydrophilic regions is more extensive in Nafion®

because by virtue of its higher IEC, ETFE-*g*-PSSA needs a larger X_v before reaching the same λ as N117. That is, the percolation threshold for ETFE-*g*-PSSA is at a higher X_v value. The higher proton mobility in the high IEC membranes ETFE-*g*-PSSA membranes may simply be the result of their possessing a higher water content.

The proton mobility trend calculated using this method compares well with those calculated by others. Kreuer, for example, elegantly illustrated how the diffusion coefficient (calculated from proton conductivity data using the Einstein relation) increases with increasing humidity and volume fraction.[94] Diffusion coefficients of protons, calculated from proton mobility using the Einstein relation[92] (equation 2.9) are illustrated in Figure 2.23 (c). Diffusion coefficients reported in the literature [94] for X_v = 0.2 and 0.4 are ~0.50 x 10^{-5} cm^2 s^{-1} and 1.03 x 10^{-5} cm^2 s^{-1}, respectively for Nafion® at 27 °C; the values calculated in this work are 0.87 x 10^{-5} cm^2 s^{-1} and 2.2 x 10^{-5} cm^2 s^{-1} at 25 °C. The highest diffusion coefficient for ETFE-*g*-PSSA is observed at X_v = 0.7 (4.07 x 10^{-5} cm^2 s^{-1} for ETFE-*g*-PSSA (3.27)) at 25 °C. This value compares well with reported diffusion coefficient of protons (calculated from the Einstein relation) in sulphonated poly(phenoxyphosphazene) (4 x 10^{-5} cm^2 s^{-1}), DOW, Nafion® poly(arylene ether ketone)s (S-PEK) and SPEK blends with X_v at 0.7.[94]

$$D_\sigma = \frac{RT\mu_{est}}{|z|F} \qquad (2.9)$$

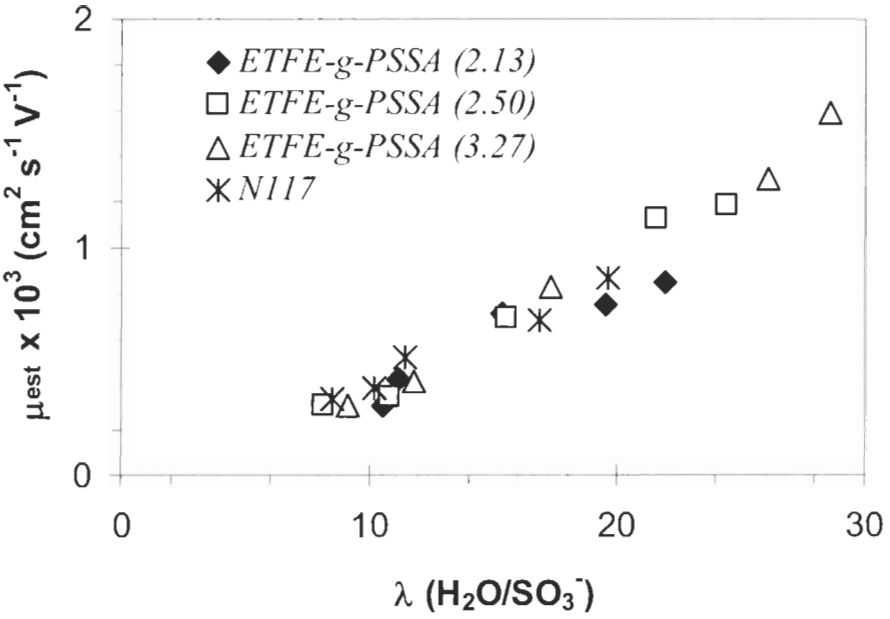
◆ ETFE-g-PSSA (2.13)
□ ETFE-g-PSSA (2.50)
△ ETFE-g-PSSA (3.27)
✳ N117
μest x 10^3 (cm^2 s^-1 V^-1)
λ (H2O/SO3-)
0
1
2
0
10
20
30

(a)

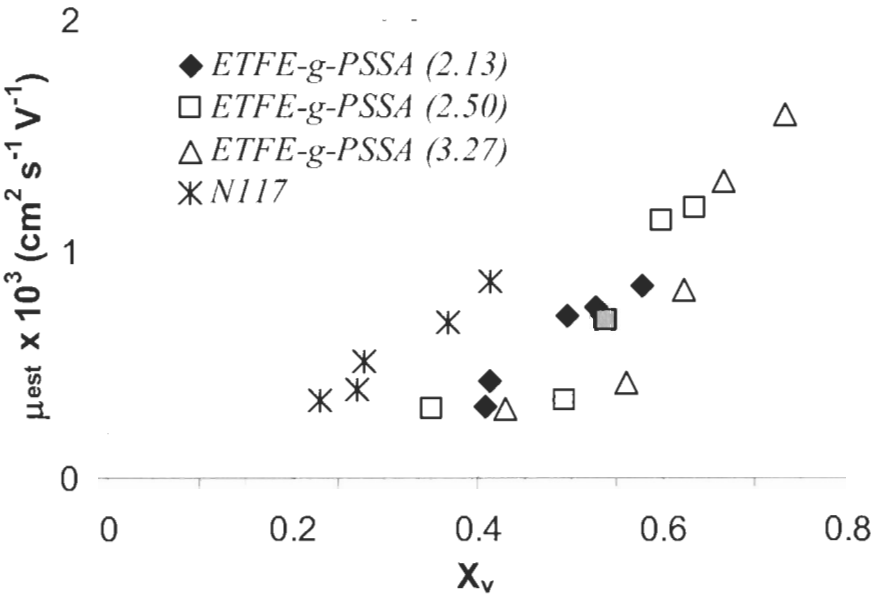
◆ ETFE-g-PSSA (2.13)
□ ETFE-g-PSSA (2.50)
△ ETFE-g-PSSA (3.27)
✳ N117
μest x 10^3 (cm^2 s^-1 V^-1)
Xv
0
1
2
0
0.2
0.4
0.6
0.8

(b)

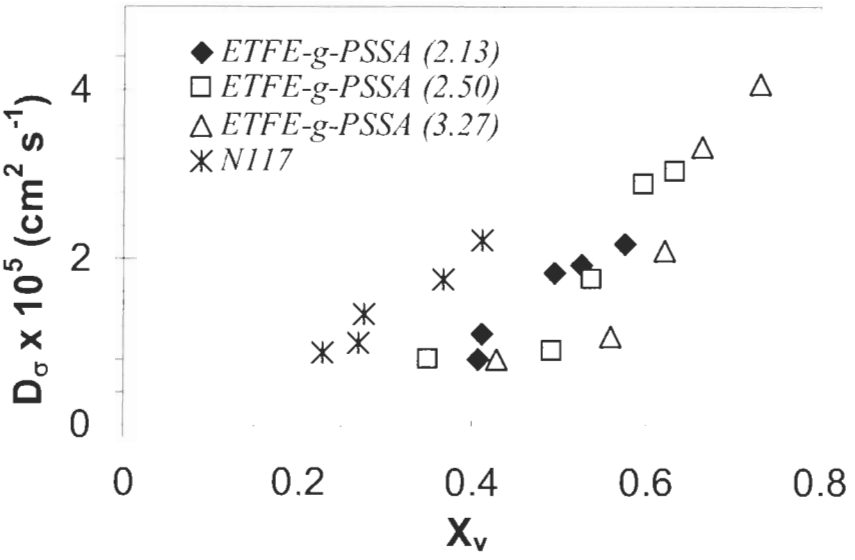

(c)

Figure 2.23: Estimated proton mobility, μ_{est}, as a function (a) of total λ and (b) of the volume fraction of water, X_v. (c) Diffusion coefficients of protons, D_σ, as a function of X_v.

2.5 Conclusions

Low temperature conductivity of two classes of proton conducting membranes at various states of humidity was studied. Three conductivity regions were observed for membranes that contain free water (i.e., > 85% RH) in the Arrhenius plots. The regions correspond to: (1) above the freezing point of water, (2) at the freezing point of water, and (3) below the freezing point of water, with transport occurring through domains of non-freezable water that are in close proximity to the surface of an ion-lined pore. However, only one conductivity region was observed for membranes containing only non-freezable water (i.e., < 85% RH). Non-freezable λ, extrapolated from the intercept of plots of total λ *versus* freezable λ, and from gravimetric analysis reveal that ~ 5 – 14 H_2O per ionic group do not freeze. Proton conductivity above 0 ^oC is highest for

membranes with larger *freezable* water contents since the presence of bulk-like water increases the mobility of protons in fully-hydrated membranes.

The ability of non-freezable water (or ion-bound water) to facilitate the transport of protons suggests that significant proton conductivity may be obtained from membranes with low water content if the membranes are optimized to yield a continuous proton conductive pathway. In PEMFC applications that require sub-zero temperature start up, this work has demonstrated that "frozen" membranes are still able to transport protons. As freezable water need not be present in order to obtain reasonable conductivity, this also has implications in the design of membranes that are required to operate with reduced RH (usually at high temperate, e.g., above 100 ^{o}C), where freezable water will not be present.

CHAPTER 3:

INFLUENCE OF WATER AND MEMBRANE STRUCTURE ON THE SELECTIVITY OF METHANOL IN POLY(STYRENE SULFONIC) ACID-CONTAINING GRAFT COPOLYMERS

Sections of this chapter have been reproduced in part with permission from:

Journal of Polymer Science: Part B: Polymer Physics, **2006**, *44*, 2240 - 2252

3.1 Introduction

The use of methanol as a "hydrogen carrier" in fuel cell has generated interests, particularly in specialized applications, such as laptops for field-use and electric scooters, where conventional batteries are not suitable because of their short operation time (i.e., 4 hours on a single battery charge). While the indirect methanol fuel cell (in which methanol is first reformed to hydrogen) still remains under development, the simple design and refuelling option of direct methanol fuel cell (DMFC) make them attractive for many portable devices. Despite the many benefits of DMFC, development and commercialization of DMFC technology face significant challenges. One of these is excessive crossover of methanol through the proton exchange membrane that lowers the overall fuel cell power density and efficiency.[6]

Methanol crossover is a prevalent problem for existing perfluorinated membranes, like Nafion®. Additives such as polypyrrole[95] and inorganic particulates[96,97] (e.g., SiO_2, TiO_2 and zeolites) have been incorporated in order to reduce their permeability to methanol. Alternative polymer membranes[17,98] such as polyimides[99,100] polysulfones[49] and poly(ether ketone)s[101] were also found to exhibit lower methanol permeabilities compared to Nafion®. Studies of polyimides by Woo *et al.*[102] and sulfonated poly(ether ketone)s by Kreuer *et al.*[101] showed that domains of ionic clusters in these systems were considerably smaller than in Nafion® and provide better methanol rejection. Kreuer also noted that the narrowing of ionic channels in poly(ether ketone)s[101] was related to a less pronounced phase separation between hydrophobic-hydrophilic domains and a more tortuous hydrophilic path for methanol transport.

Common approaches aimed to increase proton conductivity, such as by increasing the IEC or water content, also increase the permeability of methanol through the membrane. The absorption of water by the membrane swells and coalesces the ionic clusters within the membrane. This coalescence eventually leads to a continuous hydrophilic ionic network suitable for proton conduction. In an operating DMFC, methanol/water mixture is continuously supplied to the anode and water is eliminated from the cathode. As water and methanol are miscible, hydrophilic channels that facilitate proton and water transport also act as conduits for the permeation of methanol.

Decreasing the amount of "free water" within the proton conducting channels is an approach to reduce the amount of water in the PEM.[52] Free water is water that is not strongly bound to the membrane through water-ion or water-polymer interactions, and which exhibits similar characteristics to bulk water. The lower methanol permeability of poly(ether ketone)s compared to Nafion® was attributed to the lower water content of the membrane, decreased dimensions of ionic channels, and a higher number of dead-ended channels.[101] However, it is not clear how much "free water" was necessary to maintain adequate proton conductivity while keeping methanol permeability to a minimum since common approaches aimed to reduce methanol crossover also decreases proton conductivity. Furthermore, it is not obvious how the nature and microstructure of polymers that constitute a polymer electrolyte membrane influence the sorption of water, which in turn influences methanol permeability and methanol crossover.

In this chapter, control of sorbed water by variation of chemical structure and its effects on methanol transport were investigated for two classes of graft copolymer membranes: polyacrylonitrile grafted with macromolecules of poly(styrene sulfonic)

acid (PAN-*g*-*mac*PSSA) and poly(vinylidene difluoride) grafted with poly(styrenesulfonic) acid (PVDF-*g*-PSSA). Chemical structures of these polymers are shown in Figure 3.1. PAN-*g*-*mac*PSSA polymers were prepared with controlled graft lengths while PVDF-*g*-PSSA polymers were prepared with different graft densities. The data was compared to Nafion® 117 (N117).

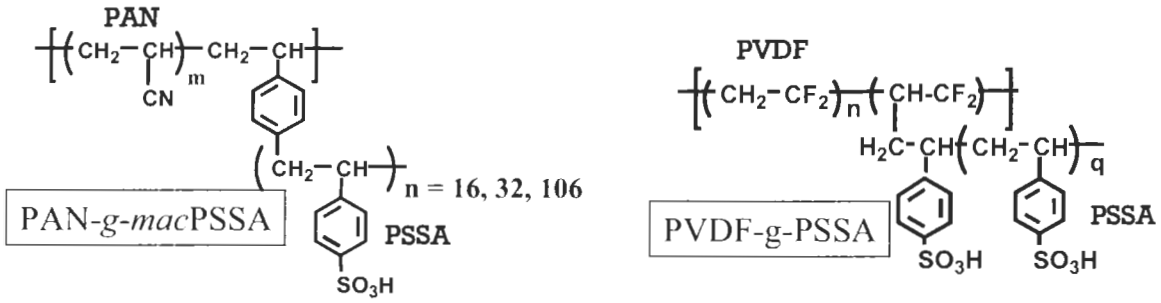

Figure 3.1: Chemical structures for PAN-*g*-*mac*PSSA and PVDF-*g*-PSSA membranes.

3.2 Experimental

3.2.1 Synthesis of Poly(styrenesulfonic) Acid-Containing Graft Copolymers

3.2.1.1 PAN-*g*-*mac*PSSA

Dr. Jianfu Ding in our laboratory provided the PAN-*g*-*mac*PSSA membranes; the synthesis of this material is described in detail elsewhere:[103] Styrenesulfonic sodium (SSNa) was polymerized by emulsion polymerization with 2,2,6,6-tetramethyl-1-piperidinyloxy (TEMPO) and $Na_2S_2O_5/K_2S_2O_8$ in a mixture of ethylene glycol/water to form poly(styrenesulfonic) sodium (PSSNa). Divinylbenzene was added at the completion of the reaction to provide a vinylic terminus for subsequent polymerization. The degree of polymerization of the macromonomer was controlled by varying the ratio of monomer to initiator. Degrees of polymerization for PSSNa macromonomer were 16,

32 and 106, with polydispersities of ~1.2. Vinylic terminated macromonomers were copolymerized with acrylonitrile to yield the graft polymer shown in Figure 3.1. A particular series in the graft copolymer is distinguished by the length of the graft chain: Series (S) was based on short graft lengths with 16 SSNa repeat units; Series (M) was based on medium graft lengths with 32 repeating SSNa units; Series (L) was based on long graft series with 106 SSNa repeat units. By varying the relative ratio of acrylonitrile to macromonomer, polymers with different ionic contents and graft densities were obtained. For a given ionic content, Series (S) contained a higher number of ionic side chains per unit length of poly(acrylonitrile) backbone than Series (M); which in turn contained more side chains per unit length of the main chain than Series (L) as illustrated in Figure 3.2 (a).

Within a series, the number of side chains per unit length of poly(acrylonitrile) was controlled by the feed ratio. The change in polymer microstructure upon increasing ionic content within a series of PAN-*g*-*mac*PSSA copolymers is illustrated in Figure 3.2 (b). A high ionic content indicated a smaller average distance of separation between graft chains and therefore a higher graft density. In contrast, a low ionic content indicated a larger graft chain separation and, therefore, a lower graft density. The different chain lengths and graft densities allowed the microstructure to be studied in a systematic manner.

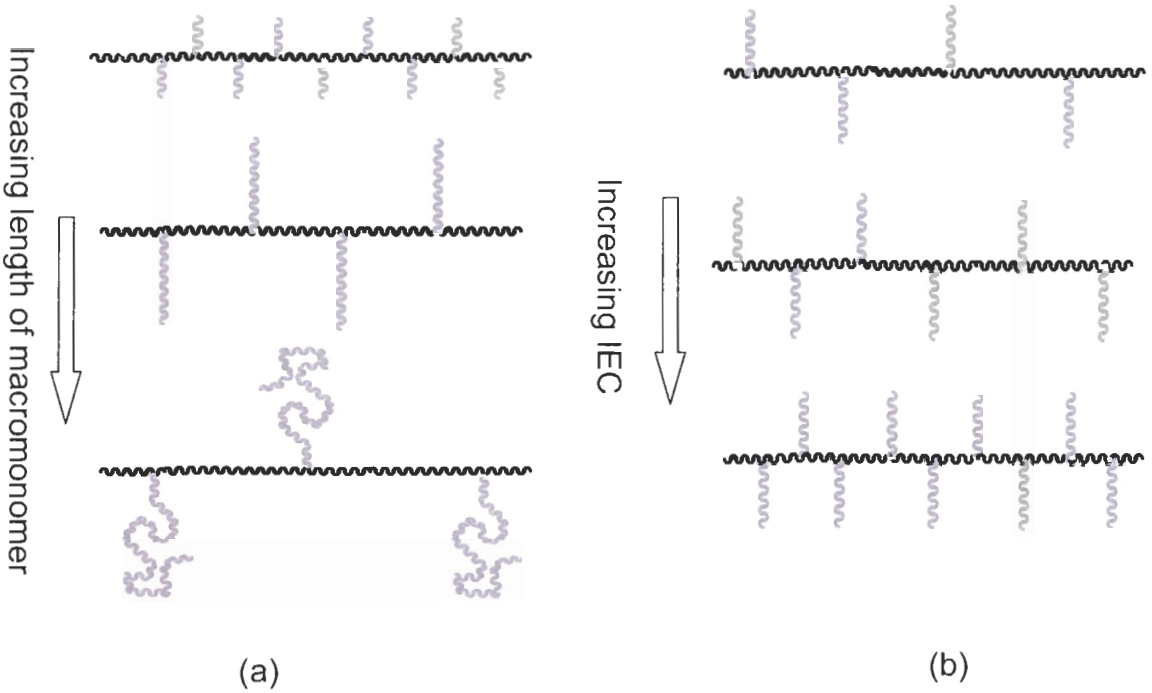

Figure 3.2: Schematic drawing illustrating (a) the effect of increasing the length of the macromonomer grafts for a given IEC and (b) for a given series with increasing IEC. The side chains are ionic poly(styrenesulfonic) acids.

3.2.2 PVDF-*g*-PSSA

Radiation-grafted membranes were provided by Lovell and co-workers (Cranfield University, UK).[81] The preparation of PVDF-*g*-PSSA membranes was similar to the preparation of poly(ethylenetetrafluoroethylene)-*graft*-poly(styrenesulfonic) acid membranes described elsewhere.[81,104] A preformed poly(vinylidene) (PVDF) film (Du Pont) was irradiated with gamma radiation and then immersed in a solution of styrene to initiate the graft polymerization of styrene. The length and density of the graft polymers were controlled by the polymerization conditions. Units of styrene were sulfonated to provide a systematic variance of ionic content for the membrane. The sulfonation process involved immersing the dry styrene grafted polymer in 5% (V/V) chlorosulfonic

acid in dichloromethane for 2 h at ambient temperature, followed by washing to neutrality with DI water.

3.2.3 Membrane Fabrication and Acidification

Both PVDF-*g*-PSSA and commercially available N117 (from Ion Power) were acquired in membrane form. PAN-*g*-*mac*PSSA powder was dissolved with stirring in a mixture of dimethylsulfoxide (DMSO) and 2% water by heating to 150 °C. The mixture was dispersed on a glass dish and dried in an oven between 110 - 120 °C for at least 20 h. The resulting transparent film was released from the glass substrate by immersion in water. Each polymer series was identified by the degree of polymerization of the macromonomer and was provided in brackets. For instance, S = 16, M = 32 and L = 106 repeating SSNa units.

Nafion® membranes were treated by boiling in 3% hydrogen peroxide solution for 30 min, and then in water for another 30 min. They were then boiled in 0.5 M H_2SO_4 for 30 min. Poly(styrenesulfonic) sodium membranes were treated less rigorously. Membranes were first soaked in MilliQ (Millipore) water for at least 30 min. and then transferred to 2 M H_2SO_4 for 1 day. Excess acid was removed from the membranes by soaking them in Millipore water for another 1 day. The water was changed at least 3 times to ensure adequate rinsing. Membranes in their protonic form were stored in Millipore water until use.

Homopolymer PAN film was prepared by dissolving PAN powder (Aldrich) in dimethylsulfoxide/water (98/2 v/v) and heating to 100 °C. The mixture was poured in a

flat Petri dish and dried overnight in an oven at 110 °C. The resulting film was released from the glass substrate by immersion in water.

3.2.4 Membrane Characterization

3.2.4.1 Ion Exchange Capacity, Water Content, and Acid Concentration

Ion exchange capacities (IEC) were determined by titration of acid (released from membranes in their protonic form in 2 M NaCl) with sodium hydroxide. The volume fraction of water in a water-swollen membrane, X_v, was calculated by converting the mass of water to volume using the density of water (1 g mL^{-1}), and the mass of the hydrated membrane to volume using the density of the hydrated membrane.

Water contents were determined from the mass ratio of water absorbed by the membrane from dry state to mass of the water-saturated membrane. A temperature of 80 °C and vacuum of 27 mm Hg was applied for 1 day to dry the samples. Proton concentrations in the membranes were estimated using equation 2.3.

3.2.5 Low Temperature Differential Scanning Calorimetry

Freezable-water in water-saturated membranes was measured by differential scanning calorimetry (DSC). A detailed description of the method used is presented in section 2.2.5. From conservation of mass, the total fraction of water in the membrane should correspond to the sum of freezable and non-freezable water.

3.2.6 Methanol Permeability

Methanol permeabilities of PEMs were measured with a set-up that is similar to Crank's diffusion cell.[45,105] The membrane of interest was mounted in between two half-

glass compartments. MilliQ water filled the receiving reservoir while a mixture of methanol and water (between 0.5 – 4.5 M) filled the source reservoir. No concentration dependence was observed for the measured methanol permeabilities. Diffusion of methanol from the source compartment to the receiving compartment was monitored by measuring the change in methanol concentration in the receiving compartment with a refractive index dectector (Waters 2414). A Shimadzu LC-10AD liquid chromatography pump circulated the water-methanol mixture between the receiving reservoir and the refractometer as shown in Figure 3.3. The permeability of methanol was calculated by fitting the change in methanol concentration in the receiving compartment as a function of time to equation 3.1. Methanol permeability was calculated from the slope, $-D_{MeOH}H\chi$. The notations c_s and c_r are methanol concentration in the source and receiving compartments, respectively, and c_s^o and c_r^o are their respective initial concentrations, D_{MeOH} is the diffusion coefficient of methanol and H is the partition coefficient. Methanol permeability, P_{MeOH} is the product of D_{MeOH} and H.

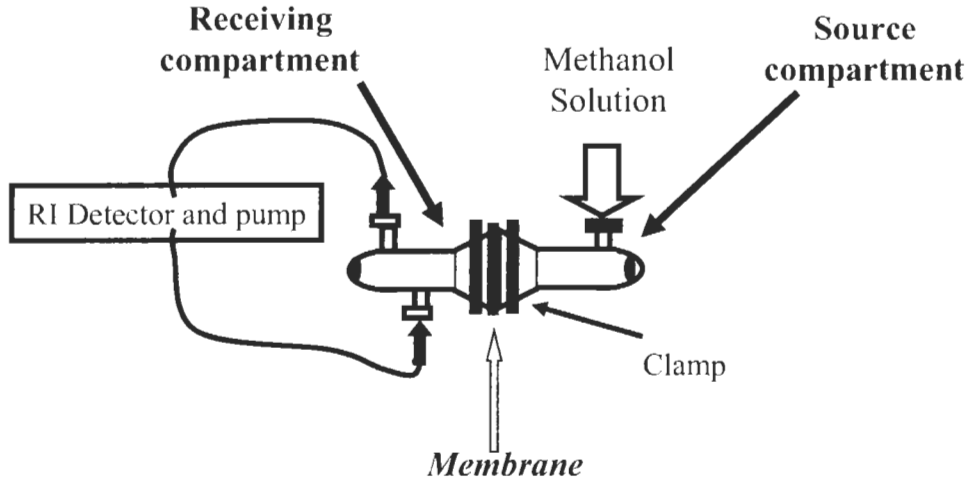

Figure 3.3: Apparatus for measuring methanol permeability.

$$\ln \frac{cs - cr}{c_s^{\,o} - c_r^{\,o}} = -\chi D_{MeOH} Ht \tag{3.1}$$

$$\chi = \frac{A}{l}\left(\frac{1}{V_s} + \frac{1}{V_r}\right) \tag{3.2}$$

3.2.7 TEM Analysis

Membranes were exchanged with Pb^{2+} by soaking them in a saturated $Pb(Ac)_2$ solution for 1 day in order to enhance the contrast between ionic and non-ionic domains. The stained membranes were rinsed with water, dried under a vacuum, imbedded in a Spur resin (Canemco) and sectioned using a Leica ultramicrotone (EM UC6) along the normal direction to yield a membrane < 100 nm thick. The slices were placed on a copper grid and viewed under a Technai G^2 transmission electron microscope (120 kV electron beam) at the Nano-imaging facility at Simon Fraser University.

3.2.8 Pulsed-Field Grandient Nuclear Magnetic Resonance (PFG-NMR)

Self-diffusion coefficients of water in hydrated membranes were determined by PFG-NMR.[106] Water-saturated samples were placed in a 10 mm NMR J-Young valve tube containing a drop of water. The tube was sealed and placed in a gradient coil probe. The ^1H echo attenuation was measured after applying the pulse sequence shown in Figure 3.4. Two field gradient pulses, **A** and **B**, were deliberately applied to distort the homogeneity of the magnetic field over the sample in a controlled manner. The first pulse labelled the position of the nuclei while the second gradient pulse detected the nuclei after a diffusion time, Δ. Nuclei that did not move over this time scale exhibited a signal.

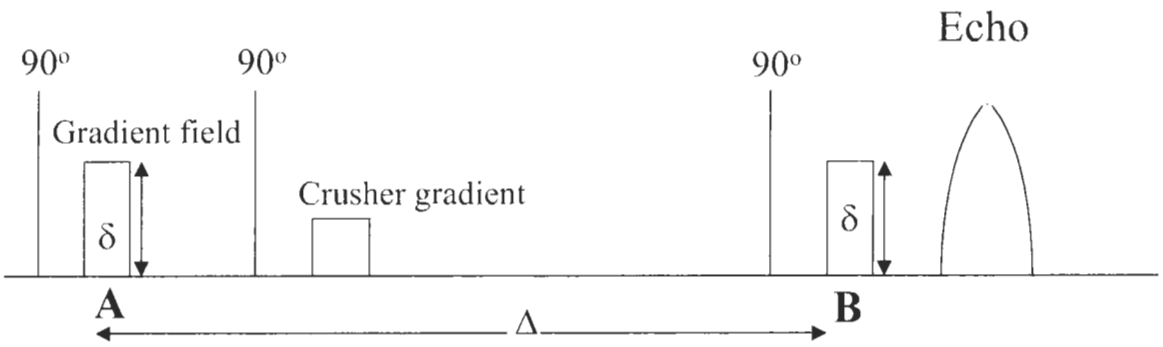

Figure 3.4: Pulse sequence applied to measure the self-diffusion coefficient of water in water-saturated membranes.

Fitting the attenuated signal to the Stejskal-Tanner equation (equation 3.3) as a function of the gradient strength yields the self-diffusion coefficient of water[107]

$$A(g) = A(0)\exp[-D_{H2O}\gamma^2 g^2 \delta^2 (\Delta - \frac{\delta}{3})] \qquad (3.3)$$

where A(g) is the measured signal, A(0) is the signal when no gradient is applied, γ is the gyromagnetic ratio (26752 for ^1H), g is the gradient strength, δ is the length of the gradient pulse, Δ is the time between gradient pulses and D_{H2O} is the self-diffusion coefficient of water.

Measurements of PAN-*g*-*mac*PSSA and PVDF-*g*-PSSA membranes were performed at Los Alamos National Laboratory (New Mexico, USA), and at Colorado School of Mines (Colorado, USA), respectively. At Los Alamos, measurements were performed on a Bruker AMX 400 MHz NMR spectrometer, with δ and Δ set between 1.5 – 2 ms, and 30 – 720 ms, respectively, and g was 34 G cm^{-1} (maximum). At Colorado School of Mines, samples were placed in a 5 mm gradient probe, and measurements were performed on a Chemagnetics CMX Infinity 400 NMR spectrometer operating at 400 MHz. δ was 1 ms, Δ was 4.2 ms, and g was 587 G cm^{-1} (maximum). Both experiments

were performed at 30 °C and were calibrated against water at 25 °C. Self-diffusion coefficients were estimated when the coefficient was independent of Δ.

Standard deviation and error propagation were applied to estimate the errors associated with the characterization techniques used.

3.3 Results and Discussion

3.3.1 Effect of IEC and Length of Side Chain on Membrane Properties

The properties of three classes of membranes studied are listed in Table 1. Proton conductivity, IEC, water content, λ_{total} and P_{MeOH} for N117, PAN-*g*-*mac*PSSA and PVDF-*g*-PSSA membranes all exhibit a strong dependence on the content of styrenesulfonic acid. As seen in Figure 3.5 and Figure 3.6 proton conductivity and methanol permeability for PAN-*g*-*mac*PSSA membranes are insensitive to the side chain length, but depend strongly on the IEC.

Table 3.1: Properties of PAN-*g*-*mac*PSSA, PVDF-*g*-PSSA, N117 Membranes

Sample / SSA[a]	IEC [b,g] (mmol g^{-1})	ℓ (mm)	σ [d,g] (S cm^{-1})	H_2O [e,g] (wt %)	λ_{total} [g] (H_2O /SO_3^-)	$[H^+]_{est}$ (M)	P_{MeOH} (cm^2 s^{-1}) x 10^7	$\lambda_{freezable}$ (H_2O /SO_3^-)	D_{H2O} x 10^6 (cm^2 s^{-1})	$X_vF_{freezable}$ [f]
PAN-*g*-*mac*PSSA (16)										
10.7	1.54	0.058	0.084	47	35	0.93	7.9	14	$\leq$ 8.7	0.19
7.9	1.15	0.021	0.031	35	29	1.52	1.5	1	8.8	0.007
4.3	0.71	0.021	0.003	19	20	0.86	0.13	0	-	0
2.6	0.45	0.031	<0.003	10	16	0.61	0.018	0	-	0
PAN-*g*-*mac*PSSA (32)										
8.5	1.39	0.036	0.055	42	32	0.78	8.2	7	-	0.073
7.6	1.17	0.041	0.037	36	29	0.94	2.2	5	-	0.071
6.1	0.98	0.025	0.013	28	25	0.59	0.23	1	-	0.014
4.9	0.81	0.024	0.006	22	20	1.52	0.032	1	-	0
PAN-*g*-*mac*PSSA (106)										
13.6	1.85	0.022	0.098	51	36	0.95	12	19	-	0.27
10.4	1.51	0.022	0.049	43	31	0.75	7.9	11	-	0.17
7.6	1.18	0.016	0.026	32	24	0.83	2.1	7	-	0.087
7	1.13	0.016	0.013	24	22	1.18	0.48	1	-	0.012
3.9	0.67	0.027	0.003	15	16	0.86	0.014	0	-	0

Sample / SSA[a]	IEC [b,g] (mmol g^{-1})	ℓ^{c} (mm)	$\sigma^{d,g}$ (S cm^{-1})	$H_2O^{e,g}$ (wt %)	$\lambda_{total}{}^{g}$ (H_2O /SO_3^-)	$[H^+]_{est}$ (M)	P_{MeOH} (cm^2 s^{-1}) x 10^7	$\lambda_{freezable}$ (H_2O /SO_3^-)	D_{H2O} x 10^6 (cm^2 s^{-1})	$X_vF_{freezable}{}^{f}$
PVDF-*g*-PSSA										
44.2	2.8	0.110	0.189	60	31	1.23	33	20	-	0.45
42.9	2.8	0.105	0.169	59	29	1.30	33	20	12.4	0.46
31.1	2.03	0.083	0.142	45	23	1.41	24	15	-	0.37
29.3	1.98	0.069	0.134	42	21	1.37	18	10	9.1	0.24
16.1	1.29	0.067	0.087	32	21	1.14	14	8	-	0.17
9	0.32	0.124	0.012	11	22	0.46	0.034	9	4.3	0.073
N117	0.97	0.205	0.079	23	18	1.13	18	9	8.1-8.6	0.17

[a] SSA content for PAN-*g*-*mac*PSSA and PVDF-*g*-PSSA are listed in mol %, and graft %, respectively

[b] Measured by titration

[c] Thickness of membrane (mm)

[d] In-plane A.C impedance measured at room temperature (20 - 22 °C) for water-saturated using a Solartron 1260.

[e] Water Content

[f] Volume fraction of freezable water, $X_vF_{freezable}$ ($F_{freezable} = \lambda_{freezable}/\lambda_{total}$)

[g] Water content, σ, λ_{total} and IEC of PAN-*g*-*mac*PSSA taken from Chuy, C.; Ding, J. F.; Swanson, E.; Holdcroft, S.; Horsfall, J.; Lovell, K. V. *Journal of the Electrochemical Society* **2003**, *150*, E271-E279.

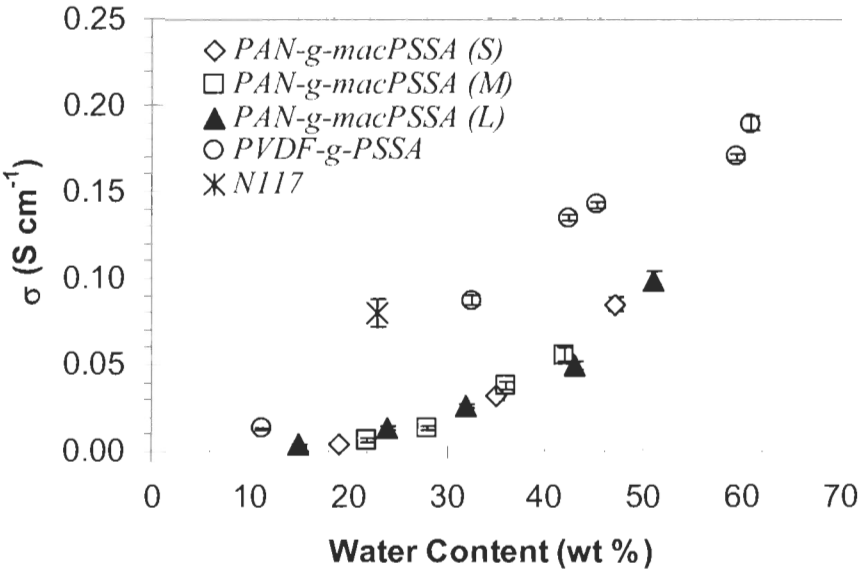

Figure 3.5: Proton conductivity of PAN-*g*-*mac*PSSA, N117 and PVDF-*g*-PSSA membranes as a function of water content.

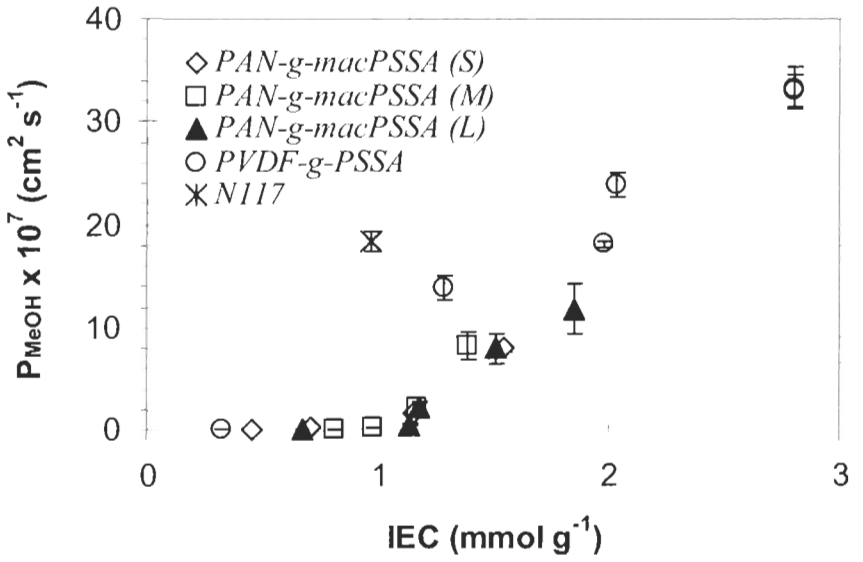

Figure 3.6: Methanol permeability for PAN-*g*-*mac*PSSA, PVDF-*g*-PSSA as a function of IEC.

Structural evolution of phase-separated Nafion® using small angle neutron scattering shows that the separated ionic agglomerates at low water content can lead to an

inverted phase with an interconnected hydrophilic network in the swollen state.[51] The possibility of phase separation due to incompatible hydrophobic/hydrophilic segments in PAN-*g*-*mac*PSSA and PVDF-*g*-PSSA membranes has already been demonstrated by electron microscope images.[103,108,109] These images show that the phase-separated ionic poly(styrenesulfonic) acid agglomerates are sparsely separated for samples with low graft contents, but become increasingly more populated (i.e., higher ionic density) as the graft density in the samples increases. The high proton conductivities observed strongly point to coalescence of ionic clusters upon absorption of water to form interconnected ionic networks.

3.3.2 Methanol Permeability

Methanol permeability ranges between 0.014 x 10^{-7} and 12 x 10^{-7} cm^2 s^{-1} for PAN-*g*-*mac*PSSA, and between 0.033 x 10^{-7} and 33 x 10^{-7} cm^2 s^{-1} for PVDF-*g*-PSSA. Methanol permeability for N117 is 18 x 10^{-7} cm^2 s^{-1}. These results are in agreement with published PVDF-*g*-PSSA[110] and N117[52] data.

The ratio of proton conductivity to methanol permeability (σ/P_{MeOH}) has been suggested as a basis for evaluating DMFC electrolytes and as a measure of the membrane's ability to reject methanol while maintaining proton conductivity.[111] A high (σ/P_{MeOH}) ratio is indicative of a membrane with good methanol exclusion properties. This ratio, normalized relative to Nafion®, is plotted as a function of conductivity in Figure 3.7. The trends show that the ability of the membrane to reject methanol decreases with increasing conductivity, which is a function of IEC and water content of

the sample. The smallest σ/P_{MeOH} ratio measured for styrenic-graft copolymers is 1.3 times greater than that of Nafion®.

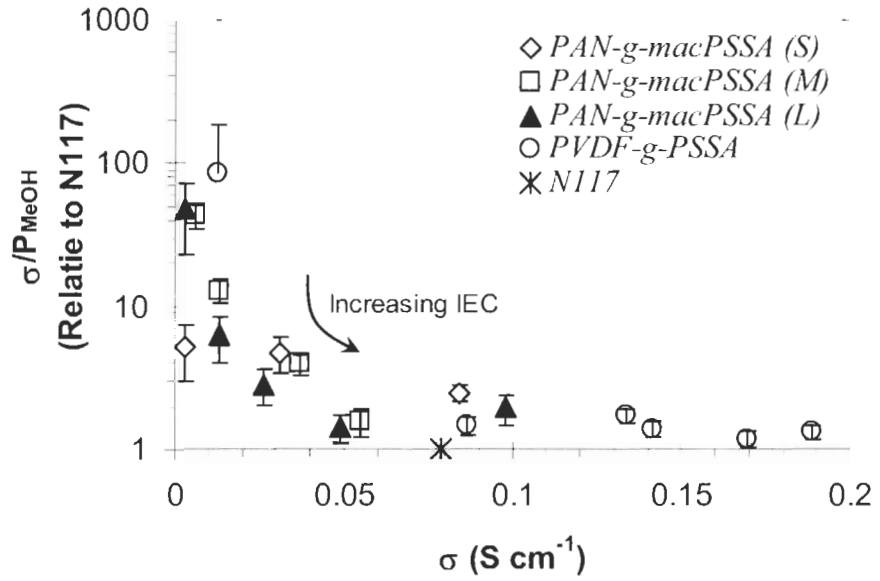

Figure 3.7: Ratio of σ/P_{MeOH} as a function of membrane proton conductivity.

In order to investigate how membrane structure influences methanol transport, the permeability of methanol for each membrane is correlated to its water volume fraction, X_v, as shown in Figure 3.8. Even though P_{MeOH} increases with X_v, as expected, permeability trends show significant variation between different polymer structures. For instance, methanol permeability is much smaller through PAN-*g*-*mac*PSSA than through PVDF-*g*-PSSA and N117 for a given volume fractions of water. Although Nafion® is limited to a single X_v value, data shows that methanol is more permeable through Nafion® than through PVDF-*g*-PSSA for the same X_v.

In considering the relationship between methanol permeability and water volume fraction, we do not account for the fact that a fraction of water inside an ionic membrane

is highly polarized by virtue of it being strongly associated with the ionic groups.[23,52,112] We postulated that permeation of methanol through ionomeric membranes is strongly correlated to the unbound or "free" water, and not simply to the total water present in a membrane. The fraction of free or unbound water may be readily determined using DSC, and is described in the next section.[52,72,113,114]

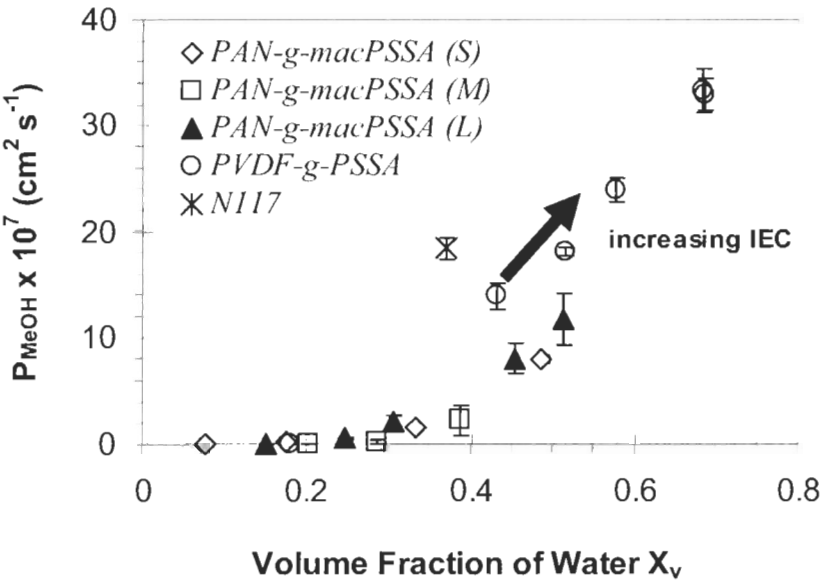

Figure 3.8: Methanol permeability as a function of total water volume fraction, X_v.

3.3.3 Bound and Unbound Water in Hydrated Polymer Electrolyte

In a real system, distinction between the different states of water within a membrane can be difficult to discern because all the water molecules are interchangeable and represent a continuum of states.[69] However, the local environment of water in ionic pores can still be probed by the temperature at which water in the membrane freezes and the heat flow required for the phase change.[58,59] This method of analysis classifies water into freezable and nonfreezable. Nonfreezable water is defined as water that is strongly

bound to either the polymer backbone or the ionic groups and yields no characteristic thermal transition in DSC traces. Freezable water, whether only weakly polarized or liquid-like, exhibits similar thermal transitions to bulk water, but its freezing point can be significantly lowered.

Examples of low temperature DSC thermograms of water-saturated N117, PVDF-*g*-PSSA (1.98 mmol g^{-1}), PAN-*g*-*mac*PSSA (L) (1.18 mmol g^{-1}) and PAN films are displayed in Figure 3.9. Thermograms of other PVDF-*g*-PSSA and PAN-*g*-*mac*PSSA samples were similar in nature to those shown but the positions of transitions and the integrated areas of the peaks varied. The exothermic peaks are due to freezing of water within the membrane, whereas the corresponding endothermic peaks are due to the melting of frozen water. The late onset of fusion at a lower, subzero temperature compared to the melting transition illustrates the known supercooling phenomenon of water.[59]

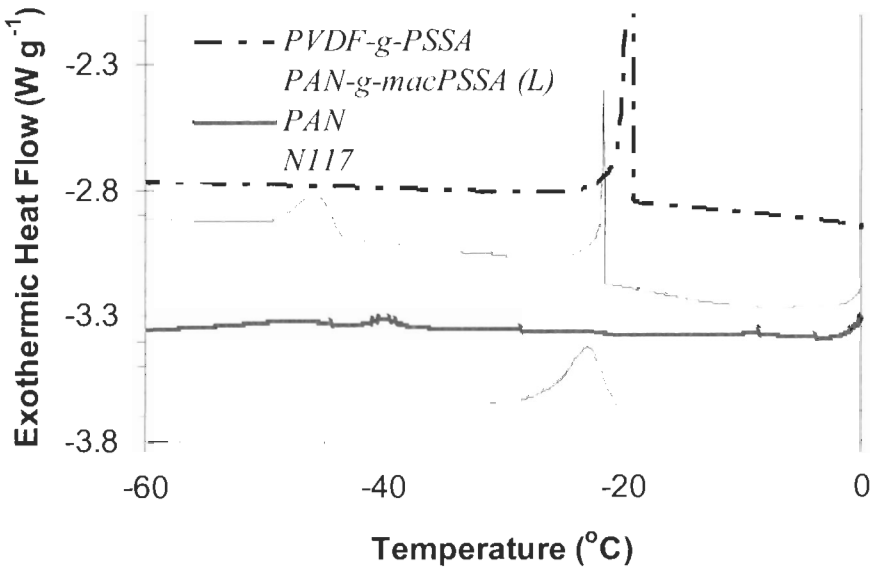

(a)

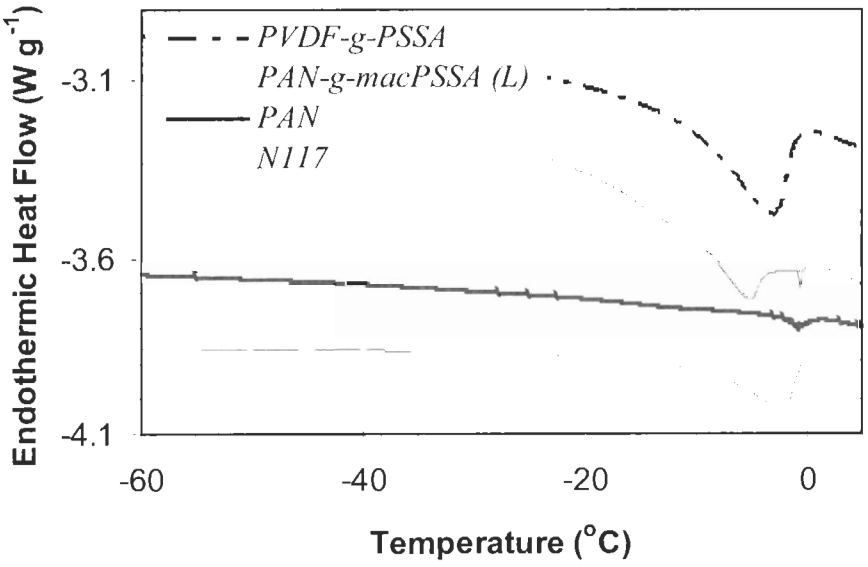

(b)

Figure 3.9: **Low temperature DSC of water-saturated PVDF-*g*-PSSA with 1.98 mmol g^{-1}, PAN-*g*-*mac*PSSA (L) with 1.18 mmol g^{-1}, PAN, and N117. (a) Freezing transitions and (b) melting transitions.**

A single freezing transition was observed for N117 and PVDF-*g*-PSSA. Two freezing transitions were observed for PAN-*g*-*mac*PSSA membranes: a transition between -10 and -20 °C, which is very similar to that observed for freezing of water in N117 and PVDF-*g*-PSSA, and a transition between -40 and – 50 °C. The latter is not usually observed in proton conducting membranes. As nitrile polymers are hygroscopic thermoplastics[115] composed of amorphous and semi-crystalline regions,[116,117] incorporating this non-ionic hygroscopic component in the ion-containing membranes may introduce additional domains in the copolymer that can absorb water. This speculation is confirmed by the presence of a lower temperature peak (between -40 and -50 °C) that corresponds to freezing of water associated to the nitrilic polymer backbone of PAN and of PAN-*g*-*mac*PSSA membranes as illustrated in Figure 3.9. Integrating the area corresponding to this transition for the water-saturated PAN homopolymer film shows that there are on average 0.44 water molecules per CH_2-CH(CN) repeat unit, a value that is similar to that calculated from reported data.[118] However, water associated with the PAN backbone in PAN-*g*-*mac*PSSA membranes does not appear to facilitate methanol permeability because the measured methanol permeability though PAN-*g*-*mac*PSSA is much lower than through either N117 or PVDF-*g*-PSSA.

A melting point of -2.2 °C was detected for water in hydrated N117. Melting points between -1.6 and -4.2 °C were detected for the same transition for hydrated PVDF-*g*-PSSA with IEC between 2.8 to 1.29 mmol g^{-1}, respectively. In contrast to the former two membranes in which single melting points were observed, hydrated PAN-*g*-*mac*PSSA membranes exhibited multiple overlapping peaks.

Integrating the area under the peak corresponding to freezing of water at ~ -23 °C provides a quantitative measure of "freezable/unbound" water in water-swollen membranes. Biological and polymer gel studies show that different water types can result depending on their interaction with the material and their distance from the pore wall or polarized group.[66] Modeling studies of Nafion® show that the permittivity of water in Nafion® is bulk-like near the pore center but decreases with decreasing radial distance from the pore wall in which the SO_3^- groups are situated in Nafion®.[63,91] Water molecules in this vicinity are highly polarized by virtue of being in close proximity to an ion and are unable to crystallize.[58] Water that bears the closest resemblance to bulk water (e.g., in the pore center) is expected to crystallize first. Residual water molecules that cannot reorientate themselves and pack into a crystal lattice are termed non-freezable or bound water. The content of free water estimated by pore permittivity calculations accounts for approximately 50 % of the total water in a fully hydrated Nafion® pore, which is in agreement with the fraction of freezable water for water-saturated Nafion® membranes measured by DSC.[113] Modeling studies by Pintauro *et al.*[67] and Paddison and *et al.*[23,63] showed that the permittivity of this water is similar to bulk water (within < 10 %) so that water that freezes may be defined as free water. Values of $\lambda_{freezable}$ for test membranes were determined by low temperature DSC and are tabulated in Table 3.1.

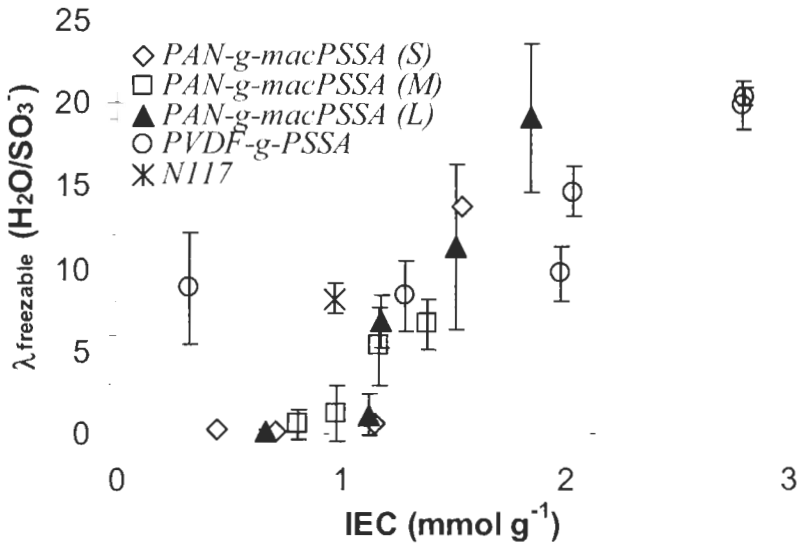

Figure 3.10: Content of freezable water in water-saturated membranes as a function of IEC.

The amount of freezable/free water in PAN-*g*-*mac*PSSA membranes decreases with decreasing IEC and approaches zero for polymers with very low IEC (Figure 3.10). However, $\lambda_{freezable}$ does not drop to zero for PVDF-*g*-PSSA membranes but instead appears to remain constant at ~ 8.5 H_2O/SO_3^-. This difference is perhaps related to the innate behaviour of each polymer. Although PVDF-*g*-PSSA has a high content of freezable water at low IEC, it is speculated that the ionic percolation network for PVDF-*g*-PSSA possessing low IECs is poorly formed because methanol permeabilities are low (0.034×10^{-6} cm^2 s^{-1}).

A plot of P_{MeOH} *versus* the product of X_v and $F_{freezable}$ is illustrated in Figure 3.11. In this case, $F_{freezable}$ is the mole fraction of free water corresponding to the peak at -23 °C or the ionic region of PAN-g-macPSSA and hence the product $X_vF_{freezable}$ represents the volume fraction of free water in the ionic region. Methanol permeability exhibits an increasing trend with increasing volume fraction of free water in the ionic phase of the

polymer. However, the fact that methanol permeability is consistently lower for PAN-*g*-*mac*PSSA compared to PVDF-*g*-PSSA for the same volume of free water strongly suggests that there are other factors that contribute to the selectivity of the membrane, e,g., morphology and interaction of the water/polymer phase. These are considered in the next section.

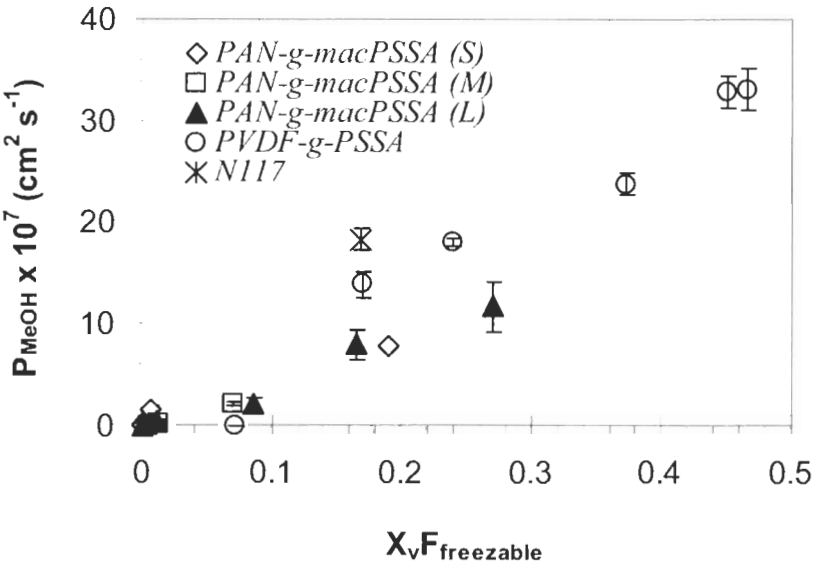

Figure 3.11: Plot of methanol permeability *versus* volume fraction of freezable water ($X_vF_{freezable}$).

3.3.4 Morphological Features of Poly(styrenesulfonic) Acid-Based Membranes

Numerous investigators have attempted to reconcile structural information with observed properties (specifically, transport properties) in order to develop a well-defined morphological model for perfluorosulfonate ionomers. The interplay of ionic domains, the random chemical structure of the copolymer, the morphological variations with solvent swelling, the relatively low degree of crystallinity, and the heterogeneous nature of the morphology adds to the complexity.[19] Central to the morphological models that have been developed is the recognition that ionic aggregates in the perfluorinated

polymer matrix coalesce with uptake of water, forming nanometer-scale domains that allow for efficient ion transport. Small angle X-ray and neutron scattering, transmission electron microscopy and atomic force microscopy investigations of dehydrated Nafion® reveal spherical ionic clusters ~ 1.5 – 6 nm in diameter.[19] Ionic clusters swell but cluster densities decrease upon absorbing water. The reported size of the swollen aggregates varies depending on the study and the method used; however, most studies indicate that cluster diameters swell up to 2 times their size in the hydrated state.[19,119-121]

The morphology of PAN-*g*-*mac*PSSA membranes determined using TEM has been reported elsewhere.[103] The ionic domains exist as worm-like regions, which become more rod-like and eventually globular with decreasing ionic content. This pattern is similar for all three series of PAN-*g*-*mac*PSSA membranes, regardless of the side chain length. The average ionic domain dimension for PAN-*g*-*mac*PSSA varies between 4 -18 nm. The size of the ionic clusters appears to be independent of the side chain length and IEC. However, ionic domains are expected to coalesce upon water uptake.

A TEM image of PVDF-*g*-PSSA with 2.03 mmol g^{-1} is presented in Figure 3.12. The white globular and thread-like structures represent the PVDF matrix, and the dark regions are Pb^{2+}-stained ionic domains. Morphological studies of divinylbenzene- and bis(vinylphenyl)ethane-crosslinked PVDF-*g*-PSSA by Hietala *et al.* reveal that the reactive sites by irradiation are formed on the surfaces of both crystalline and amorphous regions of the PVDF matrix in a random fashion.[109] Incompatibility between sulphonated styrene and PVDF leads to a gross phase-separated structure that is consistent with the literature.[109] TEM photographs of PVDF-*g*-PSSA membranes

reported in the literature show that the polymer substrate becomes more thread-like and less crystalline with increasing IEC. The distance between the globular and strand structures (or ionic regions) varies in size, with the largest domains at 250 nm.[81,109] By virtue of the large ionic clusters size, PVDF-*g*-PSSA membranes should possess the highest permeation rate, followed by PAN-*g*-*mac*PSSA and N117 membranes. However, unlike Nafion® which has been modeled by a cylindrical pore geometry[67] with ions lining the pore, the ionic conduits in the styrene-grafted polymers are less well defined and may restrict free movement of species, which is discussed in more detail below.

In an operating DMFC, a polymer electrolyte is always maintained in a water-saturated state. As formerly indicated, water in the membrane can exist in two states depending on the degree of hydration and interaction with the polymer. Self-diffusion coefficients of water appear to be affected by these interactions. Measurements of self-diffusion coefficients of water in hydrated membranes by PFG-NMR offer insight into the ease of movement, boundaries and impediments within the pores of a membrane. A logarithmic plot of the signal attenuation as a function of increasing gradient strength ($\gamma^2 g^2 \delta^2(\Delta-\delta/3)$) (equation 3.3) yields a straight line from which the diffusion coefficient can be extrapolated for freely diffusing species. Signal attenuation of bulk water and water in N117, PVDF-*g*-PSSA, and PAN-*g*-PSSA are displayed in Figure 3.13. Signal attenuation for PVDF-*g*-PSSA and PAN-*g*-PSSA membranes exhibits a change in slope with increasing gradient strength which indicates distinct diffusion processes.

Studies of water-swollen tablets[122] show that multiple relaxation processes related to water and mobile polymer units are possible. Diffusion of fast-moving protonic species, determined from the slope of the initial region (low gradient strength), is

attributed to water. The coefficient observed varies with Δ (diffusion time) as illustrated in Figure 3.14 for PAN-*g*-*mac*PSSA (S) 1.15 mmol g^{-1}. For small Δ values, water molecules in restricted geometries diffuse freely so the observed diffusion is large. As Δ is allowed to increase, a transition from free diffusion to restricted diffusion occurs wherein water diffusion experiences both surface and pore wall effects. Under conditions of large Δ, signal attenuation becomes more sensitive to the shape and dimension of the restrictive geometry and the diffusion coefficient at that point becomes independent of time.[123,124] Water self-diffusion coefficients in PAN-*g*-PSSA (S) (for IEC 1.15 and 1.54 mmol g-1) and N117 membranes are shown Table 3.1.

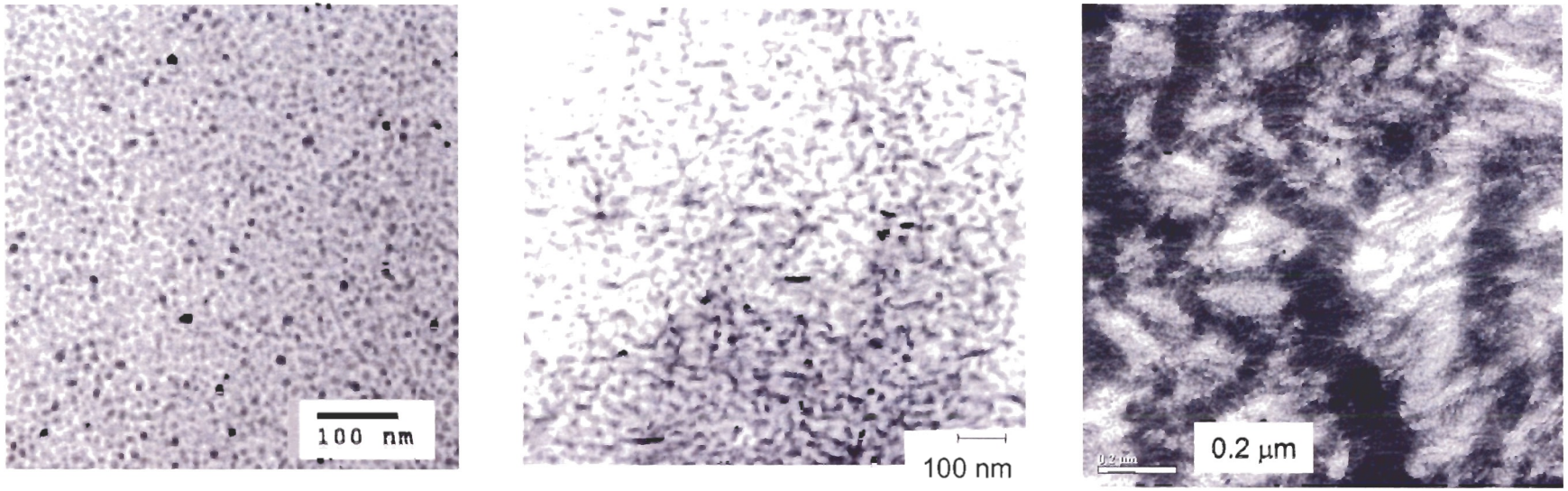

(a) (b) (c)

Figure 3.12: **TEM image of (a) Nafion® (N117), (b) PAN-*g*-*mac*PSSA (L) with 13.7 SSA% (reprinted with permission J. Electrochem. Soc. 2003, *150*, E271-E279. © 2003 The Electrochemical Society), and (c) PVDF-*g*-PSSA (2.03 mmol g^{-1}).**

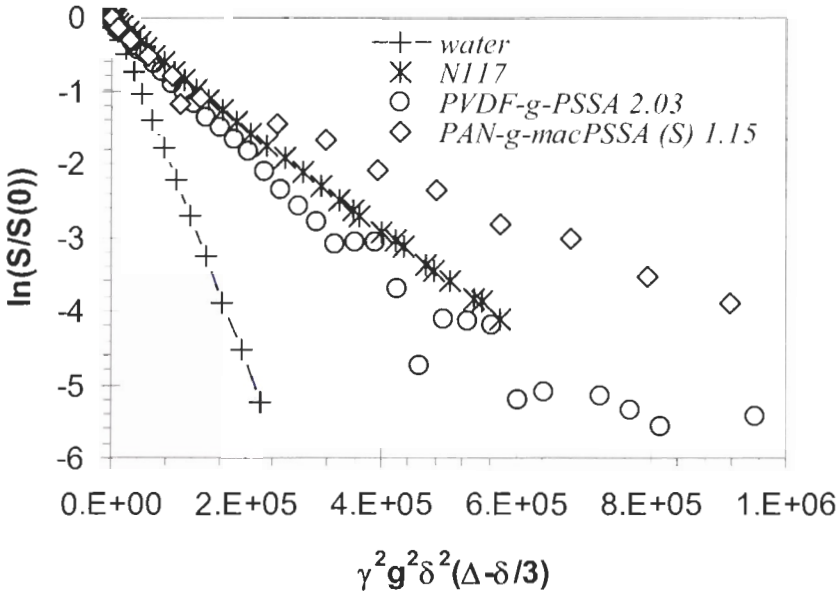

Figure 3.13: Logarithm plot of ^{1}H signal attenuation for water, and water-saturated membranes: N117, PVDF-*g*-PSSA (2.03 mmol g^{-1}), and PAN-*g*-*mac*PSSA (S) (1.15 mmol g^{-1}).

The water self-diffusion coefficients reported in the literature for water-saturated N117[57,125,126] vary between 3.5 – 8.5 x 10^{-6} cm^2 s^{-1} while that for water-saturated PVDF-*g*-PSSA[106,125] possessing different IECs vary from 9.5 to 14 x 10^{-6} cm^2 s^{-1}. The root means square displacement of water molecules in membranes was calculated using equation 3.4[123] to give an estimate of the average distance travelled by the water molecule during the NMR sampling time. Displacements of 0.0002 – 0.005 cm indicate the experimental sampling times are sufficiently long to probe macroscopic diffusion, and to provide representative information on the inherent tortuosity of the hydrophilic domains.

$$< x^2 >^{\frac{1}{2}} = 3D_{app}\Delta \qquad (3.4)$$

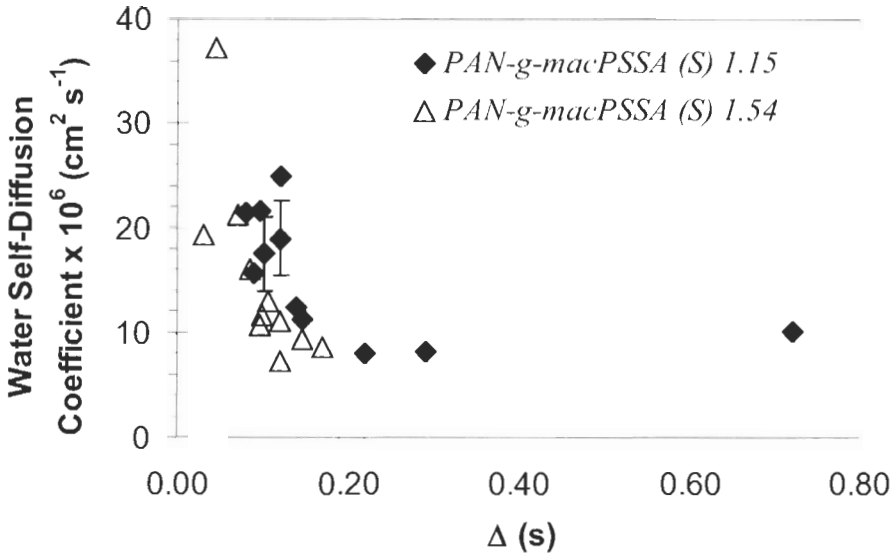

Figure 3.14: Apparent self-diffusion coefficient of water in PAN-*g*-macPSSA (S) with 1.15 and 1.54 mmol g^{-1}.

Measured diffusion coefficients of water in membranes are smaller than in bulk water (2.3 x 10^{-5} cm^2 s^{-1}), a result that is consistent with boundary restrictions present in the membrane's hydrophilic phase. PAN-*g*-*mac*PSSA membranes possess relatively higher water contents (and larger λ values) than Nafion® 117, but despite this the diffusion coefficients in PAN-*g*-*mac*PSSA are similar to that observed for Nafion®. This result implies that the water/ion-containing network is more tortuous and restrictive for PAN-*g*-*mac*PSSA membranes. The D_{H2O} for PVDF-*g*-PSSA membranes with low IEC (and hence low λ) is also lower than for Nafion®, and is attributed to a poorly-formed ionic network. In contrast, hydrated PVDF-*g*-PSSA membranes possessing a high IEC exhibit much larger water diffusion coefficients because water uptake and λ values are much larger, and the network of ionic/water domains is also much better developed.

The formation of a bi-continuous network depends on how effective the ionic domains connect. Because PSSA is constrained to the polymer backbone in PAN-*g*-

*mac*PSSA, gross phase-separation at the micron level does not occur; however, dissolution of the polymer and casting leads to a "frustrated", nano-structured morphology. PVDF-*g*-PSSA membranes are not re-cast, and are formed by filling the PVDF matrix with PSSA, which swells upon absorbing water. Both of these structures are in contrast to Nafion® which is thought to form well defined pores.[49,67]

3.3.5 Interaction of Small Molecules in the Ionic Phase of Poly(styrene sulfonic) Acid-Containing Polymers

Water diffusion, proton transport and oxygen diffusion data for a single N117, PVDF-*g*-PSSA and PAN-*g*-*mac*PSSA membrane of similar methanol exclusion ability (i.e., $\sigma/P_{MeOH} = 1 - 2$) are illustrated in Table 3.2. In this particular case, proton conductivity values increased from 0.08 to 0.10 S cm^{-1} in the order of N117, PVDF-*g*-PSSA and PAN-*g*-*mac*PSSA. The relatively constant concentration of protons of ~ 1.1 M for all the three samples, but higher proton mobility of PAN-*g*-*mac*PSSA compared to the other two samples show that the enhancement in the proton conductivity in PAN-*g*-*mac*PSSA is perhaps related to the membrane's higher proton mobility and content of free water.

Table 3.2: Comparison of single membrane data for N117, PVDF-*g*-PSSA and PAN-*g*-*mac*PSSA

	N117	PVDF-g-PSSA	PAN-*g*-*mac*PSSA
σ/P_{MeOH} (Normalized to N117)	1.0	1.3	2
σ ($S\ cm^{-1}$)	~ 0.08	~ 0.09	~ 0.1
$P_{MeOH} \times 10^7$ ($cm^2\ s^{-1}$)	18	14	12
$[H^+]$ (M)	1.1	1.1	0.9
$\mu \times 10^3$ ($cm^2\ s^{-1}\ V^{-1}$)	0.7	0.8	1.0
λ_{total} (H_2O/SO_3^-)	18	21	36
$\lambda_{freezable}$ (H_2O/SO_3^-)	8	8	19
$D_{O2} \times 10^6$ ($cm^2\ s^{-1}$)*	9.3	9.2	15.6
$D_{H2O} \times 10^6$ ($cm^2\ s^{-1}$)	~ 8	~ 9	~ 9
X_v (total)	0.38	0.44	0.5
$X_v F_{freezable}$	0.16	0.16	0.28

* Chuy-Sam, Carmen M. Influence of Morphology on the Electrochemical Properties of Proton Exchange Membranes. *Dissertation*. Simon Fraser University, 2002.

The permeability of methanol in PAN-*g*-*mac*PSSA is still lower than the other two samples even though this PEM possesses more free water in the ionic phase. The diffusion coefficients of smaller molecules, such as oxygen, are high in PAN-*g*-*mac*PSSA as one would expect with high water contents, which suggest that the reduction of methanol permeability is perhaps not so much dependent on the rate of methanol

diffusion, in this case. Since methanol permeability is the product of a diffusion term and a partition coefficient term, the reduction in methanol permeability through PAN-*g*-*mac*PSSA may be related to its low partition coefficient since the diffusion of methanol, based on diffusion measurements of other small molecules, is expected to be high. It has been demonstrated that a reduction of ~ 30 % in methanol permeability, without compromise in proton conductivity, was possible[127] through Nafion® after depositing alternate layers of positively and negatively charged polymer electrolytes. The modified region has been speculated to work by blocking effective diffusion of methanol. However, the ability of the modified membrane to transport small molecules, such as protons, may indicate that diffusion of small molecules through the modified region is relatively easy. The selectivity of the membrane is perhaps related to the interaction and solubility of methanol in the polymer. The influence of the partition coefficient on methanol permeability has yet to be verified in detail.

3.3.6 Methanol Permeability *versus* Proton Conductivity

Designing membranes that reject methanol while maintaining appropriate proton conduction is a challenge because membranes that are designed to possess lower methanol permeability often exhibit lower proton conductivity. For this reason, it is necessary to examine the relationship between conductivity and permeability. The change in proton conductivity of the membrane with volume fraction of free water is illustrated in Figure 3.15. The effect of differences in pKa of the acids in different membrane classes are expected to be minimal because equilibrium calculations of acid concentrations using the pKa values of -2 and -6 for *p*-toluenesulfonic acid and triflic

acid, respectively,[20] showed 96 - 100 % dissociation of the acid for the 2 – 4 M acid concentration estimated within the membrane pores.

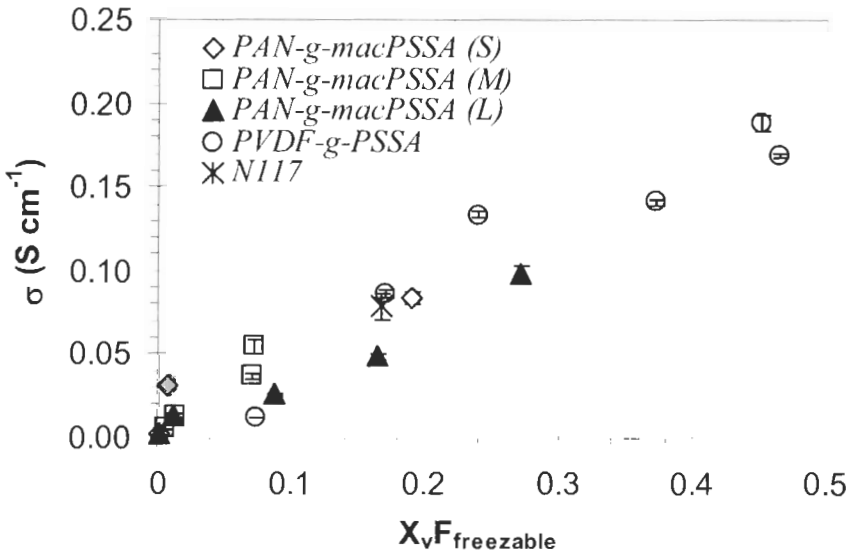

Figure 3.15: Proton conductivity, σ, of N117, PAN-*g*-*mac*PSSA, and PVDF-*g*-PSSA membranes as a function of volume fraction of freezable water, $X_vF_{freezable}$.

Proton conductivity values are between 0.003- 0.03 S cm^{-1} for volume fraction of freezable water ($X_vF_{Freezable}$) between 0 and 0.1. Methanol permeabilities in this region of $X_vF_{Freezable}$ are at least 9 times lower than that of Nafion®. The data shows that methanol permeability can be substantially lowered by designing membranes with little or no freezable water. Noting that recent low temperature conductivity studies of Nafion® and radiation grafted membranes[113] of ionic conduits with only non-freezable water can still yield reasonable proton conductivities, we speculate that membranes containing only non-freezable water would yield an even lower methanol permeability. However, the styrenic systems studied here showed poor conductivity (i.e., < 0.003 S cm^{-1}) in the absence of freezable water (i.e., for low IEC membranes) in the absence of a well-

defined, continuous ionic network. More understanding is needed in order to develop membranes that possess continuous pore structures containing only non-freezable water.

3.4 Conclusions

Two classes of polymers (PAN-*g*-*mac*PSSA and PVDF-*g*-PSSA) were studied and compared to Nafion®. Their properties depend strongly on the IEC. PAN-*g*-*mac*PSSA membranes, which consisted of controlled microstructures showed that, in this instance, altering the length of the graft was not effective in fine-tuning the water content, proton conductivity, and methanol permeability of the membrane. The association of water with the polymer backbone in PAN-*g*-*mac*PSSA is a new finding for proton conducting membranes but appears to have minimal effect on the permeability of the membrane. Its effect on other properties of the membranes is as of yet unknown.

Increasing proton conductivity of PAN-*g*-*mac*PSSA and PVDF-*g*-PSSA membranes by increasing the density of hydrophilic pendant units (i.e., increasing the IEC) also increases methanol permeability due to a higher content of free water and a corresponding enhancement in channel percolation.

Methanol permeability through high IEC PVDF-*g*-PSSA membranes is larger than for N117 and PAN-*g*-*mac*PSSA membranes because water uptake and λ values are much larger, and the network of ionic/water domains is much better developed. Despite the higher absolute methanol permeability of PVDF-*g*-PSSA, the σ/P_{MeOH} ratio is still higher in comparison to N117 because PVDF-*g*-PSSA membranes possesses much higher proton conductivity.

Methanol permeability through PAN-*g*-*mac*PSSA membranes is consistently lower than in PVDF-*g*-PSSA and Nafion® membranes. The relatively large diffusion coefficient of small molecules in PAN-*g*-*mac*PSSA strongly points to a lower solubility or partition coefficient of methanol in PAN-*g*-*mac*PSSA, assuming the methanol rejection ability of PAN-*g*-*mac*PSSA is better than either N117 and PVDF-*g*-PSSA.

CHAPTER 4:

NOVEL APPROACH TO IMPROVE WATER TRANSPORT IN GRAFT COPOLYMERS

4.1 Introduction

Research findings in Chapter 2 demonstrated that proton mobility and proton transport are reliant on the interaction between water molecules and SO_3- groups in the ionic network of well-percolated proton exchange membrane (PEM). Since proton conductivity is a membrane parameter that relates to Ohmic resistance of a fuel cell, PEMs with high conductivity values, such as poly(vinylidene difluoride) irradiation grafted with poly(styrenesulfonic) acid (PVDF-*g*-PSSA), and poly(ethylenetetrafluoroethylene) irradiation grafted with poly(styrenesulfonic) acid (ETFE-*g*-PSSA) for which proton conductivities are between 0.1 - 0.2 S cm^{-1}, should in principle produce fuel cell performances that should exceed that of baseline Nafion® (N117) in which the proton conductivity is 0.1 S cm^{-1}.

In general, a fuel cell system is considered superior when its polarization profile (or voltage-current curve) is higher than the one that it is being compared against. The voltage-current fuel cell polarizations for ETFE-*g*-PSSA membranes with hydrogen and oxygen as reactant gasses are presented in Figure 4.1. The data, which has been iR corrected to remove the effect of membrane thickness, shows a clear increasing performance trend with increasing membrane IEC. Even though ETFE-*g*-PSSA membranes possess a higher *ex-situ* proton conductivity (0.1 – 0.2 S cm^{-1}) and more free water content (see Table 2.1) than Nafion®, only ETFE-*g*-PSSA with the highest IEC exhibits a performance profile that exceeds Nafion® and even then only at current densities < 200 mA/cm^2. These results appear to contradict our understanding of how membrane resistance relates to membrane hydration. However, the dynamic nature of an

operating fuel cell requires not only good proton transport but also good water management, and this topic is discussed in more detail below.

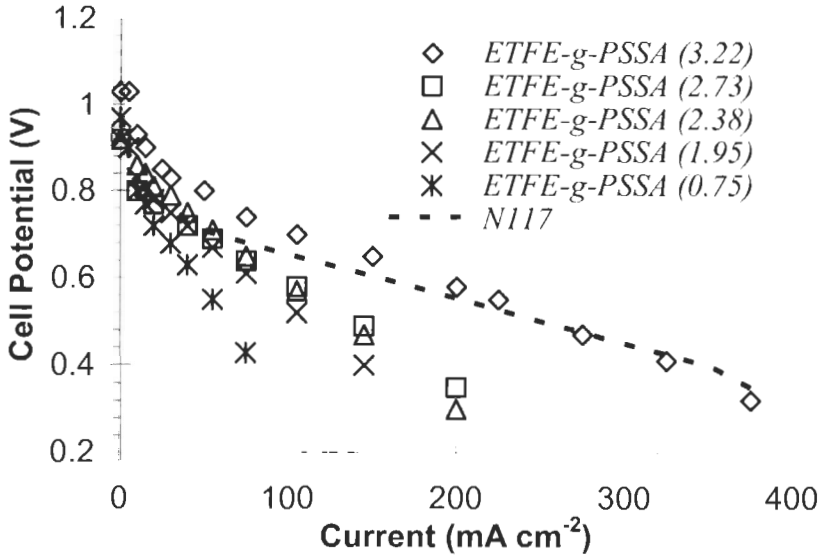

Figure 4.1: Fuel cell polarization curves of ETFE-*g*-PSSA membranes containing different ionic contents and of Nafion®. Anode and cathode contained 0.75 mg Pt cm^{-2} of catalyst and 20 wt % of Nafion® binder. Fuel cell was operated at 25 °C and at ambient pressuer with a variable flow rate of 20 mL min^{-1} A^{-1} in addition to a base flow rate of 30 mL min^{-1} which corresponded to a stoichiometry of 14 – 1.8 for H_2 and 28 – 3.6 for O_2 for current densities of 0.2 – 1.0 A cm^{-2}. The gases were fully humidified at 40 °C (~95 % RH). Data reproduced from Navessin, T.; Eikerling, M.; Wang, Q. P.; Song, D. T.; Liu, Z. S.; Horsfall, J.; Lovell, K. V.; Holdcroft, S. *Journal of the Electrochemical Society* 2005, *152*, A796-A805.

Water management is a term that refers to the many issues associated with maintaining appropriate water balance in a fuel cell during operation. This includes preventing the anode from dehydrating (due to electro-osmotic drag) and the cathode from flooding. Numerous studies and solutions have been suggested.[30-34,37-39] They focus primarily on: (1) designing new gas flow fields channels with improved differential pressure loss, (2) designing new gas diffusion layers to help wick away excess water

from the cathode to prevent flooding, (3) humidifying the anode to prevent anode from drying out (but this adds to parasitic losses to the cell), (4) supplying a pressure difference across the PEM (normally between 5 – 15 psig) to help push excess water back to the anode, and (5) maintaining the membrane in a well hydrated state by controlling water transport. This, in itself is a challenge because water can move across the membrane in many ways during operation. The different modes of water transport are schematically illustrated in Figure 4.2.

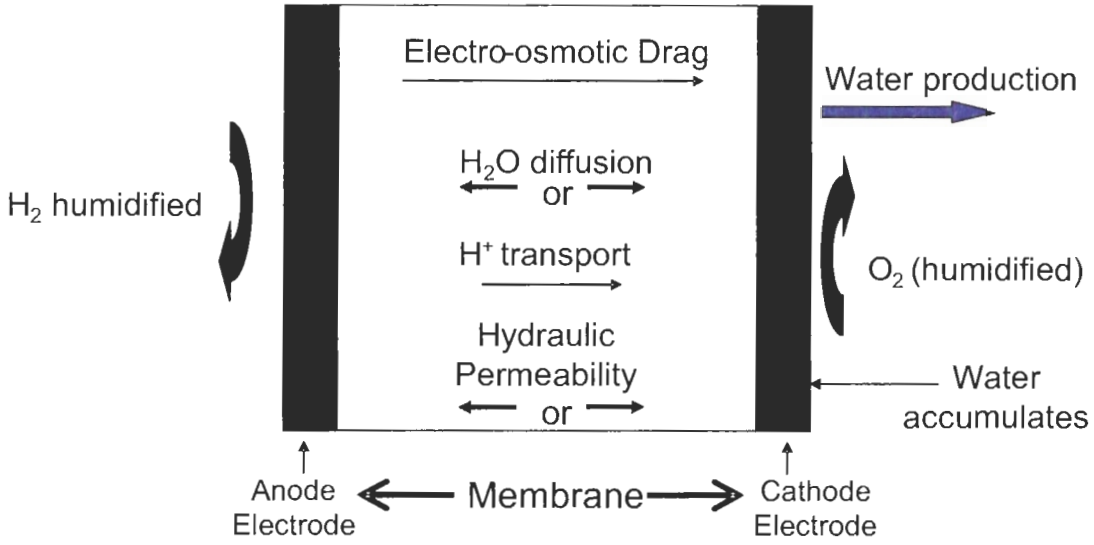

Figure 4.2: Schematic diagram illustrating different modes of water transport in a fuel cell.

Proton transport from the anode to the cathode, in most cases, entails some movement of water in the direction of the current flow. This phenomenon is known as electro-osmotic drag. The electroosmotic coefficient, n_{drag}, is a ratio that estimates moles of water co-transported with each mole of proton. Two phenomena contribute to this drag: firstly, protons are solvated and move in the hydrated form (in the case of H_3O^+ or any water-proton cluster); secondly, moving protonic water clusters pull nearby water molecules in their direction. This effect adds a hydrodynamic component to the drag.

Depending on the direction of the water gradient, diffusion of water can be a forward transport (towards the cathode) or a backward transport (towards the anode). In direct methanol fuel cells, water flux is always in the forward direction because a liquid-phase is always present at the anode. In hydrogen/air fuel cells, electro-osmosis establishes a water concentration gradient through the membrane that in most circumstances drive water back to the anode.[33,128,129] The efficiency of this flux depends a lot on the nature, design and thickness of the membrane. A membrane with good water transport properties in the backwards direction not only may reduce Ohmic resistance due to membrane dehydration, but it may also help with removing excess water at the polymer/electrode interface.

In the ETFE-*g*-PSSA polarization profiles illustrated in Figure 4.1, Navessin *et al.*[130] showed through electrochemical impedance spectroscopy that the increase in membrane resistance and contact resistance of the membrane electrode assembly (MEA) observed with decreasing membrane IEC was attributed to the poor ability of the membrane to rehydrate itself by back-diffusion of water. Andreaus *et al.* observed a similar problem in a fuel cell with Nafion® when the current density load applied to fuel cell increased.[30]

Many research studies indicate that reducing the thickness of PEMs helps maintain a more evenly hydrated membrane during fuel cell operation.[131] This method is widely employed in the fuel cell industry to reduce Ohmic resistance and to increase fuel cell performance. The use of membranes with low electro-osmotic drag coefficients, such as phosphoric acid doped polybenzimidazole (PBI) in high temperature fuel cells, also appears to reduce the problems associated with water management.[132] Incorporating

inorganic components that encourage crossover gases to react in order to allow the membrane to self-hydrate, has also reduced the effect of electro-osmosis in membranes.[133]

Another approach, which is also a focus for this work, is to facilitate water back transport by providing an alternate pathway through which water can migrate. The concept involves incorporating polar, non-ionic polymer segments into the PEM. Hydroxyethylmethacrylate (HEMA), which has the propensity to absorb water, is polymerized to PVDF-*g*-PSSA *via* two methods: (1) simultaneous co-polymerization of HEMA and styrene as grafts to poly(vinyledene difluoride) (PVDF), and (2) polymerization of HEMA to gamma irradiated PVDF-*g*-PSSA as illustrated in Figure 4.3. The different synthetic processes will make available different membrane structures for comparison. The structure-property relationship of HEMA-containing PVDF-*g*-PSSA membranes will be compared to unmodified PVDF-*g*-PSSA membranes.

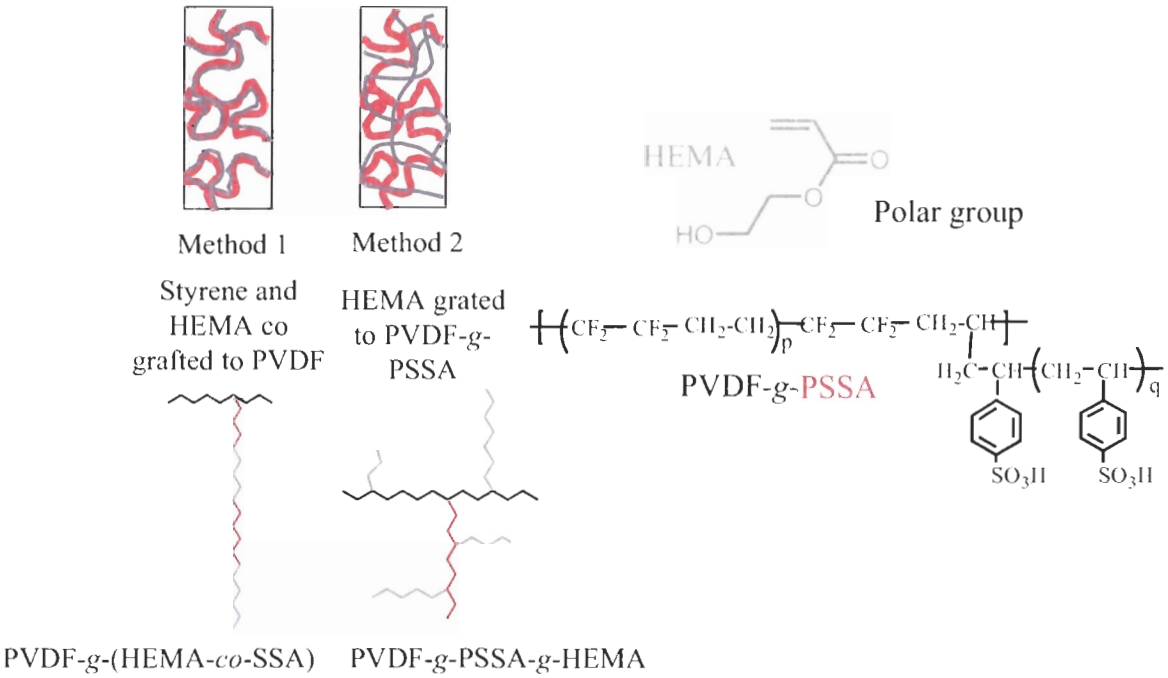

Figure 4.3: Grafting of polar non-ionic HEMA moieties to PVDF-*g*-PSSA by (1) copolymerization of styrene and HEMA, and (2) polymerization of HEMA to PVDF-*g*-PSSA.

4.2 Experimental

4.2.1 Membrane Synthesis

Radiation-grafted HEMA-containing PVDF-*g*-PSSA and unmodified PVDF-*g*-PSSA membranes were both provided by K. Lovell and co-workers (Cranfield University, U.K.). A description of PVDF-*g*-PSSA synthesis is given in section 3.2.2. HEMA-containing PVDF-*g*-PSSA was synthesized by two different techniques. The first technique involved copolymerization of HEMA and styrene to PVDF using toluene as a solvent. The dried grafted film was sulfonated by immersion in a solution of 5% (V/V) chlorosulphonic acid in dichloromethane, for 2 h at ambient temperature, and then washed to neutrality with DI water to afford the structure shown in Figure 4.3. The second method required two irradiation steps. A gamma-irradiated PVDF film was

immersed in a solution of styrene and toluene to initiate polymerization of styrene. The grafted film was sulphonated using 5% (V/V) chlorosulphonic acid and then dried. The film was irradiated again with 1Mrad or 10kGy gamma radiation and immersed in a 1 - 2 % HEMA containing DI water at 60 ^{o}C for 5 hours. A schematic representation of the desired product is illustrated in Figure 4.3. The unmodified membrane is denoted PVDF-*g*-PSSA; HEMA-containing PVDF-*g*-PSSAs membranes are denoted PVDF-*g*-P(HEMA-*co*-SSA) and PVDF-*g*-PSSA-*g*-HEMA for PVDF-g-PSSA modified using methods 1 and 2, respectively. The number in the brackets after the polymer states the IEC of the polymer.

4.2.2 Membrane Acidification

Radiation grafted and commercially available N117 (from Ion Power) were acquired in the membrane form, and were acidified by following the procedure in section 2.2.1. Protonated membranes were stored in Millipore water until use.

4.2.3 Membrane Characterization

4.2.3.1 Ion Exchange Capacity, Water Content, Acid Concentration, and State of Water

Ion exchange capacities (IEC) were determined by NaOH titration of acid released from membranes in their protonic form in 2 M NaCl. The volume fraction of water in a water-swollen membrane, X_v, was calculated by converting the mass of water to volume using the density of water (1 g mL^{-1}), and the volume of the hydrated membrane using the density of the hydrated membrane.

Water contents were determined from the mass ratio of water absorbed by the membrane from the dry state to the mass of the water-saturated membrane. The samples were dried in vacuo at 80 °C for 1 day. Acid concentrations in the membranes were estimated using equation 2.3.[113] The fraction of freezable-water in the water-saturated membranes was determined using the same calorimetric techniques described in section 2.2.5. From conservation of mass, the total fraction of water in the membrane should be the sum of freezable and non-freezable water.

4.2.3.2 Attenuated Total Reflectance – Fourier Transform Infrared Spectroscopy (ATR-FTIR)

The presence of HEMA units in PVDF-*g*-PSSA was confirmed by performing attenuated total reflectance infrared spectroscopy. Spectra were collected using a Thermo Nicolet, Nexus 470-FT-IR. Samples, after drying in a vacuum oven at 80 °C for 24 h, were pressed against a KRS-5 crystal prism. The whole assembly was placed 45° from the incident beam in the FTIR with 1000 scans collected. The beam penetration was only a few microns from the surface. Moisture and CO_2 were kept out of the FTIR by a constant nitrogen purge.

4.2.3.3 Hydraulic Permeability and Water Vapour Transmission

The continuity of the ionic and HEMA regions through the membrane and its effect of water transport were determined by measuring their hydraulic permeability and water vapour permeance values. An increase of permeability values was expected from samples with HEMA than without HEMA because of a potential increase in number of hydrophilic pores for water transport.

A 1 inch diameter circle of the water-swollen sample in H^+ form was cut for the hydraulic permeability experiment. The sample was assembled in the order of metal mesh, sample and o-ring, in a stainless steel fixture as shown in Figure 4.4. The set-up was placed in an isothermal chamber maintained at 30 °C. Care was taken to prevent the sample from dehydrating during the assembly process. De-ionized water of known pressure was applied to one side of the membrane using a syringe pump. The hydraulic permeability coefficient of water was determined by measuring the flow rate of water generated through the membrane.

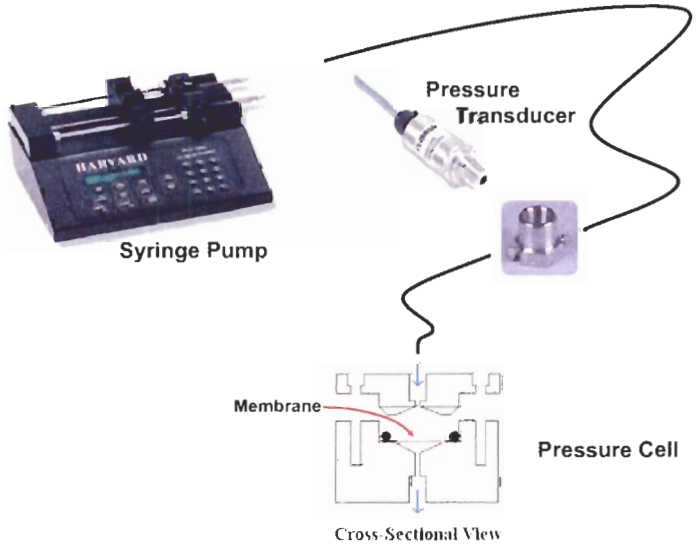

Figure 4.4: Schematic drawing of the hydraulic permeability set-up.

From Darcy's Law,

$$Q = \frac{V}{t} \propto \frac{p}{l} \tag{4.1}$$

$$\frac{Q}{A} = K_{II} p \tag{4.2}$$

$$P_{H2O,hydraulic} = /K_{II} \tag{4.3}$$

where V is volume of water, Q is the volume flow rate, A is the membrane area, p is the pressure drop, l is the membrane thickness, K_H is the hydraulic permeance, and l/K_H is the thickness normalized hydraulic permeability coefficient or $P_{H2O,hydraulic}$. The magnitude of the hydraulic permeability is a membrane property that depends on membrane morphology, size of the ionic pore and viscosity of the fluid within the ionic pores.

Details of the water transmission experiment are discussed in detail elsewhere.[134] Briefly, a hole of approximately 15 mm was drilled through the cap of a 2 Dram vial. An air dried sample, in H^+ form, was placed in between the cap and the cap insert, which also had a 15 mm hole drilled into it. Millipore water was added to the vial to a level that was no less than 19 mm from the specimen in order to reduce the risk of the membrane coming into contact with the sample when the vial was handled. The cap with the sample held in place was screwed tightly to the water-containing vial. The whole assembly was weighed and placed in an environmental chamber (ESPEC SH-241) at 60 °C and 40 % RH to form a vapour pressure gradient that ranged between 40 – 100 % through the sample. The loss of water through the membrane with time was monitored periodically. Fitting the data to the equation below yielded the vapour permeance from which the vapour transport permeability coefficient, $P_{H2O,WVT}$, was derived by multiplying the permeance by the membrane thickness.

$$\text{WVT (in units of g cm}^{-2}\text{ s}^{-1}) = \left(\frac{G}{t}\right)\frac{l}{A} \tag{4.4}$$

$$\text{Vapour Permeance} = K_v = \frac{WVT}{\Delta p} = \frac{WVT}{S(R_1 - R_2)} \tag{4.5}$$

$$P_{H2O,VWT} = l\,K_v \tag{4.6}$$

where WVT is the rate of water vapor transmission, G is the weight change, t is the time at which G is measured, $\frac{G}{t}$ is the slope of the straight line of G *versus* t plot, A is the test area, S is the saturation vapour pressure at the test temperature (e.g., 60 °C), Δp is the vapour pressure difference, R_1 is the relative humidity in the vial (e.g., 100 %), R_2 is the relative humidity of the chamber (e.g., 40 %), and K_v is the vapour permeance.

4.2.3.4 H_2/O_2 Fuel Cell Fabrication and Characterization

A detailed description of the experiment is described elsewhere.[130] An ink slurry of carbon-supported Pt (20 wt % Pt on Vulcan XC-72, ~ 100 $m^2 g^{-1}$, ElectroChem., Inc.) and Nafion® (5 wt % in water/alcohol, Aldrich) was made by adding the colloidal mixture of Nafion® and butyl acetate drop wise to a suspension of carbon-supported Pt and butyl acetate that have been homogenized at 50 °C for 30 min. The supported Pt catalyst was dispersed in butyl acetate and homogenized at 50 °C for 30 min. The mixture was stirred for 1 h and then painted on a carbon cloth substrate (ETEK, type A plain weave, 0.35 mm thick, 10 wt % wet-proofed). The gas diffusion electrode (GDE) contained 0.75 mg Pt cm^{-2} of catalyst and 20 wt % of Nafion® binder. Smaller 5 cm^2 pieces of the GDE were cut from the larger piece and hot pressed to ETFE-*g*-PSSA membranes at 220 kg cm^{-2} and 150 °C for 90 s. The membrane electrode assembly (MEA) was equilibrated in water at 60 °C for 10 min prior to assembling it in the fuel cell hardware. Gases were delivered to the MEA through a serpentine pattern flow single-cell hardware connected to a test station that had a humidifier/gas flow controller unit (Globetech, Inc.), a load bank (Scribner 890B, Scribner Associates, Inc.) and an FRA (Solartron 1250). FuelCell and Z-plot (Scribner Associates, Inc.) data acquisition

software were used to obtain steady-state polarization curves and ac impedance spectra. The fuel cell was operated at 25 °C and at ambient pressure. The anode and cathode were fully humidified at 40 °C (~95 % RH). Flow rates were set variably at 20 mL min^{-1} A^{-1} in addition to a base flow rate of 30 mL min^{-1}. These flow rates corresponded to variable stoichiometries of 14 – 1.8 for H_2 and 28 – 3.6 for O_2 when the cell is operated at a current density of 0.2 – 1.0 A cm^{-2}. The open circuit potential of the cell was monitored for ~ 30 min. after assembly until the response became stable. Galvanostatic steady state polarization was performed between the potential range of 1.05 and 0.3 V. The cell was equilibrated for 45 s after each current change. Uncompensated resistance, R_u, was measured and compensated using the current interruption technique available in the FuelCell program. This iR_u drop was estimated by interrupting the current and sampling the transient response of potential at 15 – 30 μs after the interruption.

Standard deviation and error propagation were applied to estimate the errors associated with the characterization techniques used.

4.3 Results and Discussion

4.3.1 Incorporation of HEMA into PVDF-*g*-PSSA

Figure 4.5 illustrates the ATR-FTIR spectra for poly(2-hydroxyethyl methacrylate) (poly(HEMA)), PVDF-g-PSSA (1.98), PVDF-*g*-(HEMA-*co*-SSA) and PVDF-*g*-PSSA-*g*-HEMA. The C=O stretch vibration at 1730 cm^{-1} in the modified PVDF-*g*-PSSA confirms the presence of poly(2-hydroxyethyl methacrylate) (poly(HEMA)) in them. Although the ATR-FTIR technique provides chemical composition of the sample to a depth of 0.5 – 2 μm from the surface, poly(HEMA) is

expected to be scattered throughout the polymer film because of the copolymerization technique used. The graft ratio of HEMA in PVDF-*g*-PSSA-*g*- HEMA was estimated to be ~16% from the mass change before and after the addition of HEMA to PVDF-*g*-PSSA; the graft ratio of HEMA in PVDF-g-(HEMA-*co*-SSA) was grossly approximated to be ~ 5% from the intensity ratio at 1730 cm^{-1} and 1400 cm^{-1}. The latter absorption band was attributed to scissor and pendulum oscillations of CH_2 groups in PVDF.

Literature[135] indicates that HEMA hydrolyzes to methacrylic acid and ethylene glycol if it is immersed in an aqueous media for a prolonged period. It is speculated that some hydrolysis may have taken place in the HEMA-modified PVDF-g-PSSAs, particularly in PVDF-*g*-(HEMA-*co*-SSA), because a broad C=O vibrational stretch band is observed. However, as both poly(HEMA) and poly(methacrylic acid) are materials that inherently absorb water,[136] their incorporation into PVDF-*g*-PSSA are expected to help with water transport.

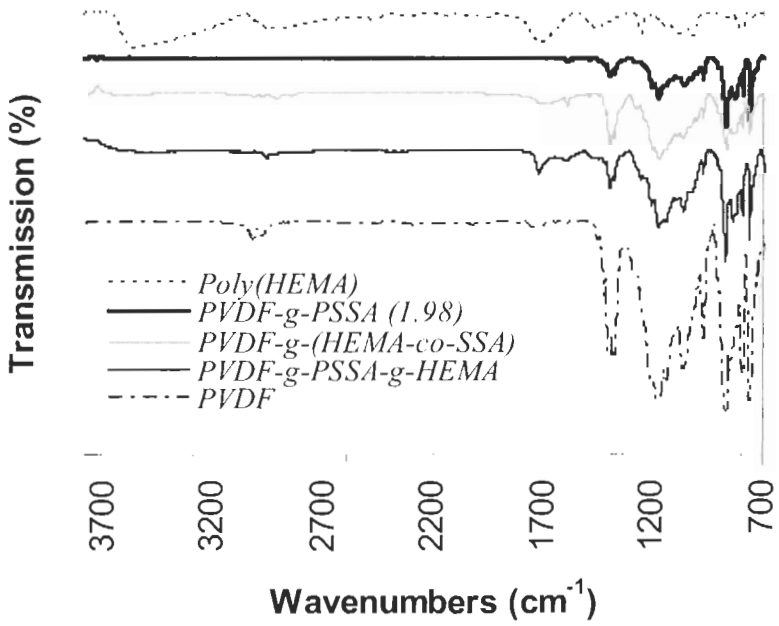

Figure 4.5: ATR-FTIR of poly(HEMA), PVDF-*g*-PSSA (1.98), PVDF-*g*-(HEMA-*co*-SSA), PVDF-*g*-PSSA-*g*-HEMA and PVDF.

4.3.2 Comparison of HEMA-Modified PVDF-*g*-PSSA and Neat PVDF-*g*-PSSA

The general properties of unmodified PVDF-*g*-PSSA, HEMA-modified PVDF-*g*-PSSA and Nafion® are presented in Table 4.1. Water uptake, proton conductivity and λ_{total} of the PVDF-*g*-PSSA decrease when the content of styrenesulfonic acid content in the membrane decreases. The inclusion of HEMA to PVDF-g-PSSA did not appear to alter the properties of PVDF-*g*-(HEMA-*co*-SSA) and PVDF-*g*-PSSA-*g*-HEMA significantly. The small variation in λ_{total} observed between PVDF-*g*-(HEMA-*co*-SSA) and PVDF-*g*-PSSA-*g*-HEMA, was probably due to the slightly higher HEMA content in PVDF-*g*-PSSA-*g*-HEMA.

Table 4.1: General properties for Nafion®, neat PVDF-*g*-PSSA and HEMA-containing PVDF-*g*-PSSA

Sample/ Grafting % (wt %)	IEC (mmol g^{-1})	Water Uptake (wt%)	X_v	λ_{total} (H_2O/SO_3^-)	$\lambda_{freezable}$ (H_2O/SO_3^-)	σ (S cm^{-1})	$P_{H2O,Hydraulic}$ (cm^2 Pa^{-1} s^{-1}) x 10^{12}	$P_{H2O,WVT}$ (cm^2 Pa^{-1} s^{-1}) x 10^{11}
PVDF-*g*-(HEMA-*co*-SSA) (30% HEMA and styrene) ~ 5% HEMA*	1.66	58	0.51	20	6	0.11	0.66	1.47
PVDF-*g*-PSSA-*g*-HEMA (27% styrene and 16% HEMA)	1.63	67	0.48	23	8	0.11	0.417	1.15
PVDF-*g*-PSSA								
9.0	0.32	13	0.18	22	9	0.012	-	-
16.1	1.29	48	0.43	21	8	0.087	0.65	1.21
29.3	1.98	74	0.51	21	10	0.134	-	-
31.1	2.03	83	0.57	23	15	0.142	1.05	1.82
42.9	2.80	146	0.68	29	20	0.169	-	-
44.2	2.80	155	0.68	31	20	0.189	1.66	1.88
N117	0.97	32	0.37	18	9	0.079	0.93	3.95

- determined from ATR-FTIR

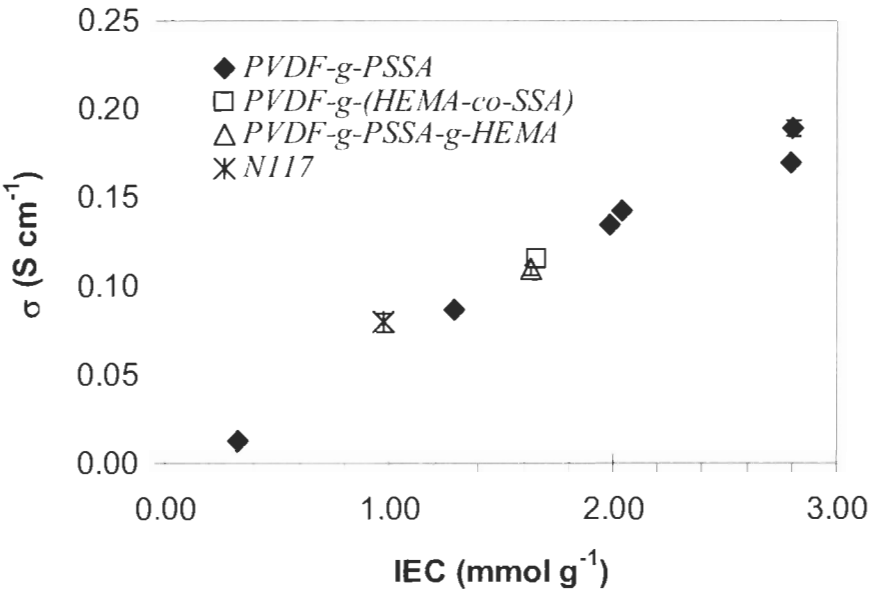

Figure 4.6: **Proton conductivity as a function of ion exchange capacity for PVDF-*g*-PSSA, N117 and HEMA-containing PVDF-*g*-PSSA.**

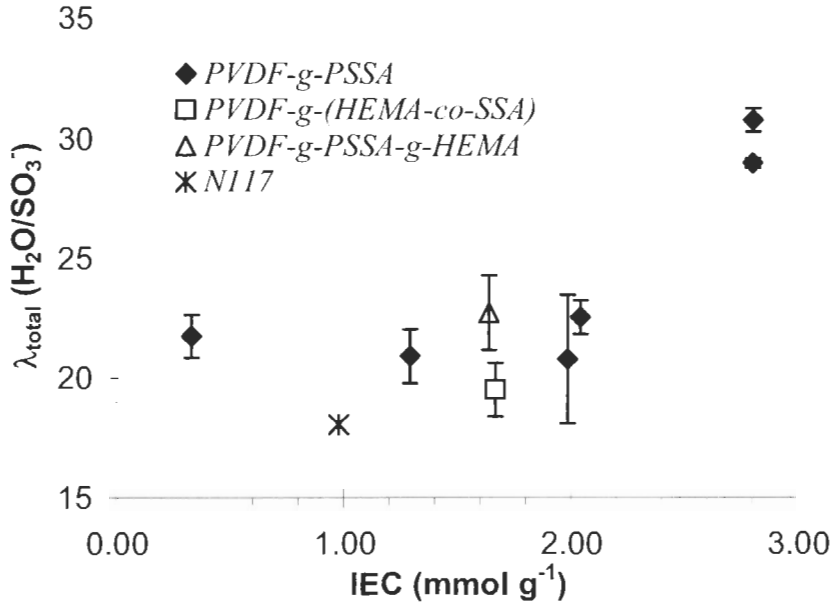

Figure 4.7: **λ_{total} as a function of ion exchange capacity for PVDF-*g*-PSSA, N117 and HEMA-containing PVDF-*g*-PSSA.**

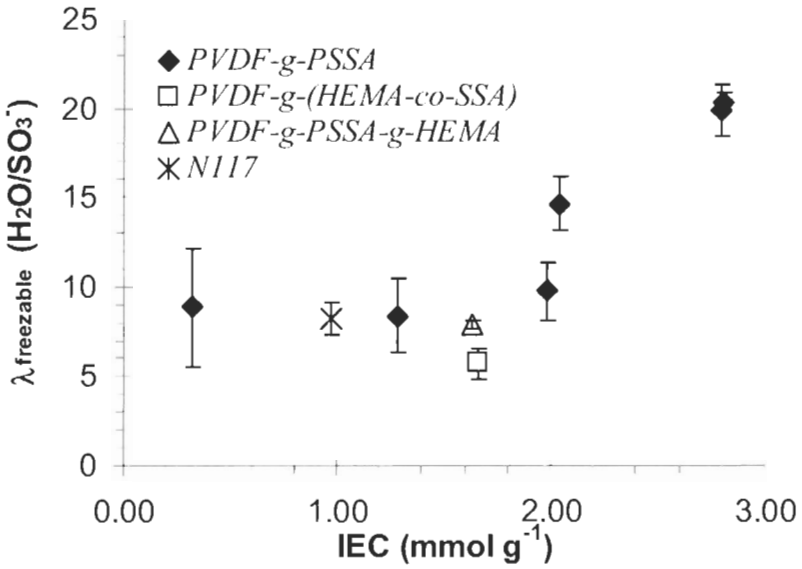

Figure 4.8: Total λ as a function ion-exchange capacity for N117, PVDF-g-PSSA and HEMA-containing PVDF-g-PSSA.

4.3.3 Freezable Water in Water-Saturated Polymer Electrolytes

The nature of water confined within hydrophilic phase of the membrane can vary depending on their interaction with nearby molecules, and discerning them can be difficult in a real system because all the water molecules are interchangeable and represent a continuum of states.[113,137] However, a snap-shot of the local environment of the water molecules can be obtained by systematic freezing of the sample and measuring the temperature at which water in the membrane freezes and the heat flow required for the phase change.[58,59] This method of analysis classifies water as either *freezable* or *nonfreezable*, and they are illustrated in Figure 2.3. Nonfreezable water is defined as water that is strongly bound to either the polymer backbone or the ionic groups and yields no characteristic thermal transition in DSC traces. Freezable water, whether only weakly polarized or liquid-like, exhibits similar thermal transitions to bulk water.

Structural evolution of phase-separated Nafion® using small angle neutron scattering shows that the separated ionic agglomerates at low water content can lead to an inverted phase with an interconnected hydrophilic network in the swollen state.[51] The possibility of phase separation due to incompatible hydrophobic/hydrophilic segments in PVDF-*g*-PSSA membranes has been demonstrated in section 3.3.4. The high proton conductivities measured for hydrated PVDF-*g*-PSSA and HEMA-containing PVDF-*g*-PSSA strongly point to a coalesced ionic cluster network.

Calorimetry data for water-saturated Nafion®, PVDF-*g*-PSSA (1.98 mmol g^{-1}), PVDF-*g*-(HEMA-*co*-SSA) and PVDF-*g*-PSSA-*g*-HEMA are presented in Figure 4.9. Other membranes in the series exhibit similar profiles, but the position and area of the transition varied. The exothermic transitions in the thermograms are attributed to freezing of water within the membrane and the corresponding endothermic transitions are due to melting of frozen water. The late onset of fusion at a lower temperature compared to the melting transitions illustrates the known supercooling phenomenon of water. A single melting transition with melting points between -1.6 and -4.2 °C was detected for hydrated PVDF-*g*-PSSA (IEC = 2.8 - 1.29 mmol g^{-1}), -2.2 °C for Nafion® and -5.1 °C for PVDF-*g*-(HEMA-*co*-SSA). Two melting transitions were detected for PVDF-*g*-PSSA-*g*-HEMA, one at –1.98 °C and the other at -0.79 °C. The latter may correspond to a water-containing, HEMA only compartment in the membrane.

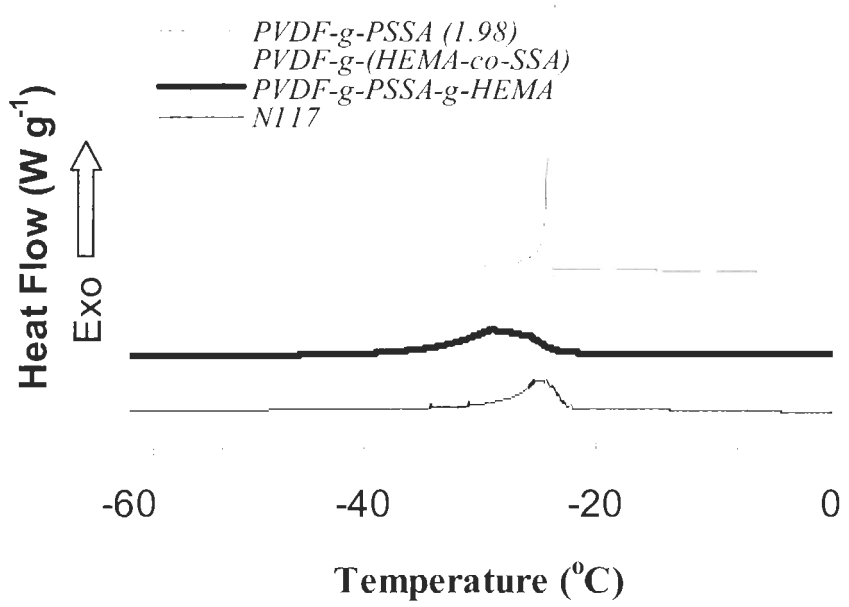

(a)

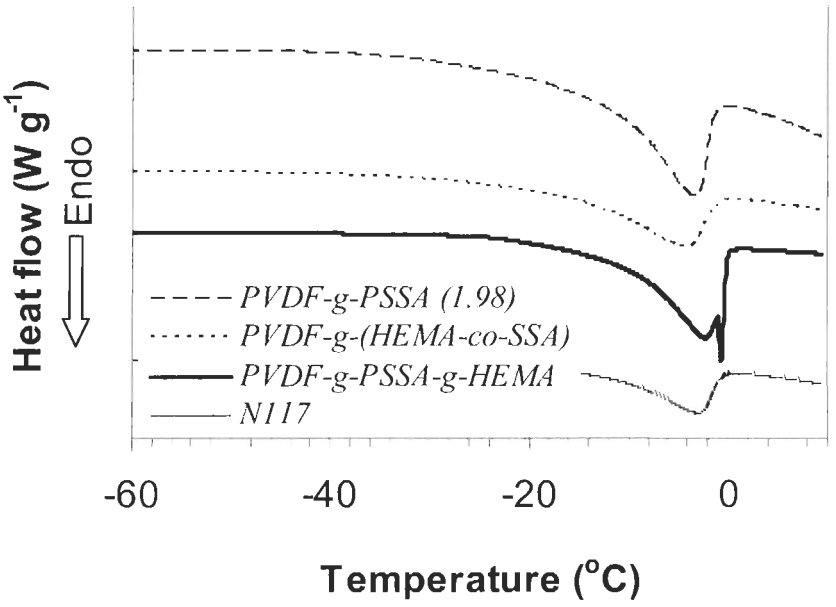

(b)

Figure 4.9: **(a) Cooling and (b) Heating DSC thermograms for water saturated PVDF-*g*-PSSA (1.98), PVDF-*g*-(HEMA-*co*-SSA), PVDF-*g*-PSSA-*g*-HEMA and N117.**

Integrating the area under the peak corresponding to freezing of water at ~ -23 °C provides a quantitative measure of "freezable/unbound" water in water-swollen membranes. Biological and polymer gel studies show that the property of the water molecules can vary depending on their interaction with the material[66] and their distance from the pore wall or polarized group. Modeling studies of Nafion® show that the permittivity of water in Nafion® is bulk-like near the pore center but decreases with decreasing radial distance from the pore wall in which the SO_3^- groups are situated in Nafion®.[63,91] Table 4.1 illustrates the change in $\lambda_{freezable}$ for the membranes. It is interesting to note that $\lambda_{freezable}$ accounts for approximately 40 – 70 % of the total water in PVDF-g-PSSA and approximately 50% of the total water in Nafion®. The content of free water estimated by pore permittivity calculations accounts for approximately 50 % of the total water in a fully hydrated Nafion® pore, which is in close agreement with the fraction of freezable water for water-saturated Nafion® membranes measured by DSC.[113] Modelling work by Pintauro and co-workers[67] and Paddison and co-workers[63,23] showed that the permittivity of this water is similar to bulk water (within < 10 %) so that water that freezes may be defined as *free water*.

The change of $\lambda_{freezable}$ with IEC for PVDF-*g*-PSSA, N117, PVDF-*g*-PSSA-*g*-HEMA and PVDF-*g*-(HEMA-*co*-SSA) are illustrated in Figure 4.10. The concominant decrease of $\lambda_{freezable}$ with IEC is expected because reducing the number of hygroscopic units in the polymer reduces the tendency for the membrane to swell. Although incorporating polar absorbing segments to PVDF-g-PSSA should theoretically yield polymers that can take up more water, the lack of variation in $\lambda_{freezable}$ between the modified and unmodified PVDF-*g*-PSSA of the same IEC, even through λ_{total} in PVDF-

g-PSSA-*g*-HEMA is slightly larger, strongly implies that that the excess water is perhaps strongly "bound" to the HEMA or to the polymer. Cross-linking induced by re-irradiation of PVDF-*g*-PSSA-*g*-HEMA may have also contributed to the reduced swelling capacity of the membrane and, therefore, less free water is present in the membrane. In the case of PVDF-*g*-(HEMA-*co*-SSA), displaced free volume due to the presence of poly(HEMA) within the ionic pore may explain the lower $\lambda_{freezable}$ observed. The influence of poly(HEMA) on water transport and on fuel cell performances will be examined in the sections below.

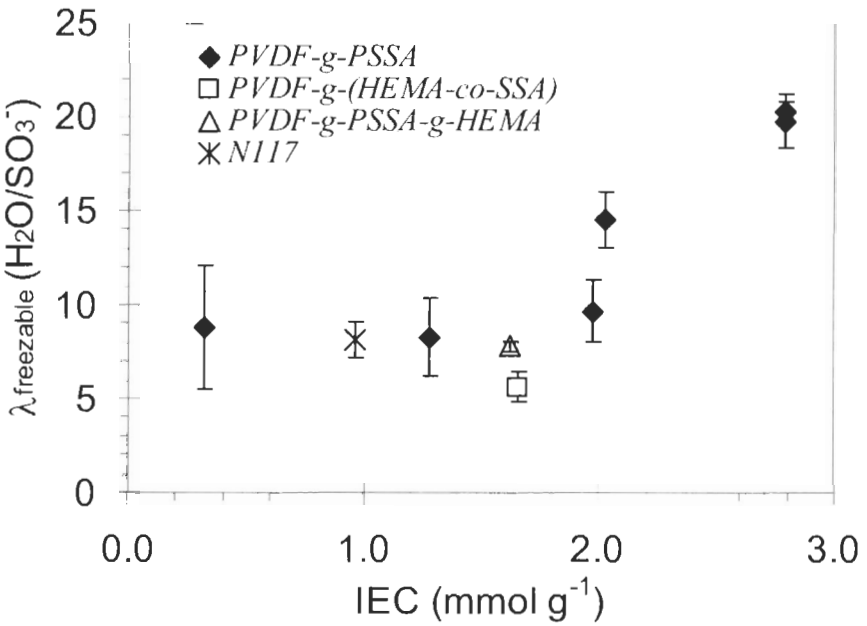

Figure 4.10: $\lambda_{freezable}$ as a function of IEC for water-saturated Nafion®, PVDF-*g*-PSSA and HEMA-containing PVDF-*g*-PSSA membranes.

4.3.4 Hydraulic Permeabilities of Water-Saturated Nafion®, PVDF-*g*-PSSA and HEMA-Containing PVDF-*g*-PSSA

Hydraulic permeability is a membrane property that depends strongly on the size, type and viscosity of the fluidic region. Since a larger $\lambda_{freezable}$ value is indicative of more

free volume in the hydrophilic phase of the polymer, the proportional increase of $P_{H2O,hydraulic}$ with $\lambda_{freezable}$ for PVDF-g-PSSA in Figure 4.11 is justified. Even though water transport should be different for the different polymer system because their morphology, tortuosity and interaction of the water/polymer phase are different, no noticeable change in $P_{H2O,hydraulic}$ was found between N117, PVDF-g-PSSA and modified PVDF-g-PSSA with the same IEC. The introduction of HEMA has not appeared to produce the alternative water transporting channels in PVDF-*g*-PSSA-*g*-HEMA; however, its applicability has not been fully explored as the effect of a higher HEMA graft content on water transport still needs to be studied.

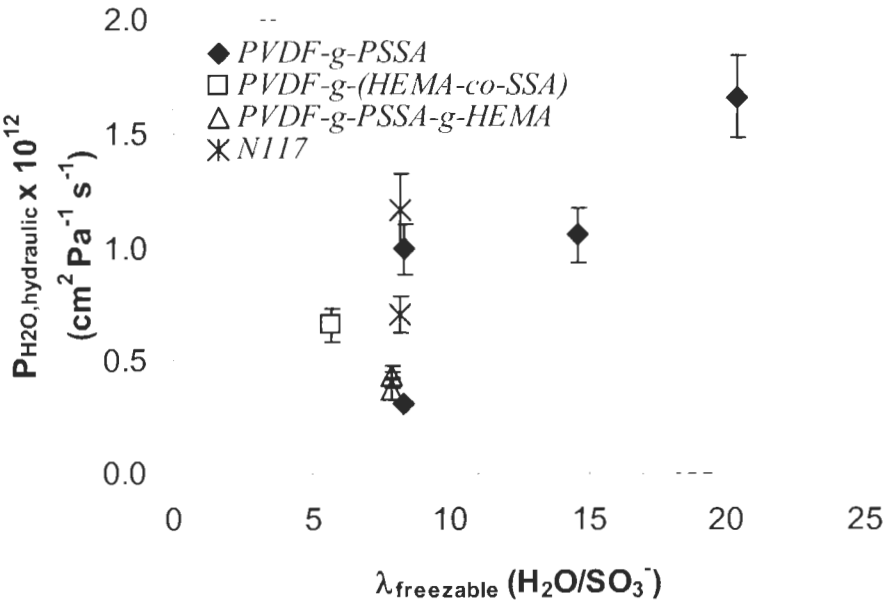

Figure 4.11: Hydraulic permeability of water through water-saturated PVDF-*g*-PSSA, HEMA-containing PVDF-*g*-PSSA and N117 membranes as a function $\lambda_{freezable}$.

4.3.5 Influence of HEMA on Fuel Cell Performance.

The influence of HEMA in PEM on fuel cell performance is presented in Figure 4.12. The polarization profiles were iR corrected in order to eliminate the effect of

membrane thickness. Preliminary work shows that fuel cells employing PVDF-*g*-PSSA incorporated with HEMA exhibits better performance than neat ETFE-*g*-PSSA membranes of similar IEC. However, the adhesion of membrane to electrode has to be further investigated in order to evaluate whether inconsistency in performance between samples is related to incompatibility and resistance at the membrane and electrode interface. A Ph.D. student is currently pursuing this work at SFU.

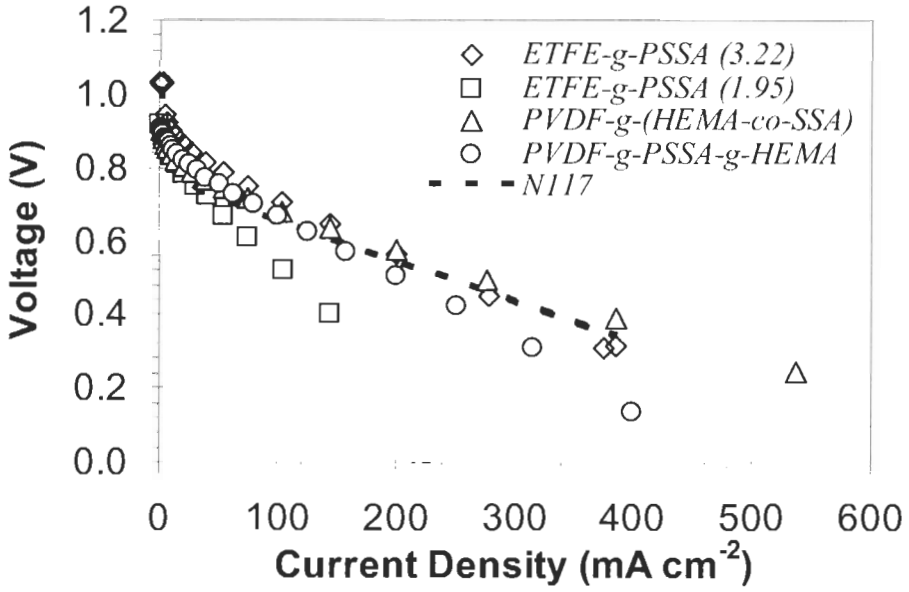

Figure 4.12: H_2/O_2 polarization of Nafion® (dashed lines), HEMA-containing membranes (grey symbols) and ETFE-*g*-PSSA (open symbols) at ambient pressure. The fuel cell was operated at 25 °C and at ambient pressure. Gases supplied were humidified at 40 °C (~ 95% RH). Flow rates were set variable at 20 mL min^{-1} A^{-1} in addition to the base flow rate of 30 mL min^{-1} A^{-1} to give a variable stoichiometry of 14 – 1.8 for H_2 and 28 – 3.6 for O_2 for current densities of 0.2 – 1.0 A cm^{-2}. Anode and cathode GDEs contained 0.75 mg Pt cm^{-2} and 20 wt % Nafion®.

It is understood that unmodified PVDF-g-PSSA would have been a more appropriate comparison, no data was available at the time the thesis was produced. Earlier studies by Chuy indicate that negligible differences exist between ETFE-*g*-PSSA

and PVDF-*g*-PSSA membranes so the results are not expected to deviate significantly from the current trends.[138]

4.3.6 Water Vapour Transport

Hydrogen gas supplied to the anode is often humidified at a higher temperature than the cell temperature in order to provide more moisture to the anode. The moisture provided, however, does not always offset the loss due to electro-osmosis[130] at higher current densities. Water concentration differences between the cathode and the anode interfaces is a major driving force for the back-transport of water. This parameter was estimated by measuring how transport of vapour pressure down a pressure gradient from 100% RH to 40% RH changes between samples. The results are illustrated in Figure 4.13. The vapour transport permeability (or $P_{H2O,VWT}$) decreases when the volume fraction of freezable water decreases, possibly due to a decreasing pore diameter dimension. The results also indicate that incorporating HEMA to PVDF-*g*-PSSA does not give PVDF-*g*-PSSA of similar freezable water volume significantly different $P_{H2O,VWT}$ behaviour; however, it is interesting that $P_{H2O,VWT}$ of Nafion® is at least three times higher compared to the two polymer types. The much higher $P_{H2O,WVT}$ value in Nafion® relative to PVDF-*g*-PSSA and modified PVDF-*g*-PSSA suggests that Nafion® is a good water transport material, a characteristic that is perhaps related to a combination of its well-defined ionic pores, and nature of the hydrophilic phase in the polymer.[49,67] The high electro-osmotic drag values reported for Nafion® (i.e., 2.5 – 4 H_2O/H^+)[35,49,94] imply that water in the membrane is transported easily in the forward direction (i.e., towards the cathode). However, since a fuel cell with Nafion® still exhibits good performance despite its high water flux to the cathode due to electro-osmosis, the

backward flow of water to the anode is probably equally as high in order to curb dehydration at the anode, and to yield reliable performances. Electro-osmotic drag measurements reported in the literature of membranes containing cross-linked poly(styrenesulfonic) acid in polypropylene support with IEC of 2.2 mmol SO_3^- g^{-1} (which is to some extend similar to the radiation grafted system) are ~ 2 H_2O/H^+ for a hydrate membrane,[35] a value that is slightly lower than Nafion®. More understanding is required, particularly on the topic of electro-osmosis and water transport during fuel cell operation.

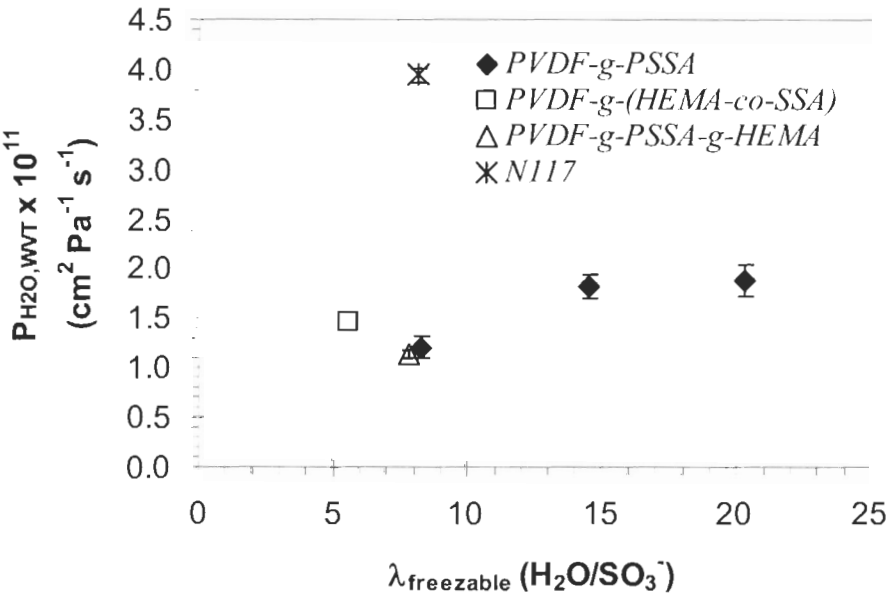

Figure 4.13: Water vapour transport permeability of PVDF-*g*-PSSA, HEMA-containing PVDF-*g*-PSSA and Nafion® as a function of $\lambda_{freezable}$.

4.4 Conclusions

The membrane in a PEMFC requires a proper level of hydration (maintained either by or in combination with gas humidification, water concentration gradient, implementation of inorganic solids inside the membrane, pressure gradient, or use of

thinner membranes) in order to sustain adequate membrane proton conduction. Each of the methods has a set of drawbacks. For instance, the use of gas humidification adds parasitic loses to the cell, the use of pressure gradient and thinner membranes risk gas crossover and membrane pin-hole formation, and the use of a water concentration gradient to transport water to the anode needs better membrane design. Ultimately, designs that decrease the complexity and size of the overall system is desired from an engineering standpoint. For this reason, designs that encourage back-transport of water or that is able to keep the anode hydrated without implementing means that consume additional power are desirable.

Water-absorbing polar non-ionic poly(2-hydroethylmethacrylate) (poly(HEMA)) was incorporated into poly(vinyledene difluoride)-grafted-poly(styrenesulfonic) acid (PVDF-*g*-PSSA) membranes by (1) copolymerization of 2-hydroethylmethacrylate (HEMA) and styrene, to afford PVDF-*g*-(HEMA-*co*-SSA), and by (2) post-irradiation grafting of PVDF-*g*-PSSA to afford PVDF-*g*-PSSA-*g*-HEMA in which the HEMA phase is randomly grafted into PVDF-*g*-PSSA. The bands at 1730 cm^{-1} corresponding to C=O stretch confirm the presence of HEMA in both membranes. Water uptake, conductivity, λ_{total} and water permeability studies of HEMA containing membranes do not appear to deviate significantly from unmodified PVDF-*g*-PSSA. A better understanding in MEA fabrication and electrode/membrane compatibility is needed before polarization curves can be interpreted. A wider HEMA composition is also required to assess whether the incorporation of polar, non-ionic polymer segments can enhance water transport properties of PEMs.

CHAPTER 5: SUMMARY AND FUTURE WORK

The nature of the interaction between water and covalently bound acid groups in the ionic phase of proton exchange membranes (PEMs) was studied using low temperature differential scanning calorimetry in five classes of polymers:

- Polyacrylonitrile-*graft*-poly(styrene sulfonic) acid (PAN-*g*-*mac*PSSA),
- Poly(vinylidene difluoride)-*graft*-poly(styrenesulfonic) acid (PVDF-*g*-PSSA),
- Poly(ethylenetetrafluoroethylene)-*graft*-with poly(styrenesulfonic) acid (ETFE-*g*-PSSA),
- PVDF-g-PSSA with hydroxyethylmethacrylate (HEMA), and
- Perfluorosulfonic acid membrane (Nafion®)

Results indicated two distinct water types: Freezable water or water molecules that exhibited a crystallization peak in the DSC thermogram at sub-zero conditions, and non-freezable water or water that did not crystallized at sub-zero temperatures. Freezable water accounted for approximately 50% of the total water in water-saturated Nafion®, 40 – 70 % of the total water in water-saturated PVDF-*g*-PSSA, ETFE-*g*-PSSA and PVDF-g-PSSA with hydroxyethylmethacrylate (HEMA), and 0 – 50 % of the total water in water-saturated PAN-*g*-*mac*PSSA. The experimental results for Nafion® were in agreement with theoretical pore permitivity calculations of water-saturated Nafion®.

Two types of temperature-dependence conductivity plots were obtained upon decreasing the temperature of ETFE-*g*-PSSA and Nafion® membranes to below 0 °C. One plot type showed a membrane in which free water (i.e., > 85% RH) was present, while the other type showed a membranes in which no free water was present (< 85 %

RH). In the former case, three conductivity regions were observed: (1) a region corresponding to proton conduction above the freezing point of water, (2) a region in which the freezing process is taking place, and (3) a region in which free water had crystallized. The activation energies for proton transport were ~ 0.15 and 0.4 - 0.5 eV for above and below freezing of water, respectively. In the latter case when no free water is present, no break in the slope was observed. The activation energy for proton transport in this environment was ~ 0.25 eV.

The much higher proton conduction in membranes with free water demonstrates that the presence of free water is important for attaining high proton conducty above 0 °C due to the increased mobility of protons in free water. However, the ability of non-freezable water to facilitate the transport of protons suggests that significant proton conductivity may be obtained from membranes with low water content if the membranes are optimized to yield a continuous proton conductive pathway. Non-freezable λ, extrapolated from the intercept of plots of total λ *versus* freezable λ, and from gravimetric analysis, reveal that ~ 5 – 14 H_2O per ionic group do not freeze. In PEMFC applications that require sub-zero temperature start up, this work has confirmed that "frozen" membranes are still able to transport protons. As liquid water need not be present to obtain reasonable conductivity, this also has implications in the design of membranes that are required to operate above 100 °C.

Results of microstructurally controlled PAN-*g*-*mac*PSSA membranes indicate that the water content, proton conductivity, and methanol permeability of these particular class of membranes do not depend on the length of the acid grafts. Methanol permeability studies of PAN-*g*-*mac*PSSA and PVDF-*g*-PSSA indicated that these

poly(styrenesulfonic) acid grafted polymers are good methanol barriers compared to Nafion® benchmark. Increasing proton conductivity of PAN-*g*-*mac*PSSA and PVDF-*g*-PSSA membranes by increasing the density of hydrophilic pendant units (i.e., increasing the IEC) also increased the permeability of methanol due to a simultaneous increase in free water content and a corresponding enhancement of hydrophilic domain network. Differences in permeability trends found for the different polymer classes with the same content of free water have been explained on the basis of tortuosity and interaction of methanol in the ionic network. The association of water with the polymer backbone in PAN-*g*-*mac*PSSA is a new finding for proton conducting membranes, but appears to have minimal effect on the permeability of the membrane.

Noting that reasonable proton conductivity can be obtained from percolated polymer electrolyte systems that contain primarily non-freezable water, we speculate that an even lower methanol permeability can be obtained from a membrane system that contains only non-freezable water. However, the styrenic systems studied here showed poor conductivity (i.e., < 0.003 S cm^{-1}) in the absence of freezable water (i.e., for low IEC membranes) possibly due to the absence of a well-defined continuous ionic network. More understanding is needed in this area in order to develop membranes that possess continuous pore structures containing only non-freezable water.

The effect of introducing polar, non-ionic grafts to PVDF-*g*-PSSA to improve its water transport was investigated. Water-absorbing, polar, non-ionic poly(2-hydroethylmethacrylate) (poly(HEMA)) was incorporated into PVDF-*g*-PSSA membranes (1) by copolymerization of 2-hydroethylmethacrylate (HEMA) and styrene, to produce PVDF-*g*-(HEMA-*co*-SSA), and (2) by post-irradiation grafting of PVDF-*g*-

PSSA to afford PVDF-*g*-PSSA-*g*-HEMA in which the HEMA phase is randomly grafted in PVDF-*g*-PSSA. Attenuated total reflectance infrared spectra confirmed the presence of HEMA in the PVDF-*g*-PSSA. Water uptake, conductivity and λ_{total} of HEMA containing membranes did not appear to deviate significantly from neat PVDF-*g*-PSSA trends. Findings also indicated negligible improvements on hydraulic and water vapour transport permeabilities in the modified polymers. More understanding is needed, particularly on the effects of electro-osmosis on membrane water transport and resistance during fuel cell operation.

BIBLIOGRAPHY

1. International Energy Annual (EIA). *Official Energy Statistics from the U.S.government*. 2003. (http://www.eia.doe.gov).
2. Zegers, P. *Journal of Power Sources* **2006**, *154*, 497-502.
3. Sachs, G. Dreaming with BRICs: The Path to 2050. *Global Economics Paper No. 99*, 2003.
4. Into Deep water. *The Economist*, **2001**, *August 21*, p 17.
5. Ramani, V. Fuel Cells. *The Electrochemical Society Interface* **2006**, *Spring*, 41-44.
6. Vielstich, W.; Lamm, A.; Gasteiger, H. A. *Handbook of Fuel Cells: Fundamentals Technology and Applications*, John Wiley & Sons, Ltd.: Chichester, UK, 2003.
7. Hickner, M. A. Transport and Structure in Fuel Cell Proton Exchange Membranes. *Dissertation*. Virginia Polytechnic Institute and State University, VA, USA, 2003.
8. Carrette L.; Friedrich K.A.; and Stimming U. *ChemPhysChem* **2000**, *1*(4), 162-193.
9. Costamagna, P.; Srinivasan, S. *Journal of Power Sources* **2001**, *102*, 253-269.
10. Carle, G.; Axhausen, K. W.; Wokaun, A.; Keller, P. *Transport Reviews* **2005**, *25*, 739-760.
11. Eikerling, M. *Journal of the Electrochemical Society* **2006**, *153*, E58-E70.
12. Song, D. T.; Wang, Q. P.; Liu, Z. S.; Eikerling, M.; Xie, Z.; Navessin, T.; Holdcroft, S. *Electrochimica Acta* **2005**, *50*, 3347-3358.
13. Wilson, M. S.; Valerio, J. A.; Gottesfeld, S. *Electrochimica Acta* **1995**, *40*, 355-363.
14. Chun, William; Narayanan, Sekharipuram R.; Jeffries-Nakamura, Barbara; Valdez, Thomas I.; Linke, Juergen. Direct deposit of catalyst on the membrane of direct-feed fuel cells. California Institute of Technology, WO, USA.1999; US Patent 9939841.
15. Wilson, M. S.; Gottesfeld, S. *Journal of the Electrochemical Society* **1992**, *139*, L28-L30.
16. Easton, E. B.; Astill, T. D.; Holdcroft, S. *Journal of the Electrochemical Society* **2005**, *152*, A752-A758.

17. Hickner, M. A.; Ghassemi, H.; Kim, Y. S.; Einsla, B. R.; McGrath, J. E. *Chemical Reviews* **2004**, *104*, 4587-4611.

18. Yang, Y.; Holdcroft, S. *Fuel Cells* **2005**, *5*, 171-186.

19. Mauritz, K. A.; Moore, R. B. *Chemical Review* **2004**, *104*, 4535-4585.

20. Stewart, R. *The Proton: Aplications to Organic Chemistry*, Academic Press: Orlando, Florida, 1985; 134-207.

21. Paddison, S. J. *Journal of New Materials for Electrochemical Systems* **2001**, *4*, 197-207.

22. Roudgar, A, Narasimachary, S. P., and Eikerling, M. *Journal of Physical Chemistry B* **2006**, *111*(41), 20469-20477.

23. Paddison, S. J. *Annual Review of Materials Research* **2003**, *33*, 289-319.

24. Zawodzinski, T. A.; Derouin, C.; Razinski, S.; Sherman, R. J.; Smith, V. T.; Springer, T. E.; Gottesfeld, S. *Journal of the Electrochemical Society* **1993**, *140*, 1041-1047.

25. Pivovar, A. A.; Pivovar, B. S. *Journal of Physical Chemistry B* **2005**, *109*, 785-793.

26. Atkins, P. *Physical Chemistry*; 6th Ed.; Oxford University Press: Oxford, UK, 1999; Chapter 29, pp. 877-903.

27. Navessin, T. Influence of the Membrane Ion Exchange Capacity on the Catalyst Layer of Proton Exchange Membrane Fuel Cell. *Dissertation*. Simon Fraser University, BC, Canada, 2004.

28. Norskov, J. K.; Rossmeisl, J.; Logadottir, A.; Lindqvist, L.; Kitchin, J. R.; Bligaard, T.; Jonsson, H. *Journal of Physical Chemistry B* **2004**, *108*, 17886-17892.

29. Yeager, E. *Electrochimica Acta* **1984**, *29*, 1527-1537.

30. Andreaus, B.; Scherer, G. G. *Solid State Ionics* **2004**, *168*, 311-320.

31. Andrews, Craig. Gas and water management for a fuel cell system. USA. 2003; US Patent 2004121218.

32. Defilippis, Michael S., Brown, Eric J., Kim, Hongsun, and Neutzler, Jay K. Method and apparatus for water management of a fuel cell system. USA. 2003, US Patent 2003215686.

33. Eikerling, M.; Kharkats, Y.; Kornyshev, A. A.; Volfkovich, Y. *Journal of the Electrochemical Society* **1998**, *145*, 2684-2699.

34. Slee, R.; Jones, P.; Lakeman, B.; Moore, J. *Proceedings of the Power Sources Conference* **2000**, *39th*, 148-151.

35. Pivovar, B. S.; Smyrl, W. H.; Cussler, E. L. *Journal of the Electrochemical Society* **2005**, *152*, A53-A60.

36. Pivovar, B. S. *Polymer* **2006**, *47*, 4194-4202.

37. Janssen, G. J. M.; Overvelde, M. L. J. *Journal of Power Sources* **2001**, *101*, 117-125.

38. Meier, F.; Eigenberger, G. *Electrochimica Acta* **2004**, *49*, 1731-1742.

39. Nguyen, T. V.; White, R. E. *Journal of the Electrochemical Society* **1993**, *140*, 2178-2186.

40. Comparison of Alternate Fuels. US Deparment of Energy - *Energy Efficiency and Renewable Energy* 2005, *2/3* (http://www.eere.energy.gov/afdc/altfuel/fuel_properties.html).

41. Bossel, U. Well-to-Wheel Studies, Heating Values, and the Energy Conservation Principle. *European Fuel Cell Forum* 2003, Oct. 29 (http://www.efcf.com).

42. Geologic Carbon Dioxide Sequestration Research. *Department of Energy* 2005, *11/6*.

43. Is Hydrogen Dangerous? *Rockie Mountain Institute* 2006 (http://www.rmi.org/sitepages/pid536.php)

44. da Rosa, A. V. *Fundamentals of Renewable Energy Processes*, Elsevier Academic Press: Burlington, MA, USA, 2005.

45. Pivovar, B. Electrochemical Selectivity and Electro-osmosis in Direct Methanol Fuel Cell Electrolytes. *Dissertation*. University of Minnesota, MN, USA, 2000.

46. Lin, J.; Lee, J. K.; Wycisk, R.; Pintauro, P. N. *Abstracts of Papers of the American Chemical Society* **2005**, *230*, U1636-U1637.

47. Gasteiger, H. A.; Panels, J. E.; Yan, S. G. *Journal of Power Sources* **2004**, *127*, 162-171.

48. Gerbis, M. Clean Energy: An Untapped Source of Energy Pollution Prevention. 2004 (http://www.c2p2online.com/documents/Mike_Gerbis.pdf).

49. Hickner, M. A.; Pivovar, B. S. *Fuel Cells* **2005**, *5*, 213-229.

50. Kim, Y. S.; Einsla, B.; Sankir, M.; Harrison, W.; Pivovar, B. S. *Polymer* **2006**, *47*, 4026-4035.

51. Gebel, G. *Polymer* **2000**, *41*, 5829-5838.

52. Kim, Y. S.; Dong, L. M.; Hickner, M. A.; Glass, T. E.; Webb, V.; McGrath, J. E. *Macromolecules* **2003**, *36*, 6281-6285.

53. Paddison, S. J. *Annual Review of Materials Research* **2003**, *33*, 289-319.

54. Anantaraman, A. V.; Gardner, C. L. *Journal of Electroanalytical Chemistry* **1996**, *414*, 115-120.

55. Kreuer, K. D. *Solid State Ionics* **1997**, *94*, 55-62.

56. Clayden, N. J.; Esposito, S.; Pernice, P.; Aronne, A. *Journal of Materials Chemistry* **2002**, *12*, 3746-3753.

57. Zawodzinski, T. A., Jr.; Neeman, M.; Sillerud, L. O.; Gottesfeld, S. *Journal of Physical Chemistry* **1991**, *95*, 6040-6044.

58. Wolfe, J.; Bryant, G.; Koster, K. L. *Cryoletters* **2002**, *23*, 157-166.

59. Buch, V.; Devlin, J.P. *Water in Confining Geometries*, Springer: New York, USA, 2003.

60. Slade, S.; Campbell, S. A.; Ralph, T. R.; Walsh, F. C. *Journal of the Electrochemical Society* **2002**, *149*, A1556-A1564.

61. Eikerling, M.; Kornyshev, A. A.; Kuznetsov, A. M.; Ulstrup, J.; Walbran, S. *Journal of Physical Chemistry B* **2001**, *105*, 3646-3662.

62. Kreuer, K. D.; Dippel, T.; Meyer, W.; Maier, J. *Materials Research Society Symposium Proceedings* **1993**, *293*, 273-282.

63. Paddison, S. J.; Paul, R. *Physical Chemistry Chemical Physics* **2002**, *4*, 1158-1163.

64. Okada, T. *Journal of Physical Chemistry B* **2002**, *106*, 1267-1273.

65. Okada, T.; Nakamura, N.; Yuasa, M.; Sekine, I. *Journal of the Electrochemical Society* **1997**, *144*, 2744-2750.

66. Rowland, S. P. *Water in Polymers*, American Chemical Society, Washington, D.C., USA, 1979.

67. Bontha, J. R.; Pintauro, P. N. *Chemical Engineering Science* **1994**, *49*, 3835-3851.

68. Yang, Y.; Pintauro, P. N. *Industrial & Engineering Chemistry Research* **2004**, *43*, 2957-2965.

69. Eikerling, M.; Kornyshev, A. A.; Kuznetsov, A. M.; Ulstrup, J.; Walbran, S. *Journal of Physical Chemistry B* **2001**, *105*, 3646-3662.

70. Walbran, S.; Kornyshev, A. A. *Journal of Chemical Physics* **2001**, *114*, 10039-10048.

71. Gebel, G.; Atkins, P. *Polymer* **2000**, *41*, 5829-5838.

72. Gupta, B.; Haas, O.; Scherer, G. G. *Journal of Applied Polymer Science* **1995**, *57*, 855-862.

73. Hietala, S.; Holmberg, S.; Nasman, J.; Ostrovskii, D.; Paronen, M.; Serimaa, R.; Sundholm, F.; Torell, L.; Otrkkeli, M. *Die Angewandte Makromolekulare Chemie* **1997**, *253*, 151-167.

74. Paddison, S. J.; Bender, G.; Kreuer, K. D.; Nicoloso, N.; Zawodzinski, T. A., Jr. *Journal of New Materials for Electrochemical Systems* **2000**, *3*, 291-300.

75. Laporta, M.; Pegoraro, M.; Zanderighi, L. *Physical Chemistry Chemical Physics* **1999**, *1*, 4619-4628.

76. Nagura, M.; Saitoh, H.; Gotoh, Y.; Ohkoshi, Y. *Polymer* **1996**, *37*, 5649-5652.

77. Cappadonia, M.; Erning, J. W.; Stimming, U. *Journal of Electroanalytical Chemistry* **1994**, *376*, 189-193.

78. Uosaki, K.; Okazaki, K.; Kita, H. *Journal of Electroanalytical Chemistry* **1990**, *287*, 163-169.

79. Alberti, G.; Casciola, M.; Massinelli, L.; Bauer, B. *Journal of Membrane Science* **2001**, *185*, 73-81.

80. Savinell, R.; Yeager, E.; Tryk, D.; Landau, U.; Wainright, J.; Weng, D.; Lux, K.; Litt, M.; Rogers, C. *Journal of the Electrochemical Society* **1994**, *141*, L46-L48.

81. Chuy, C.; Basura, V. I.; Simon, E.; Holdcroft, S.; Horsfall, J.; Lovell, K. V. *Journal of the Electrochemical Society* **2000**, *147*, 4453-4458.

82. Beattie, P. D.; Orfino, F. P.; Basura, V. I.; Zychowska, K.; Ding, J.; Chuy, C.; Schmeisser, J.; Holdcroft, S. *Journal of Electroanalytical Chemistry* **2001**, *503*, 45-56.

83. Cappadonia, M.; Erning, J. W.; Niaki, S. M. S.; Stimming, U. *Solid State Ionics* **1995** , *77*, 65-69.

84. Horne R. A.; Frysinger, G. R.; MYERS, B. R. *Journal of Chemical Physics* **1963**, *39*, 2666-2673.

85. Cowin, J. P.; Tsekouras, A. A.; Iedema, M. J.; Wu, K.; Ellison, G. B. *Letters to Nature* **1999**, *398*, 405-407.

86. Colomban P.; Novak, A. *Proton Conductors: Solids, Membranes and Gels - Materials and Devices*; Cambridge University Press: Cambridge, 1992; Chapter 3, pp. 38-60.

87. Pang, X. F. *European Physical Journal B* **2006**, *49*, 5-23.

88. Atkins, J. R.; Sides, C. R.; Creager, S. E.; Harris, J. L.; Pennington, W. T.; Thomas, B. H.; DesMarteau, D. D. *Jounal of New Materials for Electrochemical Systems* **2003**, *6*, 9-15.

89. Sumner, M. J.; Harrison, W. L.; Weyers, R. M.; Kim, Y. S.; McGrath, J. E.; Riffle, J. S.; Brink, A.; Brink, M. H. *Journal of Membrane Science* **2004**, *239*, 199-211.

90. Kim, Y. S.; Dong, L.; Hickner, M. A.; Pivovar, B. S.; McGrath, J. E. *Polymer* **2003**, *44*, 5729-5736.

91. Paul, R.; Paddison, S. J. *Solid State Ionics* **2004**, *168*, 245-248.

92. Atkins P. *Physical Chemistry*; 6th Ed.; Oxford University Press: Oxford, UK, 1999; Chapter 24, pp. 723-760.

93. Saito, M.; Arimura, N.; Hayamizu, K.; Okada, T. *Journal of Physical Chemistry B* **2004**, *108*, 16064-16070.

94. Kreuer, K. D.; Paddison, S. J.; Spohr, E.; Schuster, M. *Chemical Reviews* **2004**, *104*, 4637-4678.

95. Easton, E. B.; Langsdorf, B. L.; Hughes, J. A.; Sultan, J.; Qi, Z. G.; Kaufman, A.; Pickup, P. G. *Journal of the Electrochemical Society* **2003**, *150*, C735-C739.

96. Nunes, S. P.; Ruffmann, B.; Rikowski, E.; Vetter, S.; Richau, K. *Journal of Membrane Science* **2002**, *203*, 215-225.

97. Zhang, G. W.; Zhou, Z. T. *Journal of Membrane Science* **2005**, *261*, 107-113.

98. Smitha, B.; Sridhar, S.; Khan, A. A. *Journal of Membrane Science* **2005**, *259*, 10-26.

99. Einsla, B. R.; Kim, Y. S.; Hickner, M. A.; Hong, Y. T.; Hill, M. L.; Pivovar, B. S.; McGrath, J. E. *Journal of Membrane Science* **2005**, *255*, 141-148.

100. Besse, S.; Capron, P.; Diat, O.; Gebel, G.; Jousse, F.; Marsacq, D.; Pineri, M.; Marestin, C.; Mercier, R. *Journal of New Materials for Electrochemical Systems* **2002**, *5*, 109-112.

101. Kreuer, K. D.; Ise, M.; Fuchs, A.; Maier, J. *Journal de Physique IV* **2000**, *10*, 279-281.

102. Woo, Y.; Oh, S. Y.; Kang, Y. S.; Jung, B. *Journal of Membrane Science* **2003**, *220*, 31-45.

103. Chuy, C.; Ding, J. F.; Swanson, E.; Holdcroft, S.; Horsfall, J.; Lovell, K. V. *Journal of the Electrochemical Society* **2003**, *150*, E271-E279.

104. Shen, M.; Roy, S.; Kuhlmann, J. W.; Scott, K.; Lovell, K.; Horsfall, J. A. *Journal of Membrane Science* **2005**, *251*, 121-130.

105. Tricoli, V. *Journal of the Electrochemical Society* **1998**, *145*, 3798-3801.

106. Zawodzinski, T. A.; Neeman, M.; Sillerud, L. O.; Gottesfeld, S. *Journal of Physical Chemistry* **1991**, *95*, 6040-6044.

107. Stejskal, E. O.; Tanner, J. E. *Journal of Chemical Physics* **1965**, *42*, 288-292.

108. Ding, J. F.; Chuy, C.; Holdcroft, S. *Advanced Functional Materials* **2002**, *12*, 389-394.

109. Hietala, S.; Paronen, M.; Holmberg, S.; Nasman, J.; Juhanoja, J.; Karjalainen, M.; Serimaa, R.; Toivola, M.; Lehtinen, T.; Parovuori, K.; Sundholm, G.; Ericson, H.; Mattsson, B.; Torell, L.; Sundholm, F. *Journal of Polymer Science Part A-Polymer Chemistry* **1999**, *37*, 1741-1753.

110. Kallio, T., Kisko, K, Konturi, K, Serimaa, R., Sundholm, F., and Sundholm, G. *Fuel Cells* **2004**, *4*(4), 328-336.

111. Pivovar, B. S.; Wang, Y. X.; Cussler, E. L. *Journal of Membrane Science* **1999**, *154*, 155-162.

112. Siu, A.; Pivovar, B.; Horsfall, J.; Lovell, K. V.; Holdcroft, S. *Journal of Polymer Science Part B-Polymer Physics* **2006**, *44*, 2240-2252.

113. Siu, A., Schmeisser, J., and Holdcroft, S. *Journal of Physical Chemistry B* **2006**, *44*, 2240-2252.

114. Hietala, S.; Holmberg, S.; Nasman, J.; Ostrovskii, D.; Paronen, M.; Serimaa, R.; Sundholm, F.; Torell, L.; Torkkeli, M. *Angewandte Makromolekulare Chemie* **1997**, *253*, 151-167.

115. Jabarin, S. A.; Lofgren, E. A. *Polymer Engineering and Science* **1986**, *26*, 405-409.

116. Bashir, Z. *Polymer* **1992**, *33*, 4304-4313.

117. Bashir, Z. *Indian Journal of Fibre & Textile Research* **1999**, *24*, 1-9.

118. Price, D. M.; Bashir, Z. *Thermochimica Acta* **1995**, *249*, 351-366.

119. James, P. J.; Elliott, J. A.; McMaster, T. J.; Newton, J. M.; Elliott, A. M. S.; Hanna, S.; Miles, M. J. *Journal of Materials Science* **2000**, *35*, 5111-5119.

120. McLean, R. S.; Doyle, M.; Sauer, B. B. *Macromolecules* **2000**, *33*, 6541-6550.

121. Affoune, A. M.; Yamada, A.; Umeda, M. *Journal of Power Sources* **2005**, *148*, 9-17.

122. Blazkek, A. NMR Imagine Investigations of Swelling-Controlled Drug Delivery. *Dissertation.* The University of British Columbia, BC, Canada, 1998.

123. Challa, V.; Kuta, K.; Lopina, S.; Cheung, H. A.; von Meerwall, E. *Langmuir* **2003**, *19*, 4154-4161.

124. Topgaard, D.; Malmborg, C.; Soderman, O. *Journal of Magnetic Resonance* **2002**, *156*, 195-201.

125. Walsby, N.; Hietala, S.; Maunu, S. L.; Sundholm, F.; Kallio, T.; Sundholm, G. *Journal of Applied Polymer Science* **2002**, *86*, 33-42.

126. Zawodzinski, T. A.; Springer, T. E.; Uribe, F.; Gottesfeld, S. *Solid State Ionics* **1993**, *60*, 199-211.

127. Jiang, S. P.; Liu, Z. C.; Tian, Z. Q. *Advanced Materials* **2006**, *18*, 1068-+.

128. Springer, T. E.; Zawodzinski, T. A.; Gottesfeld, S. *Journal of the Electrochemical Society* **1991**, *138*, 2334-2342.

129. Bernardi, D. M.; Verbrugge, M. W. *Journal of the Electrochemical Society* **1992**, *139*, 2477-2491.

130. Navessin, T.; Eikerling, M.; Wang, Q. P.; Song, D. T.; Liu, Z. S.; Horsfall, J.; Lovell, K. V.; Holdcroft, S. *Journal of the Electrochemical Society* **2005**, *152*, A796-A805.

131. Chen, F. L.; Chu, H. S.; Soong, C. Y.; Yan, W. M. *Journal of Power Sources* **2005**, *140*, 243-249.

132. Wang, J. T.; Savinell, R. F.; Wainright, J.; Litt, M.; Yu, H. *Electrochimica Acta* **1996**, *41*, 193-197.

133. Watanabe, M.; Uchida, H.; Seki, Y.; Emori, M.; Stonehart, P. *Journal of the Electrochemical Society* **1996**, *143*, 3847-3852.

134. Standard Test Methods for Water Vapour Transmission of Materials. *ASTM International Standandards Worldwide* 1994, E 96, pp. 696-702.

135. Nishiyama, N.; Suzuki, K.; Yoshida, H.; Teshima, H.; Nemoto, K. *Biomaterials* **2004**, *25*, 965-969.

136. Lopour, P.; Janatova, V. *Biomaterials* **1995**, *16*, 633-640.

137. Eikerling, M.; Kornyshev, A. A.; Kuznetsov, A. M.; Ulstrup, J.; Walbran, S. *Journal of Physical Chemistry B* **2001**, *105*, 3646-3662.

138. Chuy-Sam, C. M. Influence of morphology on the electrochemical properties of proton exchange membranes. *Dissertation*. Simon Fraser University, BC, Canada. 2002.